

# 000 001 002 003 004 005 006 007 008 009 010 011 012 013 014 015 016 017 018 019 020 021 022 023 024 025 026 027 028 029 030 031 032 033 034 035 036 037 038 039 040 041 042 043 044 045 046 047 048 049 050 051 052 053 POST-HOC PROBABILISTIC VISION-LANGUAGE MODELS

Anonymous authors

Paper under double-blind review

## ABSTRACT

Vision-language models (VLMs), such as CLIP and SigLIP, have found remarkable success in classification, retrieval, and generative tasks. For this, VLMs deterministically map images and text descriptions to a joint latent space in which their similarity is assessed using the cosine similarity. However, a deterministic mapping of inputs fails to capture uncertainties over concepts arising from domain shifts when used in downstream tasks. In this work, we propose post-hoc uncertainty estimation in VLMs that does not require additional training. Our method leverages a Bayesian posterior approximation over the last layers in VLMs and analytically quantifies uncertainties over cosine similarities. We demonstrate its effectiveness for uncertainty quantification and support set selection in active learning. Compared to baselines, we obtain improved and well-calibrated predictive uncertainties, interpretable uncertainty estimates, and sample-efficient active learning. Our results show promise for safety-critical applications of large-scale models.

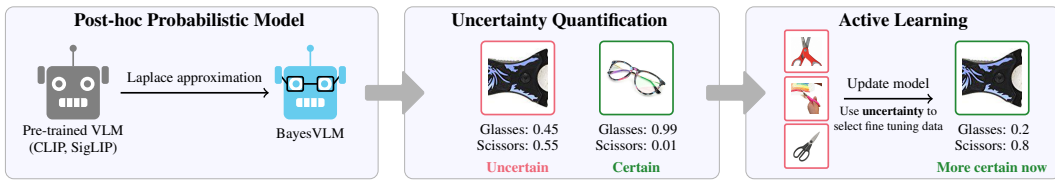


Figure 1: We introduce an efficient and effective post-hoc method to provide uncertainty estimates for vision-language models (e.g., CLIP, SigLIP) using a Laplace approximation. We demonstrate that uncertainty estimates derived from this approximation improve the calibration of these models on several zero-shot classification benchmarks (Sec. 4.1) and are effective in active learning (Sec. 4.2).

## 1 INTRODUCTION

Pre-trained large-scale vision-language models (VLMs) (Bordes et al., 2024; Zhang et al., 2024), such as CLIP (Radford et al., 2021) and SigLIP (Zhai et al., 2023), have achieved remarkable success in tasks like zero-shot classification, retrieval, and generation, driven by training on billion-scale data sets (Gadre et al., 2023; Schuhmann et al., 2022). However, when employing large-scale machine learning models reliably in real-world settings and on downstream applications, we expect them not only to provide accurate predictions but also to enable us to quantify their predictive uncertainties. Obtaining efficient and effective uncertainty estimates is particularly relevant for safety-critical applications, as well as when making decisions based on those estimates, such as in active learning.

Previous work on uncertainty quantification for VLMs has primarily focused on calibration (Guo et al., 2017; Tu et al., 2023), test-time adaptation (Ayhan & Berens, 2018; Farina et al., 2024; Yoon et al., 2024; Lafon et al., 2025), fine-tuning (Fort et al., 2021; Tu et al., 2023; Ju et al., 2025), or training probabilistic VLMs from scratch (Chun, 2024; Chun et al., 2025). However, each of those approaches has limitations regarding their applicability in real-world settings. For example, calibration methods cannot capture epistemic uncertainties, adapter and retraining-based methods come with substantial computational demands and require retraining in streaming/active learning settings, and test-time adaptation methods significantly increase inference costs.

To manifest efficient and effective uncertainty quantification for the reliable application of VLMs, we identify the following desiderata: The method should be applicable to any VLM architecture (*model-agnostic*), and uncertainties should be obtained in a *post-hoc* manner without retraining the

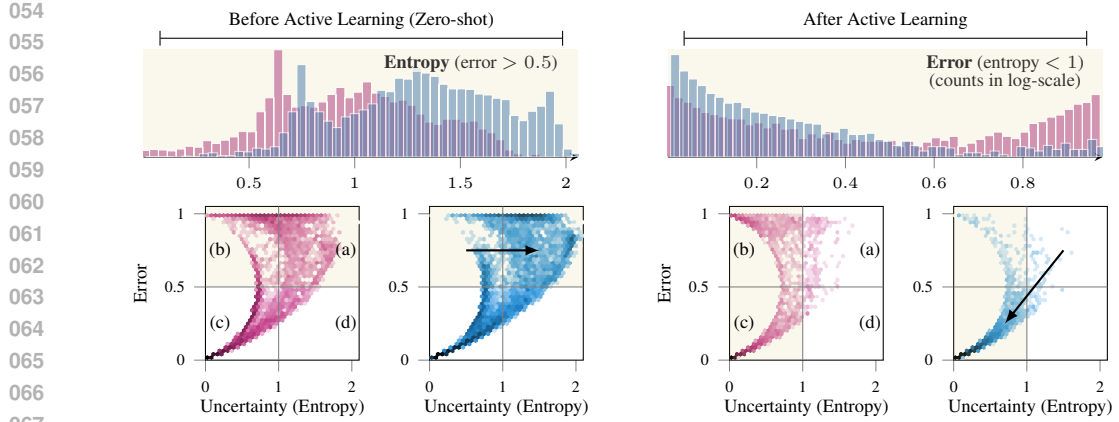


Figure 2: Predictive error vs. uncertainty (entropy) on the EuroSAT data set (Helber et al., 2019) for the OpenCLIP ViT-H-14 model. The **zero-shot** comparison (left side) of the original model (■) and its Bayesian counterpart (□) indicates that our Bayesian model exhibits better calibration and substantially reduces overconfident predictions. **Active Learning** results (right side) show that those improvements lead to a substantially reduced misclassification rate after adaptation; quadrant (b).

model from scratch. During inference, it should have low to no computational overhead (*efficient*) and capture relevant sources of uncertainties (*effective*). Finally, the method should extract uncertainties from the original VLM without adding new layers or adapters that require training (*training-free*).

The Bayesian framework provides a principled way to model epistemic and aleatoric uncertainties, and has shown promise as a ‘toolbox’ for uncertainty quantification in deep learning (Papamarkou et al., 2024). Consider Fig. 2, which shows results on the EuroSAT data set (Helber et al., 2019), a land use and land cover classification task based on Sentinel-2 satellite images, for the popular OpenCLIP model (■). We observe that the Bayesian counterpart (□) results in less overconfident predictions before active learning (compare quadrant b and a) and substantially reduces the error in the predictions after active learning, compared to the fine-tuned OpenCLIP model (■). Much of the misclassification of the OpenCLIP model after active learning can be attributed to its overconfident behaviour before and after active learning, indicating the benefits of using a Bayesian formulation.

This work proposes BayesVLM, an efficient and effective post-hoc uncertainty quantification method for pre-trained VLMs that adheres to the outlined desiderata. We leverage a Laplace approximation (MacKay, 1992) to the Bayesian posterior, thereby eliminating the need for additional training, architectural changes, or modifications to the training objective. For this, we introduce independent probabilistic models for each modality, adhering to the i.i.d. assumption and enabling efficient posterior inference. Further, we derive an analytical expression for the distribution over cosine similarities for efficient uncertainty propagation. We evaluate our approach on zero-shot classification benchmarks and for uncertainty-aware active fine-tuning (Gal et al., 2017; Hübotter et al., 2024), finding improvements in performance over baselines in both scenarios. Lastly, we assess the efficiency and robustness of our approach (BayesVLM) and find that BayesVLM provides efficient, effective, and robust uncertainty estimates, even when the VLM is pre-trained on proprietary data.

**Contributions** The overall contributions are illustrated in Fig. 1 and can be summarised as follows: (i) we propose BayesVLM, an efficient and effective post-hoc method for uncertainty quantification in pre-trained VLMs, without architecture changes or further training (Sec. 3); (ii) we present the first direct Bayesian formulation of vision-language models and derive an analytical expression of the distribution over cosine similarities for efficient uncertainty propagation (Sec. 3.2); (iii) we demonstrate the efficacy of BayesVLM in both zero-shot and active learning settings, showing improvements over baselines in both settings. And we assess its efficiency and robustness, finding that BayesVLM provides robust estimates while introducing little to no computational overhead (Sec. 4).

## 2 RELATED WORK

**Vision-language models** Models like CLIP (Radford et al., 2021) and SigLIP (Zhai et al., 2023), trained on massive data sets such as LAION (Schuhmann et al., 2022), have become widespread in

108 various applications, including zero-shot classification, generative modeling (Rombach et al., 2022;  
 109 Podell et al., 2024), and retrieval (Saito et al., 2023; Karthik et al., 2024). This work presents an  
 110 effective post-hoc approach to uncertainty estimation for these pre-trained VLMs.

111 **Uncertainty in vision-language models** Quantifying uncertainties in VLMs has observed increasing  
 112 interest, with approaches involving learning probabilistic embeddings, for example, by learning  
 113 additional probabilistic adapters (Chun et al., 2025; Lafon et al., 2025) or through pre-training/fine-  
 114 tuning with a probabilistic loss (Chun, 2024; Ju et al., 2025). In addition, recent approaches also  
 115 explored training-free uncertainty quantification, *e.g.*, through test-time augmentation (Ayhan &  
 116 Berens, 2018) or zero-shot out-of-distribution detection (Fu et al., 2025). Another key approach is to  
 117 solely focus on calibration through methods such as temperature scaling (Guo et al., 2017). Further  
 118 related works are discussed in App. B.1. In contrast, we present a training-free post-hoc approach that  
 119 does not require architectural changes, but estimates the Bayesian posterior of a pre-trained model  
 120 and efficiently propagates uncertainty arising from the Bayesian posterior to the VLM output.

121 **Active learning** The goal of active learning (Ren et al., 2021; Settles, 2009) is to improve model  
 122 performance by ‘actively’ selecting additional informative data through an acquisition function  
 123 (Holub et al., 2008; Sener & Savarese, 2018). A particularly relevant area is Bayesian active  
 124 learning (MacKay, 1992; Gal et al., 2017), where acquisition functions leverage model uncertainties.  
 125 Notable examples include the BALD score (Houlsby et al., 2011) and EPIG (Bickford Smith et al.,  
 126 2023), both of which are functions of information gain. While such methods are gaining traction in  
 127 large language models (Hübotter et al., 2025), they remain relatively underexplored for VLMs, where  
 128 ad-hoc strategies are more prevalent. In our work, we bridge this gap.

### 130 3 METHODS

132 **Notation** We denote vectors by bold lower-case letters (*e.g.*,  $\mathbf{x}, \mathbf{a}$ ) and use bold upper-case letters  
 133 for matrices (*e.g.*,  $\mathbf{X}, \mathbf{P}$ ). Further, sets are denoted in upper-case calligraphic letters (*e.g.*,  $\mathcal{D}, \mathcal{I}$ ) and  
 134 model parameters or hyperparameters are denoted using Greek letters (*e.g.*,  $\alpha, \theta$ ). In particular, let  
 135  $\mathbf{x}_i^{\text{IMG}} \in \mathbb{R}^{p_{\text{IMG}}}$  and  $\mathbf{x}_j^{\text{TXT}} \in \mathbb{R}^{p_{\text{TXT}}}$  denote the  $i^{\text{th}}$  image and  $j^{\text{th}}$  text description, respectively. Further,  
 136 let  $\phi: \mathbb{R}^{p_{\text{IMG}}} \rightarrow \mathbb{R}^{d_{\text{IMG}}}$  and  $\psi: \mathbb{R}^{p_{\text{TXT}}} \rightarrow \mathbb{R}^{d_{\text{TXT}}}$  denote the image and text encoders of the VLM, where  
 137  $p_{\text{IMG}}$  and  $p_{\text{TXT}}$  are the respective input dimensionalities and  $d_{\text{IMG}}, d_{\text{TXT}}$  is the dimensionality of the  
 138 respective feature space. Then, by denoting the linear image and text projections as  $\mathbf{P} \in \mathbb{R}^{d \times d_{\text{IMG}}}$  and  
 139  $\mathbf{Q} \in \mathbb{R}^{d \times d_{\text{TXT}}}$  respectively, the feature embeddings in the joint space can be written as  $\mathbf{g} = \mathbf{P}\phi(\mathbf{x}^{\text{IMG}})$   
 140 and  $\mathbf{h} = \mathbf{Q}\psi(\mathbf{x}^{\text{TXT}})$ . We write  $\mathbf{G}$  and  $\mathbf{H}$  to denote the matrices of stacked image and text embeddings,  
 141 respectively, whose rows correspond to the individual  $\mathbf{g}_i$  and  $\mathbf{h}_j$ . Lastly, we use the hat symbol to  
 142 denote unit-length normalised vectors, *e.g.*,  $\hat{\mathbf{g}} = \mathbf{g}/\|\mathbf{g}\|$ . The notation is listed in full in App. A.

#### 144 3.1 BACKGROUND

146 **Language-image pre-training** We consider VLMs trained by minimising the InfoNCE loss  
 147 (Oord et al., 2018) (*e.g.*, CLIP (Radford et al., 2021)) and present additional experiments for the  
 148 SigLIP loss (Zhai et al., 2023). Specifically, the InfoNCE loss is defined as the sum of two cross-  
 149 entropy terms, one for each relational direction—image to text ( $\mathcal{L}_{\text{CE}}(\mathbf{X}^{\text{IMG}}, \mathbf{X}^{\text{TXT}})$ ) and text to image  
 150 ( $\mathcal{L}_{\text{CE}}(\mathbf{X}^{\text{TXT}}, \mathbf{X}^{\text{IMG}})$ ). The total loss is defined as follows  $\mathcal{L}_{\text{InfoNCE}}(\mathbf{X}^{\text{IMG}}, \mathbf{X}^{\text{TXT}}) =$

$$-\underbrace{\frac{1}{2n} \sum_{i=1}^n \log \frac{\exp(t\hat{\mathbf{g}}_i^\top \hat{\mathbf{h}}_i)}{\sum_{j=1}^n \exp(t\hat{\mathbf{g}}_i^\top \hat{\mathbf{h}}_j)}}_{\text{IMG} \rightarrow \text{TXT}, \mathcal{L}_{\text{CE}}(\mathbf{X}^{\text{IMG}}, \mathbf{X}^{\text{TXT}})} - \underbrace{\frac{1}{2n} \sum_{i=1}^n \log \frac{\exp(t\hat{\mathbf{h}}_i^\top \hat{\mathbf{g}}_i)}{\sum_{j=1}^n \exp(t\hat{\mathbf{h}}_i^\top \hat{\mathbf{g}}_j)}},_{\text{IMG} \leftarrow \text{TXT}, \mathcal{L}_{\text{CE}}(\mathbf{X}^{\text{TXT}}, \mathbf{X}^{\text{IMG}})} \quad (1)$$

156 where  $t$  is a learnable temperature parameter,  $n$  denotes the number of image-text pairs, and  $\hat{\mathbf{g}}$  and  $\hat{\mathbf{h}}$   
 157 are the unit-length normalised embeddings. This contrastive loss function encourages embeddings  
 158 for matching image-text pairs to be similar while simultaneously pushing unrelated image-text pairs  
 159 away from each other (Oord et al., 2018). In practice, evaluating this loss is infeasible on billions of  
 160 data points. The common practice adopted is to evaluate it on a sufficiently large batch. Recently,  
 161 the SigLIP loss (Zhai et al., 2023) was proposed as an alternative to the InfoNCE loss, a binary  
 162 classification loss over cosine similarities. Further details on SigLIP are given in App. B.2.

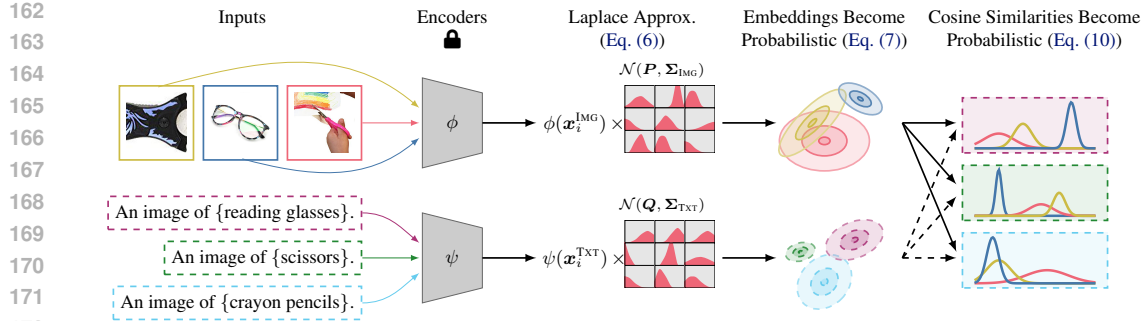


Figure 3: **Illustration of uncertainty propagation in BayesVLMs:** We estimate uncertainties over the last layers of both encoders using a Laplace approximation, which induces probabilistic feature embeddings. We then approximate the distribution over cosine similarities by estimating the expected value and variance. The cosine similarity distribution is then propagated to the VLM output.

**Laplace approximation** Given a data set  $\mathcal{D} = \{(\mathbf{x}_i, \mathbf{y}_i)\}_{i=1}^n$  and denote the neural network parameters as  $\theta$ . In Bayesian deep learning, we aim to estimate the posterior distribution, *i.e.*,

$$p(\theta | \mathcal{D}) = \frac{p(\theta) \prod_{i=1}^n p(\mathbf{y}_i | \mathbf{x}_i, \theta)}{\int_{\theta} p(\theta) \prod_{i=1}^n p(\mathbf{y}_i | \mathbf{x}_i, \theta) d\theta} = \frac{\text{prior} \times \text{likelihood}}{\text{marginal likelihood}}. \quad (2)$$

Since the marginal likelihood involves an intractable high-dimensional integral, we approximate the posterior. We adopt the Laplace approximation (LA) (MacKay, 1992), a post-hoc method that has been increasingly used in the Bayesian deep learning community (Daxberger et al., 2021; Li et al., 2025; Meronen et al., 2024; Ritter et al., 2018; Roy et al., 2022; Scannell et al., 2024).

Specifically, LA fits a Gaussian distribution to the posterior, centred at the MAP estimate of a *pre-trained* model, and is therefore ‘post-hoc’. The *prior* is implicitly defined by the L2 regularisation (weight decay) commonly used during training (Radford et al., 2021; Zhai et al., 2023), and corresponds to a diagonal Gaussian prior on the parameters, *i.e.*,  $p(\theta) = \mathcal{N}(\mathbf{0}, \lambda^{-1} \mathbf{I})$ . The *likelihood* is defined by the training loss. The final approximate posterior is given as  $p(\theta | \mathcal{D}) \approx \mathcal{N}(\theta_{\text{MAP}}, \Sigma)$  where  $\theta_{\text{MAP}}$  is the MAP estimate and  $\Sigma = (-\nabla_{\theta}^2 \log p(\mathcal{D} | \theta)|_{\theta=\theta_{\text{MAP}}} + \lambda \mathbf{I})^{-1}$  is the Hessian of the negative log joint evaluated at  $\theta_{\text{MAP}}$ . A detailed derivation is given in App. B.3.

### 3.2 BAYESVLM: POST-HOC PROBABILISTIC VLMs

To estimate predictive uncertainties in a post-hoc fashion for VLMs, we independently estimate the posterior of the image projection  $P$  and text projection  $Q$ . For CLIP, we reformulate the contrastive loss to obtain tractable likelihoods for  $P$  and  $Q$ , enabling separate posterior inference. We then approximate the Hessian of the log-likelihood and show how the resulting posteriors induce a distribution over cosine similarities. Finally, we derive a Gaussian approximation of this distribution for efficient downstream inference. Our BayesVLM pipeline is illustrated in Fig. 3.

**Estimate posterior: Likelihood approximation** The first step in formulating our Bayesian model, BayesVLM, is to define its likelihood function. When doing so, we encounter the following key challenges: popular loss functions for VLMs, such as the InfoNCE loss (Eq. (1)), entangle modalities and data points. While this is a desirable behaviour when learning multi-modal models, it breaks the usual i.i.d. assumption made in Bayesian models. Specifically, we have that

$$(\mathbf{x}_i^{\text{IMG}}, \mathbf{x}_i^{\text{TXT}}) \stackrel{\text{non-i.i.d.}}{\sim} p(\mathbf{x}_i^{\text{IMG}}, \mathbf{x}_i^{\text{TXT}} | \mathbf{X}_{\setminus i}^{\text{IMG}}, \mathbf{X}_{\setminus i}^{\text{TXT}}, \theta), \quad (3)$$

which hinders straightforward application of the Bayesian framework, as data is only conditionally independent. For that purpose, we are instead assuming two independent probabilistic models, one for each modality, with likelihood functions corresponding to the conditional probability for each modality rather than their joint, *i.e.*,

$$\mathbf{x}_i^{\text{IMG}} \stackrel{\text{i.i.d.}}{\sim} p(\mathbf{x}_i^{\text{IMG}} | \mathbf{X}^{\text{TXT}}, \theta), \quad \mathbf{x}_i^{\text{TXT}} \stackrel{\text{i.i.d.}}{\sim} p(\mathbf{x}_i^{\text{TXT}} | \mathbf{X}^{\text{IMG}}, \theta). \quad (\text{i.i.d. assumption})$$

Consequently, in case of the InfoNCE loss, each likelihood function is given by its respective modality-specific sub-loss term, *i.e.*, in case of the probabilistic model for the image modality, we

have  $\mathcal{L}_{\text{CE}}(\mathbf{X}^{\text{IMG}}, \mathbf{X}^{\text{TXT}})$ , and corresponds to a categorical distribution. A similar approximation is also applied to SigLIP. Crucially, defining independent probabilistic models for each modality additionally necessitates independence between the encoders. For example, when treating the projection layers  $\mathbf{P}$  and  $\mathbf{Q}$  probabilistically, we obtain that:

$$\mathbf{P} \perp\!\!\!\perp \mathbf{Q}. \quad (\text{Consequence of i.i.d. assumption})$$

Following the i.i.d. assumption, the probabilistic model for the image modality is

$$\mathbf{x}_i^{\text{IMG}} \xrightarrow[\text{image projection layer } \mathbf{P}]{\text{image encoder } \phi(\cdot) \text{ and}} \hat{\mathbf{g}}_i = \frac{\mathbf{P}\phi(\mathbf{x}_i^{\text{IMG}})}{\|\mathbf{P}\phi(\mathbf{x}_i^{\text{IMG}})\|} \xrightarrow[\text{compute logits}]{\text{given text embeddings } \hat{\mathbf{H}}} \hat{\mathbf{H}}\hat{\mathbf{g}}_i,$$

and the likelihood becomes a categorical distribution (see App. C.2.1 for formulation)

$$\log p(\mathbf{X}^{\text{IMG}} \mid \mathbf{X}^{\text{TXT}}, \boldsymbol{\theta}) = \log \prod_{i=1}^n p(\mathbf{x}_i^{\text{IMG}} \mid \mathbf{X}^{\text{TXT}}, \boldsymbol{\theta}) = \log \prod_{i=1}^n [\text{softmax}(\hat{\mathbf{H}}\hat{\mathbf{g}}_i)]_i. \quad (4)$$

The probabilistic model for text input can be obtained similarly. We can now apply the LA to this probabilistic model to estimate the approximate posterior.

*Why is this still a reasonable approximation?* For VLMs, it is important to capture interactions between modalities, and assuming independence seems problematic at first. However, as we are using a local post-hoc posterior estimation through the LA, we are effectively introducing an independence conditionally on the MAP estimate of the (joint) contrastive loss. Thus, crucially, even though we assume independence between modalities, we can still capture interactions between modalities. Note that this assumption is also important for computational reasons, as it helps us derive a computationally efficient approach. A detailed discussion is given in Apps. C.1 and C.2.1.

**Estimate posterior: Hessian approximation** Computing the full Hessian of the negative log-likelihood for the posterior covariance in the Laplace approximation is infeasible, as its size scales quadratically with the number of model parameters, making both its estimation and subsequent predictions computationally prohibitive. We, therefore, adopt the Generalised Gauss–Newton (GGN) approximation (Schraudolph, 2002), which requires the Jacobian of the outputs with respect to the parameters. For linear projection layers, this Jacobian can be derived in closed form. For the image and text encoders, however, the parameter count is prohibitively large, so we treat them as deterministic and approximate the posterior only over the projection matrices  $\mathbf{P}$  and  $\mathbf{Q}$ .

To further reduce computational and memory costs, we use the Kronecker-factored (KFAC) Generalised Gauss–Newton (GGN) approximation (Ritter et al., 2018; Martens & Grosse, 2015), which expresses the Hessian as a Kronecker product of two smaller matrices. This preserves a richer posterior structure than diagonal approximations. Following (Ritter et al., 2018), the KFAC GGN approximation for the Hessian of  $\mathbf{P}$  is

$$\underbrace{\left(1/\sqrt{n} \sum_{i=1}^n \phi(\mathbf{x}_i^{\text{IMG}}) \phi(\mathbf{x}_i^{\text{IMG}})^\top\right)}_{\mathbf{A}_{\text{IMG}}} \otimes \underbrace{\left(1/\sqrt{n} \sum_{i=1}^n \mathbf{J}_{\text{IMG}}(\mathbf{x}_i^{\text{IMG}})^\top \boldsymbol{\Lambda}_{\text{IMG}} \mathbf{J}_{\text{IMG}}(\mathbf{x}_i^{\text{IMG}})\right)}_{\mathbf{B}_{\text{IMG}}}, \quad (5)$$

where  $\mathbf{J}_{\text{IMG}}(\mathbf{x}_i^{\text{IMG}}) = \partial \hat{\mathbf{H}} \frac{\partial \mathbf{g}_i}{\|\mathbf{g}_i\|} / \partial \mathbf{g}_i$  and  $\boldsymbol{\Lambda}_{\text{IMG}} = \text{diag}(\boldsymbol{\pi}) - \boldsymbol{\pi}\boldsymbol{\pi}^\top$ , with  $\pi_c = \exp(f_c) / \sum_{c'} \exp(f_{c'})$ ,  $\hat{\mathbf{g}}_i^\top \hat{\mathbf{h}}_c =: f_c$ . As estimating the Kronecker factors  $\mathbf{A}$  and  $\mathbf{B}$  over the training data set is infeasible, following prior work (Ritter et al., 2018), we leverage a subset of the data and include a pseudo-data count  $\tau$  to compensate for the reduced sample size. The posterior covariance over  $\mathbf{P}$  is approximated as

$$\boldsymbol{\Sigma}_{\text{IMG}} = (\tau(\mathbf{A}_{\text{IMG}} \otimes \mathbf{B}_{\text{IMG}}) + \lambda \mathbf{I})^{-1} \approx \underbrace{\left(\sqrt{\tau} \mathbf{A}_{\text{IMG}} + \sqrt{\lambda} \mathbf{I}\right)^{-1}}_{\tilde{\mathbf{A}}_{\text{IMG}}^{-1}} \otimes \underbrace{\left(\sqrt{\tau} \mathbf{B}_{\text{IMG}} + \sqrt{\lambda} \mathbf{I}\right)^{-1}}_{\tilde{\mathbf{B}}_{\text{IMG}}^{-1}}. \quad (6)$$

Note that the Kronecker factors  $\mathbf{A}$  and  $\mathbf{B}$  can be understood as model statistics under the training data. After having the Gaussian posterior over  $\mathbf{P}$  and  $\mathbf{Q}$ , as Gaussians are closed under linear transformations, the distribution over  $\mathbf{g}$  (and  $\mathbf{h}$ ) can be obtained analytically:

$$p(\mathbf{g} \mid \mathcal{D}) = \mathcal{N} \left( \mathbf{P}_{\text{MAP}} \phi(\mathbf{x}^{\text{IMG}}), \left( \phi(\mathbf{x}^{\text{IMG}})^\top \tilde{\mathbf{A}}_{\text{IMG}}^{-1} \phi(\mathbf{x}^{\text{IMG}}) \right) \tilde{\mathbf{B}}_{\text{IMG}}^{-1} \right). \quad (7)$$

Analogous results hold for the text projection  $\mathbf{Q}$  and text embedding  $\mathbf{h}$ , which we omit here for brevity. See App. C.2.2 for detailed derivations, and Algorithm 1 outlines the steps described above.

270 **Make predictions: Cosine similarities approximation** Given a posterior distribution over the model  
 271 parameters, evaluating the VLM on an image-text pair yields *random* image and text embeddings  
 272 rather than deterministic ones, inducing a distribution over their cosine similarity. While the cosine  
 273 similarity remains well-defined, it becomes a random variable and is generally not Gaussian. The  
 274 default prediction method, Monte Carlo estimation, requires costly sampling. To improve efficiency,  
 275 we propose *ProbCosine*, a Gaussian approximation of the cosine similarity distribution based on the  
 276 first two moments of the image and text embeddings.

277 Let the Gaussian distributions for the probabilistic image and text embeddings have means  $\mu_g =$   
 278  $(\mu_{g,1}, \dots, \mu_{g,d})$  and  $\mu_h = (\mu_{h,1}, \dots, \mu_{h,d})$ , and diagonal covariances  $\Sigma_g = \text{diag}(\sigma_{g,1}^2, \dots, \sigma_{g,d}^2)$   
 279 and  $\Sigma_h = \text{diag}(\sigma_{h,1}^2, \dots, \sigma_{h,d}^2)$ . Given the cosine similarity  $S_{\cos}(\mathbf{x}, \mathbf{y}) = \mathbf{x}^\top \mathbf{y} / \|\mathbf{x}\| \|\mathbf{y}\|$  between two  
 280 vectors, the expected cosine similarity under the distribution of  $\mathbf{g}$  and  $\mathbf{h}$  is approximately:  
 281

$$\mathbb{E}[S_{\cos}(\mathbf{g}, \mathbf{h})] \approx \frac{\sum_i^d \mu_{g,i} \mu_{h,i}}{\sqrt{\sum_i \mu_{g,i}^2 + \sigma_{g,i}^2} \sqrt{\sum_i \mu_{h,i}^2 + \sigma_{h,i}^2}}, \quad (8)$$

285 where we use the fact that  $\mathbb{E}[x^2] = \mu_x^2 + \sigma_x^2$  and  $\mathbb{E}[\|\mathbf{x}\|] \leq \sqrt{\sum_i \mu_{x,i}^2 + \sigma_{x,i}^2}$  by applying the triangle  
 286 inequality. We can obtain the second moment (variance)  $\text{Var}[S_{\cos}(\mathbf{g}, \mathbf{h})]$  similarly, which is given as:  
 287

$$\text{Var}[S_{\cos}(\mathbf{g}, \mathbf{h})] = \frac{\sum_i \sigma_{g,i}^2 (\sigma_{h,i}^2 + \mu_{h,i}^2) + \sigma_{h,i}^2 \mu_{g,i}^2}{\sum_i \mu_{g,i}^2 + \sigma_{g,i}^2 \sum_i \mu_{h,i}^2 + \sigma_{h,i}^2}. \quad (9)$$

291 Henceforth, the local Gaussian approximation to the distribution over cosine similarities is:  
 292

$$p(S_{\cos}(\mathbf{g}, \mathbf{h})) \approx \mathcal{N}(\mathbb{E}[S_{\cos}(\mathbf{g}, \mathbf{h})], \text{Var}[S_{\cos}(\mathbf{g}, \mathbf{h})]). \quad (10)$$

294 Finally, the predictive distribution  $p(y | \mathbf{x})$ , *e.g.*, in a zero-shot classification setting, is calculated  
 295 with the probit approximation (Ghosal et al., 2022; Gibbs, 1998). Hence, our approach allows for  
 296 the direct propagation of model uncertainties to the class conditional. As shown in Fig. 10 (App. F),  
 297 compared to ground truth, our approximation qualitatively results in a low approximation error. A  
 298 detailed derivation can be found in App. C.3, and Algorithm 2 outlines the steps described above.

### 3.3 APPLICATION: PROBABILISTIC ACTIVE FEW-SHOT LEARNING

301 Active learning (Ren et al., 2021; Settles, 2009) naturally evaluates uncertainty quality by selecting  
 302 informative samples via predictive uncertainties. We assess BayesVLM with Bayesian acquisition  
 303 functions and adaptive target-region selection. Given unseen test data  $\mathcal{X}_{\text{test}} = \{\mathbf{x}_i^*\}_{i=1}^{n_{\text{test}}}$  with unknown  
 304 labels, the goal is to choose a labeled subset  $\{(\mathbf{x}_j, y_j)\}_{j=1}^m$  with  $\mathbf{x}_j, y_j \sim p(\mathbf{x}, y)$  that best reduces  
 305 label uncertainty on  $\mathcal{X}_{\text{test}}$ . We first bias selection toward the query-set predictive distribution, then  
 306 rank support candidates by influence or informativeness.

307 **Target region selection** Following Margatina et al. (2021); Hübotter et al. (2025), we first apply  
 308  $k$ -NN in feature space to pre-select support candidates near the test data, focusing on training points  
 309 likely useful for the downstream task and reducing acquisition-function cost. Because features are  
 310 stochastic, we compute either the expected cosine similarity (Eq. (8)) or the 2-Wasserstein distance  
 311 between image-feature distributions. Details of the calculations are given in App. D.1.

312 **Acquisition functions** We consider the BALD (Gal et al., 2017) and EPIG (Bickford Smith et al.,  
 313 2023) scores as acquisition functions and assess their viability on downstream tasks. Both acquisition  
 314 functions can utilise model uncertainties estimated by the LA, but they differ conceptually in terms  
 315 of which uncertainties are targeted. See App. D.2 for details.

316 **Online Laplace approximation** We maintain a Laplace posterior over the image-projection matrix  
 317  $\mathbf{P}$  and update it online by (*i*) a gradient step on  $\mathbf{P}$  and (*ii*) updating the Kronecker factors. The prior  
 318 precision can optionally be re-estimated after each step (Lin et al., 2023); see App. D.3.  
 319

## 4 EXPERIMENTS

320 We outline our setup and address three questions: (*i*) Uncertainty quantification: Does BayesVLM pro-  
 321 vide reliable uncertainty estimates? (*ii*) Active learning: Can we select informative data for fine-tuning  
 322

324 **Table 1: Does BayesVLM provide useful uncertainty estimates in zero-shot settings? Yes.** With  
 325 the OpenCLIP ViT-B-32 model, our BayesVLM performs on par with CLIP and temp. scaling on  
 326 ACC (%) and NLPD, while being better calibrated according to the ECE.

Metrics	Methods	FLOWERS-102	FOOD-101	CIFAR-10	CIFAR-100	IMAGENET-R	UCF101	SUN397
ACC $\uparrow$	CLIP (Radford et al., 2021)	<b>68.99</b> $\pm$ 0.5899	80.21 $\pm$ 0.2507	<b>93.61</b> $\pm$ 0.2446	<b>73.76</b> $\pm$ 0.4399	74.52 $\pm$ 0.5032	59.82 $\pm$ 0.7971	67.18 $\pm$ 0.3333
	CLIP (temp. scaling)	<b>68.99</b> $\pm$ 0.5899	80.21 $\pm$ 0.2507	<b>93.61</b> $\pm$ 0.2446	<b>73.76</b> $\pm$ 0.4399	74.52 $\pm$ 0.5032	59.82 $\pm$ 0.7971	67.18 $\pm$ 0.3333
	TTA (Farina et al., 2024)	<b>68.87</b> $\pm$ 0.5905	<b>81.68</b> $\pm$ 0.2435	88.54 $\pm$ 0.3185	65.64 $\pm$ 0.4749	<b>78.29</b> $\pm$ 0.4760	<b>63.07</b> $\pm$ 0.7847	<b>68.58</b> $\pm$ 0.3295
	BayesVLM	<b>68.87</b> $\pm$ 0.4630	80.43 $\pm$ 0.3968	<b>93.62</b> $\pm$ 0.2444	<b>73.63</b> $\pm$ 0.4406	74.45 $\pm$ 0.4361	61.43 $\pm$ 0.4868	66.96 $\pm$ 0.4703
NLPD $\downarrow$	CLIP (Radford et al., 2021)	1.90 $\pm$ 0.0486	0.70 $\pm$ 0.0094	0.21 $\pm$ 0.0079	0.97 $\pm$ 0.0173	1.07 $\pm$ 0.0237	1.59 $\pm$ 0.0364	1.16 $\pm$ 0.0131
	CLIP (temp. scaling)	<b>1.67</b> $\pm$ 0.0373	0.69 $\pm$ 0.0073	0.21 $\pm$ 0.0061	<b>0.94</b> $\pm$ 0.0138	1.04 $\pm$ 0.0191	1.46 $\pm$ 0.0282	<b>1.11</b> $\pm$ 0.0100
	TTA (Farina et al., 2024)	1.86 $\pm$ 0.0475	<b>0.67</b> $\pm$ 0.0094	0.35 $\pm$ 0.0092	1.26 $\pm$ 0.0178	<b>0.90</b> $\pm$ 0.0210	1.50 $\pm$ 0.0363	1.14 $\pm$ 0.0131
	BayesVLM	1.73 $\pm$ 0.0320	<b>0.68</b> $\pm$ 0.0126	<b>0.20</b> $\pm$ 0.0067	0.95 $\pm$ 0.0152	1.03 $\pm$ 0.0177	<b>1.44</b> $\pm$ 0.0183	1.12 $\pm$ 0.0155
ECE $\downarrow$	CLIP (Radford et al., 2021)	6.59	3.91	1.45	6.31	5.20	11.52	8.71
	CLIP (temp. scaling)	5.51	4.74	1.88	3.07	4.80	3.61	2.67
	TTA (Farina et al., 2024)	9.63	4.18	2.02	5.27	2.88	11.75	9.92
	BayesVLM	<b>4.22</b>	<b>1.69</b>	<b>0.72</b>	<b>1.92</b>	<b>1.78</b>	<b>3.57</b>	<b>2.06</b>

336 **Table 2: Can ProbCosine improve the zero-shot performance of pre-trained probabilistic  
 337 models? Yes.** Applying ProbCosine (Ours) to PCME++ (Chun, 2024) consistently improves zero-  
 338 shot performance over its standard prediction (Mean) across classification benchmarks and metrics.

Metrics	Methods	FLOWERS-102	FOOD-101	CIFAR-10	CIFAR-100	IMAGENET-R	UCF101	SUN397
ACC $\uparrow$	Mean	<b>40.59</b> $\pm$ 0.0063	65.47 $\pm$ 0.0030	<b>75.16</b> $\pm$ 0.0043	<b>42.52</b> $\pm$ 0.0049	<b>42.87</b> $\pm$ 0.0057	<b>45.97</b> $\pm$ 0.0035	<b>28.50</b> $\pm$ 0.0073
	Ours	40.43 $\pm$ 0.0063	<b>65.54</b> $\pm$ 0.0030	<b>75.12</b> $\pm$ 0.0043	<b>42.60</b> $\pm$ 0.0049	<b>42.83</b> $\pm$ 0.0057	<b>46.00</b> $\pm$ 0.0035	<b>28.50</b> $\pm$ 0.0073
NLPD $\downarrow$	Mean	3.22 $\pm$ 0.0471	1.30 $\pm$ 0.0125	0.77 $\pm$ 0.0132	2.28 $\pm$ 0.0216	2.77 $\pm$ 0.0346	2.18 $\pm$ 0.0169	3.83 $\pm$ 0.0550
	Ours	<b>3.04</b> $\pm$ 0.0407	<b>1.25</b> $\pm$ 0.0109	<b>0.75</b> $\pm$ 0.0117	<b>2.21</b> $\pm$ 0.0193	<b>2.59</b> $\pm$ 0.0301	<b>2.09</b> $\pm$ 0.0146	<b>3.50</b> $\pm$ 0.0472
ECE $\downarrow$	Mean	8.81	6.78	4.79	10.78	17.38	12.62	26.03
	Ours	<b>2.79</b>	<b>1.54</b>	<b>2.02</b>	<b>4.89</b>	<b>10.82</b>	<b>5.61</b>	<b>19.41</b>

346 using BayesVLM uncertainty estimates? (iii) Efficiency and robustness: Does BayesVLM introduce  
 347 overhead during inference, does it work in closed-source data settings, and how sensitive is its performance  
 348 to key hyperparameters? Further setup details and additional results appear in Apps. E and F.

349 **Data sets** We evaluate zero-shot classification on FLOWERS-102 (Nilsback & Zisserman, 2008),  
 350 FOOD-101 (Bossard et al., 2014), CIFAR-10/100 (Krizhevsky & Hinton, 2009), IMAGENET-  
 351 R (Hendrycks et al., 2021), UCF101 (Soomro et al., 2012), and SUN397 (Xiao et al., 2010). For  
 352 active learning, we form a cross-domain setup with test data from a single domain and a training pool  
 353 spanning all domains, using OfficeHome (Venkateswara et al., 2017) (Art, Clipart, Product) and an  
 354 ImageNet variant with ImageNet-R and ImageNet-Sketch (Wang et al., 2019).

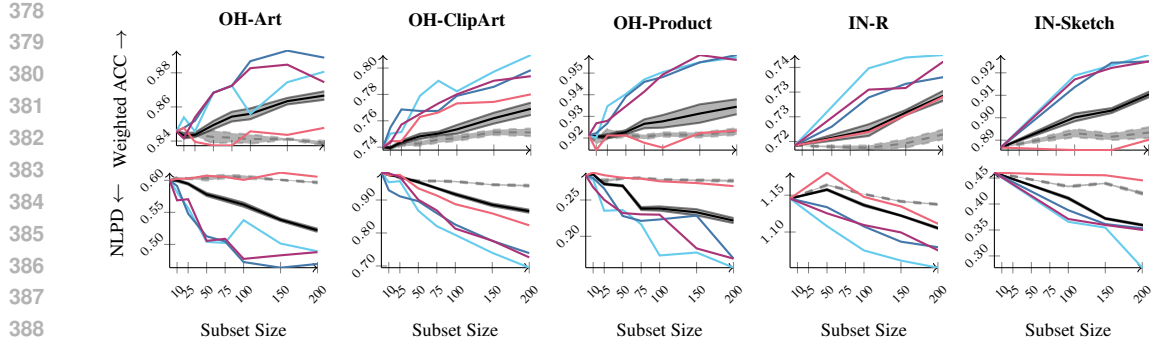
355 **Network architectures** In the zero-shot experiments, we used the OpenCLIP (Ilharco et al., 2021)  
 356 ViT-B-32 and ViT-L-14, and the SigLIP-B-16 model (Zhai et al., 2023). In the active learning  
 357 experiments, we use either CLIP-Huge and SigLIP-Base and fine-tune their projection layers.

358 **Zero-shot baselines** We compare with vanilla CLIP/SigLIP, CLIP/SigLIP with temperature scaling  
 359 (Guo et al., 2017; Nixon et al., 2019), and test-time augmentation (TTA) (Farina et al., 2024). Temperature  
 360 scaling uses the parameter minimising negative log predictive density (NLPD) (Quinonero-  
 361 Candela et al., 2005) on the ImageNet validation set (Deng et al., 2009). We also show ProbCo-  
 362 sine can pair with probabilistic VLMs trained from scratch, e.g., ProLIP (Chun et al., 2025) and  
 363 PCME++ (Chun, 2024). Our focus is on training-free uncertainty estimation, not methods requiring  
 364 extra adaptation (Upadhyay et al., 2023; Zhou et al., 2025).

365 **Acquisition functions** For active learning, we incorporate the uncertainties from BayesVLM into  
 366 the acquisition functions BALD and EPIG and compare against random and entropy-based selection.  
 367 Both BALD and EPIG use target region selection with nearest neighbour (NN), which selects a test  
 368 sample based on the uncertainty score, and then selects its 1-NN of the labelled training samples. We  
 369 also combine the random and entropy baselines with this targeted selection strategy.

370 **Hyperparameter settings** We estimated the Hessian with 327k image-text pairs (10 CLIP  
 371 mini-batches) from LAION-400M (Schuhmann et al., 2022), and used the same estimate across all ex-  
 372 periments. The pseudo-data count  $\tau$  was selected via grid search to minimise NLPD on the ImageNet  
 373 validation set, and the prior precision  $\lambda$  was set by maximising the marginal likelihood (App. C.2).  
 374 The same hyperparameters were used for both zero-shot and active learning experiments.

375 **Evaluation metrics** For the zero-shot experiments, we report the mean and standard error of accuracy  
 376 (ACC), NLPD (Quinonero-Candela et al., 2005), and the expected calibration error (ECE) (Guo

389  
390 **Figure 4: Can we select informative data for fine-tuning using BayesVLM uncertainty estimates?**391 **Yes.** On the OfficeHome data set (OH) and ImageNet variants (IN), when using uncertainty-based  
392 scores (EPIG (—) and BALD (—)) to select the fine-tuning data, we achieve better performance  
393 compared with Entropy (targeted) (—), Entropy (—), Random selection (targeted) (—), and  
394 Random selection (---). Thus, highlighting the benefits of using uncertainties from BayesVLM.395 et al., 2017) computed over the test set. We use a paired  $t$ -test with  $p = 0.05$  to bold results with a  
396 significant statistical difference. Active-learning results use class-weighted accuracy and NLPD.  
397398  
399 

#### 4.1 UNCERTAINTY QUANTIFICATION: DOES BAYESVLM PROVIDE RELIABLE ESTIMATES?

400 We first test the uncertainty estimates of BayesVLM in the zero-shot setting. In Table 1, we report the  
401 zero-shot performance of the CLIP-base model using our post-hoc BayesVLM approach, alongside  
402 baseline methods, with a focus on predictive quality and uncertainty calibration. Results for CLIP-  
403 Large are provided in Table 9 (App. F.7). We observe that BayesVLM achieves similar ACC but lower  
404 NLPD than the deterministic CLIP across all data sets, showing that BayesVLM is less overconfident  
405 when predicting the incorrect class. BayesVLM performs similarly to temp. scaling on ACC and  
406 NLPD, but outperforms all baselines on the ECE. Although TTA achieves higher ACC on some  
407 benchmarks, BayesVLM is significantly better calibrated, which results in more useful uncertainty  
408 estimates. We conclude that BayesVLM improves model calibration and uncertainty estimation  
409 without compromising performance, indicating the effectiveness of our post-hoc strategy.410 To test ProbCosine (Sec. 3.2), we applied it to probabilistic embeddings from the pre-trained VLMs  
411 PCME++ (Chun, 2024) and ProLIP (Chun et al., 2025) (see Table 11). Zero-shot results for PCME++  
412 (Table 2) show that PCME++ combined with ProbCosine keeps accuracy while consistently improving  
413 calibration, indicating ProbCosine can improve any VLM with Gaussian embeddings. **Similarly,**  
414 **ProbCosine improves calibration in most cases when combined with ProLIP (Table 11).**415  
416 

#### 4.2 ACTIVE LEARNING: CAN WE SELECT INFORMATIVE DATA USING BAYESVLM?

417 To further assess the utility of BayesVLM’s uncertainty estimates, we evaluate it in the active  
418 learning setting. We consider a cross-domain setting where the unlabelled target data is from a single  
419 domain while the labelled training samples are from multiple domains. The goal is to select the  
420 most informative samples from the diverse pool for adapting to the target domain, given a maximum  
421 budget (subset size) of support set samples. We experiment with the OfficeHome (Venkateswara  
422 et al., 2017) (OH) dataset, where the domains are {Art, Clipart, Product}, and an ImageNet-variant  
423 (IN) with domains {R, Sketch}. We incorporated the BayesVLM uncertainties into BALD and  
424 EPIG and compared against random and entropy-based selection, either from (i) the full training pool  
425 (Random, Entropy) or with (ii) selection from the test set followed by a 1-NN selection (targeted).426 As shown in Fig. 4, both EPIG and BALD, with BayesVLM uncertainties for data selection, out-  
427 perform Random and Entropy across various subset sizes and target domains. On OH-Product and  
428 IN-Sketch, EPIG and BALD obtain similar weighted ACC as Entropy-targeted. However, EPIG  
429 consistently achieves lower NLPD than Entropy-targeted, which shows that the finetuned model is  
430 less overconfident on incorrect predictions when trained with samples selected using BayesVLM.  
431 Similar conclusions can be observed for CLIP-Huge and SigLIP-Base (Figs. 13 and 14 in App. F).

432 In Fig. 2, we show the change in the predictive error ( $1 - p(y = y^* | x)$ ) and the predictive uncertainty  
 433 (entropy) for BayesVLM before (zero-shot) and after active learning on EuroSAT (Helber et al.,  
 434 2019) using EPIG. We use 200 support points and compare against CLIP with entropy selection.  
 435 BayesVLM reduces overconfident predictions in the zero-shot setting (samples move (b) → (a)), and  
 436 more effectively adapts to the new data set based on the support set (samples move to (c)).  
 437

### 438 4.3 EFFICIENCY AND ROBUSTNESS: HOW EFFICIENT AND ROBUST IS BAYESVLM?

440 Following the protocol for zero-shot experiments, we assessed the performance of BayesVLM when  
 441 estimating the Hessian in settings where the training data is not available, an increasingly common  
 442 setting for modern machine learning models. In particular, we estimated the Hessian of BayesVLM  
 443 using the CC12M as a proxy dataset for CLIP models and used the LAION-400M dataset as a  
 444 proxy for Google’s SigLIP model. We find that BayesVLM provides robust uncertainty estimates  
 445 for CLIP even when estimated on the proxy dataset, *cf.* Table 3, and it remains stable under mild  
 446 distribution shifts in the proxy dataset (see App. F.11). Moreover, BayesVLM provides competitive  
 447 results for SigLIP, a VLM model trained on proprietary data (Table 10 in App. F.7), is robust w.r.t.  
 448 the pseudo-data count  $\tau$  (App. F.8), provides interpretable uncertainties under corruptions (Fig. 5),  
 449 and maintains calibration under substantial distribution shift (App. F.12).  
 450

451 **Table 3: Does BayesVLM work in closed-source data settings? Yes.** With OpenCLIP ViT-B-32  
 452 trained on LAION-400M and BayesVLM estimated on the proxy dataset CC12M, we find that results  
 453 are robust and show only slight degradation; statistically significant differences are **bold** ( $p = 0.05$ ).  
 454

Metrics	Dataset	FLOWERS-102	FOOD-101	CIFAR-10	CIFAR-100	IMAGENET-R	UCF101	SUN397
ACC $\uparrow$	LAION-400M	<b>68.87</b> $\pm$ 0.4630	80.43 $\pm$ 0.3968	93.62 $\pm$ 0.2444	73.63 $\pm$ 0.4406	74.45 $\pm$ 0.4361	61.43 $\pm$ 0.4868	66.96 $\pm$ 0.4703
	CC12M	68.12 $\pm$ 0.4660	80.35 $\pm$ 0.3974	93.57 $\pm$ 0.2453	73.78 $\pm$ 0.4398	74.32 $\pm$ 0.4369	61.46 $\pm$ 0.4867	66.81 $\pm$ 0.4709
NLPD $\downarrow$	LAION-400M	<b>1.73</b> $\pm$ 0.0320	0.68 $\pm$ 0.0126	0.20 $\pm$ 0.0067	0.95 $\pm$ 0.0152	<b>1.03</b> $\pm$ 0.0177	1.44 $\pm$ 0.0183	<b>1.12</b> $\pm$ 0.0155
	CC12M	1.77 $\pm$ 0.0330	0.68 $\pm$ 0.0129	0.20 $\pm$ 0.0067	0.95 $\pm$ 0.0152	1.03 $\pm$ 0.0180	1.44 $\pm$ 0.0185	1.13 $\pm$ 0.0162
ECE $\downarrow$	LAION-400M	4.22	1.69	0.72	1.92	1.78	<b>3.77</b>	<b>2.06</b>
	CC12M	<b>3.84</b>	<b>0.99</b>	<b>0.70</b>	<b>1.43</b>	<b>1.39</b>	3.83	3.89

460 **Computational overhead** Compared to the deterministic CLIP, BayesVLM adds under 5% runtime  
 461 for CLIP-base and less than 1% for huge models (Table 7 in App. F.5). Inference cost rises only  
 462 0.11% GFLOPs for CLIP-base, whereas TTA needs an 80 $\times$  increase, see Table 8 in App. F.5.  
 463

464 **Probabilistic cosine similarities** We qualita-  
 465 tively assessed the distribution obtained by Prob-  
 466 Cosine on a randomly selected test example from  
 467 the OfficeHome clipart domain, evaluating the  
 468 mean and variance of the cosine similarity un-  
 469 der increasing corruption in both image and text  
 470 domains. Text corruption was introduced by  
 471 randomly replacing characters with ‘x’, and im-  
 472 age corruption by randomly adding grey squares.  
 473 Fig. 5 shows the mean and variance of cosine sim-  
 474 ilarities as corruption increases. We observe that  
 475 the expected cosine similarity generally decreases  
 476 and variance increases with more corruption, indi-  
 477 cating that our approximation effectively captures  
 478 model uncertainties under distribution shift. Note  
 479 that we observe a slight increase in the cosine  
 480 similarity after one character has been replaced,  
 481 indicating that performing predictions solely on the expected cosine similarity can be problematic. In  
 482 this case, the variance over cosine similarities can capture the change in the input, highlighting the  
 483 importance of capturing and propagating the model uncertainties.  
 484

485 **Number of data points for Hessian estimation** We evaluated how the number of samples affects  
 486 Hessian estimation by computing the trace over 10 random subsets of LAION-400M. As shown in  
 487 Fig. 11 (App. F.4), the traces for both image and text projections quickly converge with low variance,  
 488 suggesting that 10 mini-batches are sufficient for a stable estimate.  
 489

486     **Number of negative samples** We vary the  
 487     batch size  $K \in \{32768, 8192, 2048\}$  and estimate  
 488     the posterior from 1–5 random batches, report-  
 489     ing mean $\pm$ std over five trials. Since the poste-  
 490     rior depends on negative samples only via the  
 491     Hessian  $\mathbf{B}$  (cf. Eq. (5)), we show the relative  
 492     trace  $\text{tr}(\mathbf{B}_{i \times K}) / \text{tr}(\mathbf{B}_{5 \times K})$ , which is expected  
 493     to be one. As observed in Figure 6 and Fig. 16  
 494     (App. F.9), a base batch size of 32768 stays near  
 495     1 across all batches with minimal variance, indi-  
 496     cating stable estimates of the Hessian.  
 497

## 5 CONCLUSION

500     In this work, we introduced a novel approach for post-hoc uncertainty estimation and propagation  
 501     502     for large-scale vision language models (VLMs) such as CLIP (Radford et al., 2021) and SigLIP (Zhai  
 503     504     et al., 2023). For this, we first formulated probabilistic models admissible to a Bayesian treatment and  
 505     then utilised a post-hoc posterior approximation over the last layer of each encoder. Moreover, we  
 506     derived an analytic approximation of the distribution over cosine similarities for efficient uncertainty  
 507     propagation. Thus, our approach allows efficient and effective uncertainty quantification without any  
 508     architectural changes or additional training. We demonstrated the effectiveness of BayesVLM in zero-  
 509     shot and active learning settings, showing improvements over baselines, and additionally assessed  
 510     its robustness and efficiency, showing BayesVLM is a valuable tool for reliable application of VLMs.  
 511

512     **Limitations** The limitations of our approach are (i) we need access to training data to estimate the  
 513     Hessian, (ii) we require that embeddings are Gaussian distributed, (iii) and our method only utilises  
 514     Bayesian projection layers. As the training data is closed-source for many VLMs, we also assessed  
 515     potential performance degradation when estimating the Hessian on proxy data sets and found that  
 516     BayesVLM provides robust estimates. However, further research is needed in closed-source settings.  
 517

## 518     REPRODUCIBILITY STATEMENT

519     To ensure the reproducibility of our paper, we have provided detailed information on our method and  
 520     experimental setups. We will discuss the respective details below.  
 521

522     **BayesVLM method & algorithms** In addition to the details presented in the main text (Sec. 3),  
 523     we provided detailed derivations in App. C of (i) the likelihood function approximation in App. C.1,  
 524     (ii) the Laplace approximation used in our method in App. C.2, and (iii) the distribution over cosine  
 525     similarities in App. C.3. Moreover, we provided algorithmic descriptions of our method in Algorithm 1  
 526     and in Algorithm 2, outlining details on the precomputation of BayesVLM and the forward inference.  
 527     Lastly, we presented detailed descriptions of the active learning algorithm used in our work in App. D  
 528     and provided specific details on (i) the targeted selection algorithm in App. D.1, (ii) the acquisition  
 529     functions used in this work in App. D.2, and (iii) the online Laplace updates in App. D.3.  
 530

531     **Experiments** In addition to the details provided in the main text in Sec. 4, we provided extensive  
 532     additional information in App. E. Specifically, we (i) detail information on the pre-trained models used  
 533     in this work in App. E.1, (ii) present detailed information on the Hessian estimation and respective  
 534     hyper-parameters in App. E.2, and in App. E.3, and (iii) present details on the hyperparameters and  
 535     setup of the active learning experiments in App. E.4. We also presented additional experiments and  
 536     experimental results that extend beyond those presented in the main text in App. F.  
 537

538     **Implementation** For reference, we have provided a reference implementation of BayesVLM in the  
 539     supplement, which will be made open-access on GitHub upon publication acceptance.  
 540

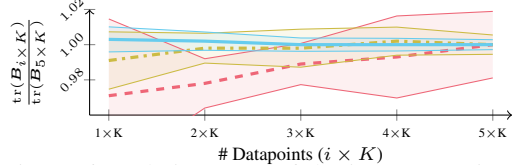


Figure 6: Relative trace of the image Hessian  $B$ -factor for varying base batch sizes  $K$  (2048 (---), 8192 (---), 32768 (—)) and 1–5 random batches. Error bars show  $\pm 1$  std over five trials.

## 541     REFERENCES

542     Sharat Agarwal, Himanshu Arora, Saket Anand, and Chetan Arora. Contextual diversity for active  
 543     learning. In *European Conference on Computer Vision*, pp. 137–153. Springer, 2020. 18  
 544

- 540 Jordan T. Ash, Chicheng Zhang, Akshay Krishnamurthy, John Langford, and Alekh Agarwal. Deep  
 541 batch active learning by diverse, uncertain gradient lower bounds. In *International Conference on*  
 542 *Learning Representations*, 2020. 18
- 543
- 544 Murat Seckin Ayhan and Philipp Berens. Test-time data augmentation for estimation of heteroscedastic  
 545 aleatoric uncertainty in deep neural networks. In *Medical Imaging with Deep Learning*, 2018.  
 546 1, 3, 18
- 547
- 548 Jihwan Bang, Sumyeong Ahn, and Jae-Gil Lee. Active prompt learning in vision language models.  
 549 In *Proceedings of the IEEE/CVF Conference on Computer Vision and Pattern Recognition*, pp.  
 550 27004–27014, 2024. 18
- 551
- 552 Freddie Bickford Smith, Andreas Kirsch, Sebastian Farquhar, Yarin Gal, Adam Foster, and Tom  
 553 Rainforth. Prediction-oriented Bayesian active learning. In *International Conference on Artificial*  
 554 *Intelligence and Statistics*, Proceedings of Machine Learning Research, pp. 7331–7348. PMLR,  
 555 2023. 3, 6, 18, 30
- 556
- 557 Florian Bordes, Richard Yuanzhe Pang, Anurag Ajay, Alexander C Li, Adrien Bardes, Suzanne  
 558 Petryk, Oscar Mañas, Zhiqiu Lin, Anas Mahmoud, Bargav Jayaraman, et al. An introduction to  
 559 vision-language modeling. *arXiv preprint arXiv:2405.17247*, 2024. 1
- 560
- 561 Lukas Bossard, Matthieu Guillaumin, and Luc Van Gool. Food-101 - mining discriminative compo-  
 562 nents with random forests. In *European Conference on Computer Vision*, pp. 446–461. Springer,  
 563 2014. 7
- 564
- 565 Soravit Changpinyo, Piyush Sharma, Nan Ding, and Radu Soricut. Conceptual 12M: Pushing web-  
 566 scale image-text pre-training to recognize long-tail visual concepts. In *Proceedings of the IEEE*  
 567 *Conference on Computer Vision and Pattern Recognition*, pp. 3558–3568, 2021. 32
- 568
- 569 Youngjae Cho, HeeSun Bae, Seungjae Shin, Yeo Dong Youn, Weonyoung Joo, and Il-Chul Moon.  
 570 Make prompts adaptable: Bayesian modeling for vision-language prompt learning with data-  
 571 dependent prior. In *Proceedings of the AAAI Conference on Artificial Intelligence*, volume 38, pp.  
 572 11552–11560, 2024. 18
- 573
- 574 Sanghyuk Chun. Improved probabilistic image-text representations. In *International Conference on*  
 575 *Learning Representations*, 2024. 1, 3, 7, 8, 17
- 576
- 577 Sanghyuk Chun, Seong Joon Oh, Rafael Sampaio De Rezende, Yannis Kalantidis, and Diane Larlus.  
 578 Probabilistic embeddings for cross-modal retrieval. In *Proceedings of the IEEE/CVF Conference*  
 579 *on Computer Vision and Pattern Recognition*, pp. 8415–8424, 2021. 17
- 580
- 581 Sanghyuk Chun, Wonjae Kim, Song Park, and Sangdoo Yun. Probabilistic language-image pre-  
 582 training. In *International Conference on Learning Representations*, 2025. 1, 3, 7, 8, 17, 35,  
 583 36
- 584
- 585 Erik Daxberger, Agustinus Kristiadi, Alexander Immer, Runa Eschenhagen, Matthias Bauer, and  
 586 Philipp Hennig. Laplace redux-effortless Bayesian deep learning. In *Advances in Neural Infor-*  
 587 *mation Processing Systems*, volume 34, pp. 20089–20103. Curran Associates, Inc., 2021. 4, 19,  
 588 31
- 589
- 590 Jia Deng, Wei Dong, Richard Socher, Li-Jia Li, Kai Li, and Li Fei-Fei. ImageNet: A large-scale  
 591 hierarchical image database. In *Proceedings of the IEEE/CVF Conference on Computer Vision*  
 592 *and Pattern Recognition*, pp. 248–255, 2009. 7
- 593
- 594 Karan Desai, Gaurav Kaul, Zubin Trivadi Aysola, and Justin Johnson. Redcaps: Web-curated image-  
 595 text data created by the people, for the people. In *Thirty-fifth Conference on Neural Information*  
 596 *Processing Systems Datasets and Benchmarks Track (Round 1)*, 2021. 32
- 597
- 598 Matteo Farina, Gianni Franchi, Giovanni Iacca, Massimiliano Mancini, and Elisa Ricci. Frustratingly  
 599 easy test-time adaptation of vision-language models. In *Advances in Neural Information Processing*  
 600 *Systems*, volume 37, pp. 129062–129093. Curran Associates, Inc., 2024. 1, 7, 18, 35, 36, 40

- 594 Stanislav Fort, Jie Ren, and Balaji Lakshminarayanan. Exploring the limits of out-of-distribution  
 595 detection. In *Advances in neural information processing systems*, volume 34, pp. 7068–7081.  
 596 Curran Associates, Inc., 2021. 1
- 597
- 598 Hao Fu, Naman Patel, Prashanth Krishnamurthy, and Farshad Khorrami. Clipscope: Enhancing zero-  
 599 shot ood detection with bayesian scoring. In *2025 IEEE/CVF Winter Conference on Applications  
 600 of Computer Vision (WACV)*, pp. 5346–5355. IEEE, 2025. 3, 18
- 601 Samir Yitzhak Gadre, Gabriel Ilharco, Alex Fang, Jonathan Hayase, Georgios Smyrnis, Thao Nguyen,  
 602 Ryan Marten, Mitchell Wortsman, Dhruba Ghosh, Jieyu Zhang, et al. Datacomp: In search of the  
 603 next generation of multimodal datasets. *Advances in Neural Information Processing Systems*, 36:  
 604 27092–27112, 2023. 1
- 605
- 606 Yarin Gal, Riashat Islam, and Zoubin Ghahramani. Deep Bayesian active learning with image data.  
 607 In *International Conference on Machine Learning*, Proceedings of Machine Learning Research,  
 608 pp. 1183–1192. PMLR, 2017. 2, 3, 6, 18
- 609 Ido Galil, Mohammed Dabbah, and Ran El-Yaniv. What can we learn from the selective prediction  
 610 and uncertainty estimation performance of 523 imagenet classifiers? In *International Conference  
 611 on Learning Representations*, 2023. 18
- 612 Indrayudh Ghosal, Yunzhe Zhou, and Giles Hooker. The infinitesimal jackknife and combinations of  
 613 models. *arXiv preprint arXiv:2209.00147*, 2022. 6
- 614
- 615 Mark Gibbs. *Bayesian Gaussian Processes for Regression and Classification*. PhD thesis, University  
 616 of Glasgow, 1998. 6, 20
- 617
- 618 Chuan Guo, Geoff Pleiss, Yu Sun, and Kilian Q Weinberger. On calibration of modern neural  
 619 networks. In *International Conference on Machine Learning*, Proceedings of Machine Learning  
 620 Research, pp. 1321–1330. PMLR, 2017. 1, 3, 7, 18
- 621 Patrick Helber, Benjamin Bischke, Andreas Dengel, and Damian Borth. Eurosat: A novel dataset  
 622 and deep learning benchmark for land use and land cover classification. *IEEE Journal of Selected  
 623 Topics in Applied Earth Observations and Remote Sensing*, 12(7):2217–2226, 2019. 2, 9
- 624
- 625 Dan Hendrycks, Steven Basart, Norman Mu, Saurav Kadavath, Frank Wang, Evan Dorundo, Rahul  
 626 Desai, Tyler Zhu, Samyak Parajuli, Mike Guo, Dawn Song, Jacob Steinhardt, and Justin Gilmer.  
 627 The many faces of robustness: A critical analysis of out-of-distribution generalization. In *Proceed-  
 628 ings of the IEEE/CVF International Conference on Computer Vision*, pp. 8340–8349. IEEE, 2021.  
 629 7, 32
- 630
- 631 Alex Holub, Pietro Perona, and Michael C Burl. Entropy-based active learning for object recogni-  
 632 tion. In *Proceedings of the IEEE/CVF Conference on Computer Vision and Pattern Recognition  
 633 Workshops*, pp. 1–8. IEEE, 2008. 3, 18
- 634
- 635 Neil Houlsby, Ferenc Huszár, Zoubin Ghahramani, and Máté Lengyel. Bayesian active learning for  
 636 classification and preference learning. *arXiv preprint arXiv:1112.5745*, 2011. 3, 18, 30
- 637
- 638 Jonas Hübotter, Sascha Bongni, Ido Hakimi, and Andreas Krause. Efficiently learning at test-time:  
 639 Active fine-tuning of llms. In *International Conference on Learning Representations*, 2025. 3, 6,  
 640 18
- 641
- 642 Jonas Hübotter, Bhavya Sukhija, Lenart Treven, Yarden As, and Andreas Krause. Transductive active  
 643 learning: Theory and applications. *arXiv preprint arXiv:2402.15898*, 2024. 2
- 644
- 645 Gabriel Ilharco, Mitchell Wortsman, Ross Wightman, Cade Gordon, Nicholas Carlini, Rohan Taori,  
 646 Achal Dave, Vaishaal Shankar, Hongseok Namkoong, John Miller, Hannaneh Hajishirzi, Ali  
 647 Farhadi, and Ludwig Schmidt. Openclip, 2021. 7, 32
- 648
- 649 Alexander Immer, Matthias Bauer, Vincent Fortuin, Gunnar Rätsch, and Khan Mohammad Emtiyaz.  
 650 Scalable marginal likelihood estimation for model selection in deep learning. In *International  
 651 Conference on Machine Learning*, Proceedings of Machine Learning Research, pp. 4563–4573.  
 652 PMLR, 2021. 27, 30

- 648 Yatai Ji, Junjie Wang, Yuan Gong, Lin Zhang, Yanru Zhu, Hongfa Wang, Jiaxing Zhang, Tetsuya  
 649 Sakai, and Yujiu Yang. Map: Multimodal uncertainty-aware vision-language pre-training model.  
 650 In *Proceedings of the IEEE/CVF Conference on Computer Vision and Pattern Recognition*, pp.  
 651 23262–23271, 2023. 17
- 652 Li Ju, Max Andersson, Stina Fredriksson, Edward Glöckner, Andreas Hellander, Ekta Vats, and  
 653 Prashant Singh. Exploiting the asymmetric uncertainty structure of pre-trained vlms on the unit  
 654 hypersphere. In *Advances in Neural Information Processing Systems*. Curran Associates, Inc.,  
 655 2025. 1, 3, 18
- 656 Shyamgopal Karthik, Karsten Roth, Massimiliano Mancini, and Zeynep Akata. Vision-by-language  
 657 for training-free compositional image retrieval. In *International Conference on Learning Representations*, 2024. 3
- 658 Alex Krizhevsky and Geoffrey Hinton. Learning multiple layers of features from tiny images.  
 659 Technical report, University of Toronto, 2009. 7
- 660 Marc Lafon, Yannis Karmim, Julio Silva-Rodríguez, Paul Couairon, Clément Rambour, Raphaël  
 661 Fournier-Sniedotta, Ismail Ben Ayed, Jose Dolz, and Nicolas Thome. Vilu: Learning vision-  
 662 language uncertainties for failure prediction. In *Proceedings of the IEEE/CVF International Conference on Computer Vision*. IEEE, 2025. 1, 3, 17
- 663 Hao Li, Jingkuan Song, Lianli Gao, Pengpeng Zeng, Haonan Zhang, and Gongfu Li. A differentiable  
 664 semantic metric approximation in probabilistic embedding for cross-modal retrieval. In *Advances in Neural Information Processing Systems*, volume 35, pp. 11934–11946. Curran Associates, Inc.,  
 665 2022. 17
- 666 Rui Li, Marcus Klasson, Arno Solin, and Martin Trapp. Streamlining prediction in Bayesian deep  
 667 learning. In *International Conference on Learning Representations*, 2025. 4, 19
- 668 Jihao Andreas Lin, Javier Antoran, and José Miguel Hernández-Lobato. Online laplace model  
 669 selection revisited. In *Fifth Symposium on Advances in Approximate Bayesian Inference*, 2023. 6,  
 670 30
- 671 Yuning Lu, Jianzhuang Liu, Yonggang Zhang, Yajing Liu, and Xinmei Tian. Prompt distribution  
 672 learning. In *Proceedings of the IEEE/CVF Conference on Computer Vision and Pattern Recognition*,  
 673 pp. 5206–5215, 2022. 18
- 674 David JC MacKay. Information-based objective functions for active data selection. *Neural Computation*, 4(4):590–604, 1992. 2, 3, 4, 18, 19
- 675 Katerina Margatina, Giorgos Vernikos, Loïc Barrault, and Nikolaos Aletras. Active learning by  
 676 acquiring contrastive examples. In *International Conference on Empirical Methods in Natural Language Processing*, pp. 650—663. Association for Computational Linguistics, 2021. 6
- 677 James Martens and Roger Grosse. Optimizing neural networks with kronecker-factored approximate  
 678 curvature. In *International Conference on Machine Learning*, Proceedings of Machine Learning  
 679 Research, pp. 2408–2417. PMLR, 2015. 5
- 680 Lassi Meronen, Martin Trapp, Andrea Pilzer, Le Yang, and Arno Solin. Fixing overconfidence in  
 681 dynamic neural networks. In *IEEE/CVF Winter Conference on Applications of Computer Vision*,  
 682 pp. 2680–2690, 2024. 4, 19
- 683 Yibo Miao, Yu Lei, Feng Zhou, and Zhijie Deng. Bayesian exploration of pre-trained models for  
 684 low-shot image classification. In *Proceedings of the IEEE/CVF Conference on Computer Vision and Pattern Recognition*, pp. 23849–23859, 2024. 18
- 685 Pablo Morales-Álvarez, Stergios Christodoulidis, Maria Vakalopoulou, Pablo Piantanida, and Jose  
 686 Dolz. Bayesadapter: enhanced uncertainty estimation in clip few-shot adaptation. *arXiv preprint arXiv:2412.09718*, 2024. 17
- 687 Andrei Neculai, Yanbei Chen, and Zeynep Akata. Probabilistic compositional embeddings for  
 688 multimodal image retrieval. In *Proceedings of the IEEE/CVF Conference on Computer Vision and Pattern Recognition Workshops*, pp. 4547–4557, 2022. 17

- 702 Maria-Elena Nilsback and Andrew Zisserman. Automated flower classification over a large number of  
 703 classes. In *Indian Conference on Computer Vision, Graphics and Image Processing*, pp. 722–729.  
 704 IEEE, 2008. 7
- 705
- 706 Jeremy Nixon, Michael W Dusenberry, Linchuan Zhang, Ghassen Jerfel, and Dustin Tran. Measuring  
 707 calibration in deep learning. In *Proceedings of the IEEE/CVF Conference on Computer Vision and*  
 708 *Pattern Recognition Workshops*, volume 2, 2019. 7
- 709
- 710 Aaron van den Oord, Yazhe Li, and Oriol Vinyals. Representation learning with contrastive predictive  
 711 coding. *arXiv preprint arXiv:1807.03748*, 2018. 3, 18
- 712
- 713 Theodore Papamarkou, Maria Skouliaridou, Konstantina Palla, Laurence Aitchison, Julyan Arbel,  
 714 David Dunson, Maurizio Filippone, Vincent Fortuin, Philipp Hennig, José Miguel Hernández-  
 715 Lobato, et al. Position: Bayesian deep learning is needed in the age of large-scale AI. In  
 716 *International Conference on Machine Learning*, Proceedings of Machine Learning Research, pp.  
 717 39556–39586. PMLR, 2024. 2
- 718
- 719 Dustin Podell, Zion English, Kyle Lacey, Andreas Blattmann, Tim Dockhorn, Jonas Müller, Joe  
 720 Penna, and Robin Rombach. SDXL: Improving latent diffusion models for high-resolution image  
 721 synthesis. In *International Conference on Learning Representations*, 2024. 3
- 722
- 723 Joaquin Quinonero-Candela, Carl Edward Rasmussen, Fabian Sinz, Olivier Bousquet, and Bern-  
 724 hard Schölkopf. Evaluating predictive uncertainty challenge. In *Machine Learning Challenges*  
 725 *Workshop*, pp. 1–27. Springer, 2005. 7
- 726
- 727 Alec Radford, Jong Wook Kim, Chris Hallacy, Aditya Ramesh, Gabriel Goh, Sandhini Agarwal,  
 728 Girish Sastry, Amanda Askell, Pamela Mishkin, Jack Clark, et al. Learning transferable visual  
 729 models from natural language supervision. In *International Conference on Machine Learning*,  
 730 Proceedings of Machine Learning Research, pp. 8748–8763. PMLR, 2021. 1, 2, 3, 4, 7, 10, 18, 19,  
 731 32, 36, 40
- 732
- 733 Liva Ralaivola, Marie Szafranski, and Guillaume Stempfel. Chromatic pac-bayes bounds for non-  
 734 iid data. In *Proceedings of the Twelfth International Conference on Artificial Intelligence and*  
 735 *Statistics*, volume 5 of *Proceedings of Machine Learning Research*, pp. 416–423. PMLR, 16–18  
 736 Apr 2009. 21
- 737
- 738 Carl Edward Rasmussen and Christopher K. I. Williams. *Gaussian Processes for Machine Learning*.  
 739 The MIT Press, 2006. 25
- 740
- 741 Pengzhen Ren, Yun Xiao, Xiaojun Chang, Po-Yao Huang, Zhihui Li, Brij B Gupta, Xiaojiang Chen,  
 742 and Xin Wang. A survey of deep active learning. *ACM Computing Surveys*, 54(9):1–40, 2021. 3,  
 743 6, 18
- 744
- 745 Hippolyt Ritter, Aleksandar Botev, and David Barber. A scalable Laplace approximation for neural  
 746 networks. In *International Conference on Learning Representations*, 2018. 4, 5, 19, 24, 32
- 747
- 748 Robin Rombach, Andreas Blattmann, Dominik Lorenz, Patrick Esser, and Björn Ommer. High-  
 749 resolution image synthesis with latent diffusion models. In *Proceedings of the IEEE/CVF Confer-  
 750 ence on Computer Vision and Pattern Recognition*, pp. 10674–10685, 2022. 3
- 751
- 752 Subhankar Roy, Martin Trapp, Andrea Pilzer, Juho Kannala, Nicu Sebe, Elisa Ricci, and Arno Solin.  
 753 Uncertainty-guided source-free domain adaptation. In *European Conference on Computer Vision*,  
 754 pp. 537–555. Springer, 2022. 4, 19
- 755
- 756 Bardia Safaei and Vishal M Patel. Active learning for vision-language models. In *2025 IEEE/CVF  
 757 Winter Conference on Applications of Computer Vision (WACV)*, pp. 4902–4912. IEEE, 2025. 18
- 758
- 759 Kuniaki Saito, Kihyuk Sohn, Xiang Zhang, Chun-Liang Li, Chen-Yu Lee, Kate Saenko, and Tomas  
 760 Pfister. Pic2word: Mapping pictures to words for zero-shot composed image retrieval. In *Proceed-  
 761 ings of the IEEE/CVF Conference on Computer Vision and Pattern Recognition*, pp. 19305–19314,  
 762 2023. 3

- 756 Aidan Scannell, Riccardo Mereu, Paul Edmund Chang, Ella Tamir, Joni Pajarinen, and Arno Solin.  
 757 Function-space parameterization of neural networks for sequential learning. In *International*  
 758 *Conference on Learning Representations*, 2024. 4, 19
- 759 Nicol N Schraudolph. Fast curvature matrix-vector products for second-order gradient descent.  
 760 *Neural computation*, 14(7):1723–1738, 2002. 5, 23
- 762 Christoph Schuhmann, Romain Beaumont, Richard Vencu, Cade Gordon, Ross Wightman, Mehdi  
 763 Cherti, Theo Coombes, Aarush Katta, Clayton Mullis, Mitchell Wortsman, et al. Laion-5b: An  
 764 open large-scale dataset for training next generation image-text models. In *Advances in Neural*  
 765 *Information Processing Systems*, volume 35, pp. 25278–25294. Curran Associates, Inc., 2022. 1,  
 766 2, 7, 32
- 767 Ozan Sener and Silvio Savarese. Active learning for convolutional neural networks: A core-set  
 768 approach. In *International Conference on Learning Representations*, 2018. 3, 18
- 769 Burr Settles. Active learning literature survey. Technical report, University of Wisconsin-Madison  
 770 Department of Computer Sciences, 2009. 3, 6, 18
- 772 Divya Shanmugam, Davis Blalock, Guha Balakrishnan, and John Guttag. Better aggregation in  
 773 test-time augmentation. In *Proceedings of the IEEE/CVF International Conference on Computer*  
 774 *Vision*, pp. 1214–1223, 2021. 18
- 775 Piyush Sharma, Nan Ding, Sebastian Goodman, and Radu Soricut. Conceptual captions: A cleaned,  
 776 hypernymed, image alt-text dataset for automatic image captioning. In *Annual Meeting of the*  
 777 *Association for Computational Linguistics*, pp. 2556–2565, 2018. 32
- 779 Samarth Sinha, Sayna Ebrahimi, and Trevor Darrell. Variational adversarial active learning. In  
 780 *Proceedings of the IEEE/CVF International Conference on Computer Vision*, pp. 5972–5981, 2019.  
 18
- 782 Khurram Soomro, Amir Roshan Zamir, and Mubarak Shah. Ucf101: A dataset of 101 human actions  
 783 classes from videos in the wild. *arXiv preprint arXiv:1212.0402*, 2012. 7
- 785 Weijie Tu, Weijian Deng, and Tom Gedeon. A closer look at the robustness of contrastive language-  
 786 image pre-training (CLIP). In *Thirty-seventh Conference on Neural Information Processing*  
 787 *Systems*, volume 36, pp. 13678–13691. Curran Associates, Inc., 2023. 1, 18
- 788 Weijie Tu, Weijian Deng, Dylan Campbell, Stephen Gould, and Tom Gedeon. An empirical study  
 789 into what matters for calibrating vision-language models. In *International Conference on Machine*  
 790 *Learning*, Proceedings of Machine Learning Research, pp. 48791–48808. PMLR, 2024. 18
- 792 Uddeshya Upadhyay, Shyamgopal Karthik, Massimiliano Mancini, and Zeynep Akata. ProbVLM:  
 793 Probabilistic adapter for frozen vision-language models. In *Proceedings of the IEEE/CVF Interna-*  
*794 tional Conference on Computer Vision*, pp. 1899–1910, 2023. 7, 17
- 795 Hemanth Venkateswara, Jose Eusebio, Shayok Chakraborty, and Sethuraman Panchanathan. Deep  
 796 hashing network for unsupervised domain adaptation. In *Proceedings of the IEEE Conference on*  
*797 Computer Vision and Pattern Recognition*, pp. 5018–5027, 2017. 7, 8, 32
- 798 Dan Wang and Yi Shang. A new active labeling method for deep learning. In *International Joint*  
 799 *Conference on Neural Networks (IJCNN)*, pp. 112–119. IEEE, 2014. 18
- 800 Haohan Wang, Songwei Ge, Zachary Lipton, and Eric P Xing. Learning robust global representations  
 801 by penalizing local predictive power. In *Advances in Neural Information Processing Systems*, pp.  
 802 10506–10518. Curran Associates, Inc., 2019. 7, 32
- 803 Jianxiong Xiao, James Hays, Krista A Ehinger, Aude Oliva, and Antonio Torralba. Sun database:  
 804 Large-scale scene recognition from abbey to zoo. In *Proceedings of the IEEE Computer Society*  
 805 *Conference on Computer Vision and Pattern Recognition*, pp. 3485–3492, 2010. 7
- 807 Yichen Xie, Han Lu, Junchi Yan, Xiaokang Yang, Masayoshi Tomizuka, and Wei Zhan. Active  
 808 finetuning: Exploiting annotation budget in the pretraining-finetuning paradigm. In *Proceedings of*  
 809 *the IEEE/CVF Conference on Computer Vision and Pattern Recognition*, pp. 23715–23724, 2023.  
 18

810 Adam X Yang, Maxime Robeysns, Xi Wang, and Laurence Aitchison. Bayesian low-rank adaptation  
811 for large language models. In *International Conference on Learning Representations*, 2024. 18  
812

813 Hee Suk Yoon, Eunseop Yoon, Joshua Tian Jin Tee, Mark A. Hasegawa-Johnson, Yingzhen Li, and  
814 Chang D. Yoo. C-TPT: Calibrated test-time prompt tuning for vision-language models via text  
815 feature dispersion. In *International Conference on Learning Representations*, 2024. 1, 18

816 Xiaohua Zhai, Basil Mustafa, Alexander Kolesnikov, and Lucas Beyer. Sigmoid loss for language  
817 image pre-training. In *Proceedings of the IEEE/CVF International Conference on Computer Vision*,  
818 pp. 11975–11986, 2023. 1, 2, 3, 4, 7, 10, 18, 19, 32, 36  
819

820 Jingyi Zhang, Jiaxing Huang, Sheng Jin, and Shijian Lu. Vision-language models for vision tasks: A  
821 survey. *IEEE Transactions on Pattern Analysis and Machine Intelligence*, 46(8):5625–5644, 2024.  
822 1

823 Lihua Zhou, Mao Ye, Shuaifeng Li, Nianxin Li, Xiatian Zhu, Lei Deng, Hongbin Liu, and Zhen  
824 Lei. Bayesian test-time adaptation for vision-language models. In *Proceedings of the IEEE/CVF*  
825 *Conference on Computer Vision and Pattern Recognition*, 2025. 7, 18  
826  
827  
828  
829  
830  
831  
832  
833  
834  
835  
836  
837  
838  
839  
840  
841  
842  
843  
844  
845  
846  
847  
848  
849  
850  
851  
852  
853  
854  
855  
856  
857  
858  
859  
860  
861  
862  
863

864 APPENDIX  
865

866 The appendix is organized as follows: [App. A](#) summarizes the notation used in the paper. [App. B](#)  
867 reviews background on vision–language models and the Laplace approximation. [App. C](#) presents  
868 the derivation of the posterior estimation and the efficient computation of distributions over cosine  
869 similarity. [App. D](#) outlines the active learning setup. [App. E](#) details the experimental setup, while  
870 additional results are provided in [App. F](#).

871 **Use of Large Language Models** In this paper, LLMs were used only for minor grammatical edits,  
872 word polishing, or rephrasing. They did not contribute to research ideation, experiments, or core  
873 writing. All suggestions from LLMs were manually verified and edited by the authors prior to final  
874 inclusion.

875  
876 A NOTATION  
877

878 We will briefly summarise the notation used throughout the paper. See [Table 4](#) for the modality-  
879 specific notation used and [Table 5](#) for an overview of the notation of general operands and operators.  
880

881  
882 [Table 4: Summary of modality-specific notation.](#)  
883

Description	Image	Text
Input	$\mathbf{x}^{\text{IMG}}$	$\mathbf{x}^{\text{TXT}}$
Encoder	$\phi(\cdot)$	$\psi(\cdot)$
Projection matrix	$\mathbf{P}$	$\mathbf{Q}$
Embedding	$\mathbf{g}$	$\mathbf{h}$
Normalised embedding	$\hat{\mathbf{g}}$	$\hat{\mathbf{h}}$
Stacked embeddings	$\mathbf{G}$	$\mathbf{H}$
Kronecker factors	$\mathbf{A}_{\text{IMG}}, \mathbf{B}_{\text{IMG}}$	$\mathbf{A}_{\text{TXT}}, \mathbf{B}_{\text{TXT}}$
Covariance matrix	$\Sigma_{\text{IMG}}$	$\Sigma_{\text{TXT}}$
Jacobian matrix	$\mathbf{J}_{\text{IMG}}$	$\mathbf{J}_{\text{TXT}}$

895  
896 [Table 5: Summary of general notation.](#)  
897

Description	Notation
Number of data points	$n$
Number of test data points	$n_{\text{test}}$
Number of support set points	$m$
Kronecker product	$\otimes$
Prior precision	$\lambda$
Pseudo-data count	$\tau$

907  
908 B BACKGROUND  
909

910 This section provides additional background information and an extended discussion of related work.  
911

912 B.1 EXTENDED RELATED WORK  
913

914 **Uncertainty in vision–language models** Many efforts have aimed to learn probabilistic embeddings  
915 by making architectural changes to the VLMs and pre-training with a probabilistic loss ([Chun,](#)  
916 [2024; Chun et al., 2025; 2021; Ji et al., 2023; Li et al., 2022; Nucleai et al., 2022](#)). To reduce  
917 training costs, several works have proposed enabling uncertainty estimation in pre-trained VLMs  
via additional training of adapters ([Morales-Álvarez et al., 2024; Upadhyay et al., 2023; Lafon](#)

918 et al., 2025), learning distributions of prompts (Cho et al., 2024; Lu et al., 2022; Yang et al., 2024),  
919 model ensembles (Miao et al., 2024), or test-time adaptation (Zhou et al., 2025). These works use  
920 a proxy data set different from the pre-training set to learn the predictive uncertainties. Test-time  
921 augmentation is a training-free method used for obtaining input-dependent predictive uncertainties  
922 by augmenting the test input (Ayhan & Berens, 2018; Farina et al., 2024; Shanmugam et al., 2021),  
923 which trades off simplicity against higher inference costs. Other recent training-free approaches focus  
924 on zero-shot out-of-distribution detection in CLIP (Fu et al., 2025) or estimating the distribution  
925 on the hypersphere as a von-Mises Fisher distribution (Ju et al., 2025). Moreover, calibration of  
926 VLMs has been studied for mitigating overconfident predictions (Tu et al., 2023; 2024; Yoon et al.,  
927 2024) where temperature scaling is a common post-hoc method for calibrating pre-trained models  
928 using a held-out validation set (Galil et al., 2023; Guo et al., 2017). Here, we apply the Laplace  
929 approximation to estimate uncertainties directly from the pre-trained VLM without the need for  
930 additional training, architectural changes, or training from scratch. Our approach estimates a Bayesian  
931 posterior distribution with the pre-training data or a proxy data set before test time and has a similar  
932 inference speed to the pre-trained VLM.

933 **Active learning** In active learning (Ren et al., 2021; Settles, 2009), the model determines through  
934 an acquisition function which additional data points are needed to make reliable predictions on a  
935 given downstream task. The acquisition function quantifies the informativeness of samples using  
936 entropy (Holub et al., 2008; Safaei & Patel, 2025; Wang & Shang, 2014) or diversity-based scores (Ash  
937 et al., 2020; Agarwal et al., 2020), coresets (Sener & Savarese, 2018), and parametric models (Sinha  
938 et al., 2019; Xie et al., 2023). Here, we focus on acquisition functions utilising model uncertainties  
939 from Bayesian active learning (Bickford Smith et al., 2023; Gal et al., 2017; Houlsby et al., 2011).  
940 A popular method is the BALD score (Gal et al., 2017; Houlsby et al., 2011), which measures the  
941 reduction in epistemic uncertainties of the model. More recently, EPIG was proposed to measure  
942 the information gain in the space of predictions rather than parameters (Bickford Smith et al., 2023),  
943 building on MacKay’s foundational work on information-theoretic experimental design (MacKay,  
944 1992). While such acquisition functions have gained traction in large language models (Hübotter  
945 et al., 2025), they remain underexplored in VLMs, where ad-hoc strategies like prompt tuning (Bang  
946 et al., 2024) are more prevalent. This work bridges this gap by adapting Bayesian active learning  
947 methods to VLMs.

## 948 B.2 LANGUAGE-IMAGE PRE-TRAINING

949 We consider VLMs trained by minimising the InfoNCE loss (Oord et al., 2018) (e.g., CLIP (Radford  
950 et al., 2021)) or the SigLIP loss (Zhai et al., 2023). Specifically, the InfoNCE loss is defined as the  
951 sum of two cross-entropy terms, one for each relational direction—image to text ( $\mathcal{L}_{\text{CE}}(\mathbf{X}^{\text{IMG}}, \mathbf{X}^{\text{TXT}})$ )  
952 and text to image ( $\mathcal{L}_{\text{CE}}(\mathbf{X}^{\text{TXT}}, \mathbf{X}^{\text{IMG}})$ ). The total loss is defined as follows  $\mathcal{L}_{\text{InfoNCE}}(\mathbf{X}^{\text{IMG}}, \mathbf{X}^{\text{TXT}}) =$

$$953 - \underbrace{\frac{1}{2n} \sum_{i=1}^n \log \frac{\exp(t\hat{\mathbf{g}}_i^\top \hat{\mathbf{h}}_i)}{\sum_{j=1}^n \exp(t\hat{\mathbf{g}}_i^\top \hat{\mathbf{h}}_j)}}_{\text{IMG} \rightarrow \text{TXT}, \mathcal{L}_{\text{CE}}(\mathbf{X}^{\text{IMG}}, \mathbf{X}^{\text{TXT}})} - \underbrace{\frac{1}{2n} \sum_{i=1}^n \log \frac{\exp(t\hat{\mathbf{h}}_i^\top \hat{\mathbf{g}}_i)}{\sum_{j=1}^n \exp(t\hat{\mathbf{h}}_i^\top \hat{\mathbf{g}}_j)}}, \quad (11)$$

954 where  $t$  is a learnable temperature parameter,  $n$  denotes the number of image-text pairs, and  $\hat{\mathbf{g}}$  and  $\hat{\mathbf{h}}$   
955 are the unit-length normalised embeddings. This contrastive loss function encourages embeddings  
956 for matching image-text pairs to be similar while simultaneously pushing unrelated image-text pairs  
957 away from each other (Oord et al., 2018).

958 Recently, the SigLIP loss (Zhai et al., 2023) has been proposed as an alternative to the InfoNCE loss,  
959 aimed at improving numerical stability and training speed. In contrast to InfoNCE, the SigLIP loss  
960 uses a binary classification loss over the cosine similarities, i.e.,  $\mathcal{L}_{\text{SigLIP}}(\mathbf{X}^{\text{IMG}}, \mathbf{X}^{\text{TXT}}) =$

$$961 - \frac{1}{n} \sum_{i=1}^n \sum_{j=1}^n \log \frac{1}{1 + \exp(z_{ij}(-t\hat{\mathbf{g}}_i^\top \hat{\mathbf{h}}_j + b))}, \quad (12)$$

962 where  $z_{ii} = 1$ ,  $z_{ij} = -1$  if  $i \neq j$  and  $b$  is a learnable bias term. For classification settings, the  
963 SigLIP loss does not provide normalised class conditional probabilities  $p(y | \mathbf{x})$  but provides binary  
964 classification probabilities. Henceforth, when fine-tuning a SigLIP pre-trained VLM for classification  
965 tasks, one typically uses the cross-entropy loss instead.

972 B.3 LAPLACE APPROXIMATION  
973974 Given a data set  $\mathcal{D} = \{(\mathbf{x}_i, \mathbf{y}_i)\}_{i=1}^n$  and denote the model parameters as  $\boldsymbol{\theta}$ , in Bayesian deep learning,  
975 we aim to estimate the posterior distribution

976  
977 
$$p(\boldsymbol{\theta} | \mathcal{D}) = \frac{p(\boldsymbol{\theta}) \prod_{i=1}^n p(\mathbf{y}_i | \mathbf{x}_i, \boldsymbol{\theta})}{\int_{\boldsymbol{\theta}} p(\boldsymbol{\theta}) \prod_{i=1}^n p(\mathbf{y}_i | \mathbf{x}_i, \boldsymbol{\theta}) d\boldsymbol{\theta}} \quad (13)$$
  
978  
979  
980  
981

982 Unfortunately, computing the denominator (marginal likelihood) is generally intractable (not feasible)  
983 as it requires integration over a high-dimensional space w.r.t. a potentially non-linear function. A  
984 classical approach to circumvent this challenge is to approximate the posterior using a Laplace  
985 approximation MacKay (1992), which has recently gained traction in the Bayesian deep learning  
986 community Ritter et al. (2018); Daxberger et al. (2021); Li et al. (2025); Meronen et al. (2024); Roy  
987 et al. (2022); Scannell et al. (2024).988 The Laplace approximation hinges on the idea that the posterior distribution is proportional to the  
989 joint, i.e.,

990  
991 
$$p(\boldsymbol{\theta} | \mathcal{D}) \propto p(\boldsymbol{\theta}, \mathcal{D}) = p(\boldsymbol{\theta}) \prod_{i=1}^n p(\mathbf{y}_i | \mathbf{x}_i, \boldsymbol{\theta}) \quad (14)$$
  
992

993 up to an unknown normalisation constant (the marginal likelihood). Moreover, using a second-order  
994 Taylor expansion of the log joint around the maximum-a-posteriori (MAP) estimate  $\boldsymbol{\theta}_{\text{MAP}}$  (mode of  
995 the function) one obtains the unnormalised log density function of a Gaussian centred at  $\boldsymbol{\theta}_{\text{MAP}}$ , i.e.,  
996  $\log p(\boldsymbol{\theta}, \mathcal{D}) \approx$ 

997 
$$\log p(\boldsymbol{\theta}_{\text{MAP}}, \mathcal{D}) - \frac{1}{2}(\boldsymbol{\theta} - \boldsymbol{\theta}_{\text{MAP}})^T \boldsymbol{\Sigma}^{-1}(\boldsymbol{\theta} - \boldsymbol{\theta}_{\text{MAP}}), \quad (15)$$
  
998

999 where

1000 
$$\boldsymbol{\Sigma} = (-\nabla_{\boldsymbol{\theta}}^2 \log p(\boldsymbol{\theta}, \mathcal{D})|_{\boldsymbol{\theta}=\boldsymbol{\theta}_{\text{MAP}}})^{-1} = (-\nabla_{\boldsymbol{\theta}}^2 \log p(\mathcal{D} | \boldsymbol{\theta})|_{\boldsymbol{\theta}=\boldsymbol{\theta}_{\text{MAP}}} - \nabla_{\boldsymbol{\theta}}^2 \log p(\boldsymbol{\theta})|_{\boldsymbol{\theta}=\boldsymbol{\theta}_{\text{MAP}}})^{-1} \quad (16)$$
  
1001

1002 is the Hessian matrix of the log joint (prior  $\times$  likelihood) at  $\boldsymbol{\theta}_{\text{MAP}}$ . By matching the marginal likelihood  
1003 in Eq. (2) with the normalisation constant of a Gaussian, we obtain the Laplace approximation:  
1004

1005 
$$p(\boldsymbol{\theta} | \mathcal{D}) \approx \mathcal{N}(\boldsymbol{\theta}_{\text{MAP}}, \boldsymbol{\Sigma}^{-1}), \quad (17)$$
  
1006

1007 with covariance given by the inverse of the Hessian matrix.

1008 As LA fits a Gaussian distribution to the posterior, centred at the MAP estimate of a *pre-trained* model,  
1009 it is ‘post-hoc’. The *prior* is implicitly defined by the L2 regularisation (weight decay) commonly  
1010 used during training Radford et al. (2021); Zhai et al. (2023), and corresponds to a diagonal Gaussian  
1011 prior on the parameters, i.e.,  $p(\boldsymbol{\theta}) = \mathcal{N}(\mathbf{0}, \lambda^{-1} \mathbf{I})$ . The *likelihood* is defined by the training loss.  
10121013 C DERIVATIONS  
10141015 This section provides detailed derivations of the equations presented in the main text. App. C.1  
1016 discusses the setting where the i.i.d. assumption is not made and the challenges associated with it.  
1017 App. C.2 discusses the i.i.d. assumption, the resulting probabilistic model, and the derivations for  
1018 estimating the posterior. App. C.3 covers the derivations for efficient prediction, i.e., the distribution  
1019 over cosine similarities.1021 C.1 WHAT HAPPENS WITHOUT THE I.I.D. ASSUMPTION  
10221023 In this section, we derive the Laplace approximation when we don’t make the i.i.d. assumption.  
1024 We will show this results in multiple computationally expensive or infeasible terms in the posterior  
1025 covariance, and the posterior obtained by our i.i.d. assumption keeps the computationally feasible  
term.

1026

1027

1028

1029

1030

1031

1032

1033

1034

1035

1036

1037

1038

1039

1040

1041

1042

1043

1044

1045

1046

1047

**Algorithm 1** Turn VLM into BayesVLM

- 1: **Input:** VLM encoders  $\{\text{IMG}, \text{TXT}\}$ , training data  $\mathcal{D}$
- 2: **for each** encoder  $\text{ENC} \in \{\text{IMG}, \text{TXT}\}$  **do**
- 3:   Compute  $\mathbf{A}_{\text{ENC}}$  factor with Eq. (48)
- 4:   Compute  $\mathbf{B}_{\text{ENC}}$  factor with Eq. (49)
- 5: **end for**
- 6: Find  $\lambda$  by maximising the marginal likelihood (Eq. (81))
- 7: (*Optional*) Find optimal  $\tau$  or set  $\tau = 1$
- 8: **for each** encoder  $\text{ENC} \in \{\text{IMG}, \text{TXT}\}$  **do**
- 9:   Update  $\tilde{\mathbf{A}}_{\text{ENC}} \leftarrow \sqrt{\tau} \mathbf{A}_{\text{ENC}} + \sqrt{\lambda} \mathbf{I}$
- 10:   Update  $\tilde{\mathbf{B}}_{\text{ENC}} \leftarrow \sqrt{\tau} \mathbf{B}_{\text{ENC}} + \sqrt{\lambda} \mathbf{I}$
- 11: **end for**
- 12: **Return:**  $\{(\tilde{\mathbf{A}}_{\text{IMG}}, \tilde{\mathbf{B}}_{\text{IMG}}), (\tilde{\mathbf{A}}_{\text{TXT}}, \tilde{\mathbf{B}}_{\text{TXT}})\}$

1048

1049

1050

1051

1052

1053

1054

1055

1056

1057

We start by reformulating the InfoNCE loss. Given a dataset with  $n$  image-text pairs  $(\mathbf{x}_i^{\text{IMG}}, \mathbf{x}_i^{\text{TXT}})$ , the InfoNCE loss is defined as  $\mathcal{L}_{\text{InfoNCE}}(\mathbf{X}^{\text{IMG}}, \mathbf{X}^{\text{TXT}}) =$

$$-\frac{1}{2n} \sum_{i=1}^n \log \underbrace{\frac{\exp(t\hat{\mathbf{g}}_i^\top \hat{\mathbf{h}}_i)}{\sum_{j=1}^n \exp(t\hat{\mathbf{g}}_i^\top \hat{\mathbf{h}}_j)}}_{\mathcal{L}_{\text{CE}}^{\text{IMG}}(\mathbf{X}^{\text{IMG}}, \mathbf{X}^{\text{TXT}})} - \frac{1}{2n} \sum_{i=1}^n \log \underbrace{\frac{\exp(t\hat{\mathbf{h}}_i^\top \hat{\mathbf{g}}_i)}{\sum_{j=1}^n \exp(t\hat{\mathbf{h}}_i^\top \hat{\mathbf{g}}_j)}}_{\mathcal{L}_{\text{CE}}^{\text{TXT}}(\mathbf{X}^{\text{TXT}}, \mathbf{X}^{\text{IMG}})}, \quad (18)$$

where  $t$  is a learnable temperature parameter,  $\hat{\mathbf{g}}$  and  $\hat{\mathbf{h}}$  are the unit-length normalised image and text embeddings. Evaluating this loss in practice is infeasible on billions of data points. Therefore, the common practice adopted in VLMs, such as CLIP, is to evaluate it on a sufficiently large batch. Specifically, denote a batch of image-text pairs as  $\mathcal{B} = \{\mathbf{X}_{\mathcal{B}}^{\text{IMG}}, \mathbf{X}_{\mathcal{B}}^{\text{IMG}}\}$ . Then the InfoNCE loss over the whole data set is approximated by:

$$\mathcal{L}_{\text{InfoNCE}}(\mathbf{X}^{\text{IMG}}, \mathbf{X}^{\text{TXT}}) \approx \sum_{\mathcal{B}} \mathcal{L}_{\text{InfoNCE}}(\mathbf{X}_{\mathcal{B}}^{\text{IMG}}, \mathbf{X}_{\mathcal{B}}^{\text{TXT}}). \quad (19)$$

1060

1061

1062

1063

For each batch, we can view the InfoNCE loss as two separate classification losses, one over image inputs and the other over text inputs. To avoid clutter, we drop the temperature parameter from now on. Looking at the loss for the image inputs  $\mathcal{L}_{\text{CE}}^{\text{IMG}}(\mathbf{X}_{\mathcal{B}}^{\text{IMG}}, \mathbf{X}_{\mathcal{B}}^{\text{TXT}})$ , we can reformulate it as follows:

$$\mathcal{L}_{\text{CE}}^{\text{IMG}}(\mathbf{X}_{\mathcal{B}}^{\text{IMG}}, \mathbf{X}_{\mathcal{B}}^{\text{TXT}}) = -\frac{1}{2|\mathcal{B}|} \sum_{i=1}^{|\mathcal{B}|} \log \frac{\exp(\hat{\mathbf{g}}_i^\top \hat{\mathbf{h}}_i)}{\sum_{j=1}^{|\mathcal{B}|} \exp(\hat{\mathbf{g}}_i^\top \hat{\mathbf{h}}_j)} \quad (20)$$

$$= -\frac{1}{2|\mathcal{B}|} \sum_{i=1}^{|\mathcal{B}|} \log \left[ \text{softmax} \left( [\hat{\mathbf{g}}_i^\top \hat{\mathbf{h}}_1, \hat{\mathbf{g}}_i^\top \hat{\mathbf{h}}_2, \dots, \hat{\mathbf{g}}_i^\top \hat{\mathbf{h}}_{|\mathcal{B}|}] \right) \right]_i \quad (21)$$

$$= -\frac{1}{2|\mathcal{B}|} \sum_{i=1}^{|\mathcal{B}|} \log \left[ \text{softmax} \left( \hat{\mathbf{H}} \hat{\mathbf{g}}_i \right) \right]_i, \quad (22)$$

1073

1074

1075

1076

1077

1078

1079

**Algorithm 2** Compute Predictions

- 1: **Input:** BayesVLM,  $(x_{\text{IMG}}, x_{\text{TXT}})$
- 2:   Compute embeddings using Eq. (7), *i.e.*,
- 3:    $\mu_{\mathbf{g}} \leftarrow \mathbf{P}_{\text{MAP}} \phi(\mathbf{x}_{\text{IMG}})$
- 4:    $\Sigma_{\mathbf{g}} \leftarrow \left( \phi(\mathbf{x}_{\text{IMG}})^\top \tilde{\mathbf{A}}_{\text{IMG}}^{-1} \phi(\mathbf{x}_{\text{IMG}}) \right) \tilde{\mathbf{B}}_{\text{IMG}}^{-1}$
- 5:    $\mu_{\mathbf{h}} \leftarrow \mathbf{Q}_{\text{MAP}} \psi(\mathbf{x}_{\text{TXT}})$
- 6:    $\Sigma_{\mathbf{h}} \leftarrow \left( \psi(\mathbf{x}_{\text{TXT}})^\top \tilde{\mathbf{A}}_{\text{TXT}}^{-1} \psi(\mathbf{x}_{\text{TXT}}) \right) \tilde{\mathbf{B}}_{\text{TXT}}^{-1}$
- 7:   Apply ProbCosine, *i.e.*,
- 8:   Compute  $\mathbb{E}[\text{S}_{\text{cos}}(\mathbf{g}, \mathbf{h})]$  with Eq. (8)
- 9:   Compute  $\text{Var}[\text{S}_{\text{cos}}(\mathbf{g}, \mathbf{h})]$  with Eq. (9)
- 10:   Apply probit approximation (Gibbs, 1998), *i.e.*,
- 11:   **Return:**  $\text{softmax} \left( \frac{t \mathbb{E}[\text{S}_{\text{cos}}(\mathbf{g}, \mathbf{h})]}{\sqrt{1 + \pi/s * t^2 \text{Var}[\text{S}_{\text{cos}}(\mathbf{g}, \mathbf{h})]}} \right)$

1080 Similarly, the text loss  $\mathcal{L}_{\text{CE}}^{\text{TXT}}(\mathbf{X}^{\text{TXT}}, \mathbf{X}^{\text{IMG}})$  can be viewed as cross-entropy loss on the following  
 1081 model where label  $\mathbf{y}_i^{\text{TXT}}$  is a one-hot encoded vector with  $i$ -th element equal to one,  
 1082

1083

1084  $\mathbf{x}_i^{\text{TXT}} \xrightarrow[\text{text projection layer } \mathbf{Q}]{\text{Text encoder } \psi(\cdot) \text{ and}} \hat{\mathbf{h}}_i = \frac{\mathbf{Q}\psi(\mathbf{x}_i^{\text{TXT}})}{\|\mathbf{Q}\psi(\mathbf{x}_i^{\text{TXT}})\|} \xrightarrow[\text{to compute logit}]{\substack{\text{use image embeddings } \hat{\mathbf{G}} \\ \text{to compute logit}}} \hat{\mathbf{G}}\hat{\mathbf{h}}_i.$

1085

1086

1087 Under this view, VLMs trained with the InfoNCE loss can be viewed as using the following equivalent  
 1088 model and loss:  
 1089

1090

1091  $f(\mathbf{x}_i^{\text{IMG}}, \mathbf{x}_i^{\text{TXT}} \mid \mathbf{X}_{\setminus i}^{\text{IMG}}, \mathbf{X}_{\setminus i}^{\text{TXT}}, \boldsymbol{\theta}) = [\hat{\mathbf{H}}\hat{\mathbf{g}}_i, \hat{\mathbf{G}}\hat{\mathbf{h}}_i], \quad (23)$

1092  $\ell_i^{\text{IMG}, \text{TXT}} = \underbrace{-\log[\text{softmax}(\hat{\mathbf{H}}\hat{\mathbf{g}}_i)]_i}_{\ell_i^{\text{IMG}}} - \underbrace{\log[\text{softmax}(\hat{\mathbf{G}}\hat{\mathbf{h}}_i)]_i}_{\ell_i^{\text{Txt}}} \quad (24)$

1093

1094

1095  $\mathcal{L}_{\text{CE}}^{\text{IMG}}(\mathbf{X}_{|\mathcal{B}|}^{\text{IMG}}, \mathbf{X}_{|\mathcal{B}|}^{\text{TXT}}) = \frac{1}{2|\mathcal{B}|} \sum_{i=1}^{|\mathcal{B}|} \ell_i^{\text{IMG}, \text{TXT}}. \quad (25)$

1096

1097

1098

1099

1100

1101

1102

Because data is only conditionally independent in this model, *i.e.*,

1103

1104

$(\mathbf{x}_i^{\text{IMG}}, \mathbf{x}_i^{\text{TXT}}) \sim p(\mathbf{x}_i^{\text{IMG}}, \mathbf{x}_i^{\text{TXT}} \mid \mathbf{X}_{\setminus i}^{\text{IMG}}, \mathbf{X}_{\setminus i}^{\text{TXT}}, \boldsymbol{\theta}), \quad (26)$

1105

1106

the usual i.i.d. assumption made in Bayesian models is violated. Note that performing Bayesian inference over non-i.i.d. data in general settings is an active research field (Ralaivola et al., 2009). Nevertheless, we can still consider applying the Laplace approximation in this case. Crucially, note that Laplace approximation is derived through a second-order Taylor approximation of the negative log joint  $-\log p(\mathcal{D} \mid \boldsymbol{\theta})p(\boldsymbol{\theta})$ , which only requires the negative log joint to be a twice-differentiable function. Therefore, we can still consider the Laplace for local posterior approximation at the MAP estimation. The interpretation of the underlying probabilistic model, however, may be more challenging in those cases.

1107

1108

1109

1110

1111

1112

1113

1114

1115

1116

1117

1118

1119

1120

1121

1122

1123

1124

1125

1126

1127

1128

1129

1130

1131

1132

1133

We will now derive the negative log likelihood Hessian for the image projection layer  $\mathbf{P}$ . Define shorthand  $f_{\mathbf{P}, \mathbf{Q}}(\mathbf{x}_i) = f(\mathbf{x}_i^{\text{IMG}}, \mathbf{x}_i^{\text{TXT}} \mid \mathbf{X}_{\setminus i}^{\text{IMG}}, \mathbf{X}_{\setminus i}^{\text{TXT}}, \boldsymbol{\theta})$ , the GGN approximation for the Hessian over image projection layer  $\mathbf{P}$  is given as

$$\frac{\partial^2 \ell_i^{\text{IMG}, \text{TXT}}}{\partial^2 \mathbf{P}} \approx \frac{\partial f_{\mathbf{P}, \mathbf{Q}}(\mathbf{x}_i)}{\partial \mathbf{P}}^\top \frac{\partial^2 \ell_i}{\partial^2 f_{\mathbf{P}, \mathbf{Q}}(\mathbf{x}_i)} \frac{\partial f_{\mathbf{P}, \mathbf{Q}}(\mathbf{x}_i)}{\partial \mathbf{P}}, \quad (27)$$

where

$$\frac{\partial f_{\mathbf{P}, \mathbf{Q}}(\mathbf{x}_i)}{\partial \mathbf{P}}^\top = \left[ \left( \frac{\partial \hat{\mathbf{H}}\hat{\mathbf{g}}_i}{\partial \mathbf{P}} \right)^\top \left( \frac{\partial \hat{\mathbf{G}}\hat{\mathbf{h}}_i}{\partial \mathbf{P}} \right)^\top \right], \quad (28)$$

$$\frac{\partial^2 \ell_i^{\text{IMG}, \text{TXT}}}{\partial^2 f_{\mathbf{P}, \mathbf{Q}}(\mathbf{x}_i)} = \begin{bmatrix} \frac{\partial^2 \ell_i^{\text{IMG}, \text{TXT}}}{\partial^2 \hat{\mathbf{H}}\hat{\mathbf{g}}_i} & \frac{\partial^2 \ell_i^{\text{IMG}, \text{TXT}}}{\partial \hat{\mathbf{H}}\hat{\mathbf{g}}_i \partial \hat{\mathbf{G}}\hat{\mathbf{h}}_i} \\ \frac{\partial^2 \ell_i^{\text{IMG}, \text{TXT}}}{\partial \hat{\mathbf{G}}\hat{\mathbf{h}}_i \partial \hat{\mathbf{H}}\hat{\mathbf{g}}_i} & \frac{\partial^2 \ell_i^{\text{IMG}, \text{TXT}}}{\partial^2 \hat{\mathbf{G}}\hat{\mathbf{h}}_i} \end{bmatrix}. \quad (29)$$

1134 When writing out the matrix multiplication, we have:

$$1136 \frac{\partial^2 \ell_i^{\text{IMG,TXT}}}{\partial^2 \mathbf{P}} \approx \frac{\partial f_{\mathbf{P}, \mathbf{Q}}(\mathbf{x}_i)}{\partial \mathbf{P}}^\top \frac{\partial^2 \ell_i}{\partial^2 f_{\mathbf{P}, \mathbf{Q}}(\mathbf{x}_i)} \frac{\partial f_{\mathbf{P}, \mathbf{Q}}(\mathbf{x}_i)}{\partial \mathbf{P}} \quad (30)$$

$$1138 \frac{\partial^2 \ell_i^{\text{IMG}}}{\partial^2 \hat{\mathbf{H}} \hat{\mathbf{g}}_i} = \underbrace{\left( \frac{\partial \hat{\mathbf{H}} \hat{\mathbf{g}}_i}{\partial \mathbf{P}} \right)}_{\mathbb{R}^{d \times |\mathcal{B}|}}^\top \underbrace{\frac{\partial^2 \ell_i^{\text{IMG}}}{\partial^2 \hat{\mathbf{H}} \hat{\mathbf{g}}_i}}_{\mathbb{R}^{|\mathcal{B}| \times |\mathcal{B}|}} \frac{\partial \hat{\mathbf{H}} \hat{\mathbf{g}}_i}{\partial \mathbf{P}} \quad (31)$$

$$1142 \quad + \left( \frac{\partial \hat{\mathbf{H}} \hat{\mathbf{g}}_i}{\partial \mathbf{P}} \right)^\top \frac{\partial^2 \ell_i^{\text{TXT}}}{\partial^2 \hat{\mathbf{H}} \hat{\mathbf{g}}_i} \frac{\partial \hat{\mathbf{H}} \hat{\mathbf{g}}_i}{\partial \mathbf{P}} + \left( \frac{\partial \hat{\mathbf{G}} \hat{\mathbf{h}}_i}{\partial \mathbf{P}} \right)^\top \frac{\partial^2 \ell_i^{\text{IMG,TXT}}}{\partial^2 \hat{\mathbf{G}} \hat{\mathbf{h}}_i} \frac{\partial \hat{\mathbf{H}} \hat{\mathbf{g}}_i}{\partial \mathbf{P}} \quad (32)$$

$$1145 \quad + \left( \frac{\partial \hat{\mathbf{H}} \hat{\mathbf{g}}_i}{\partial \mathbf{P}} \right)^\top \frac{\partial^2 \ell_i^{\text{IMG,TXT}}}{\partial^2 \hat{\mathbf{H}} \hat{\mathbf{g}}_i} \frac{\partial \hat{\mathbf{G}} \hat{\mathbf{h}}_i}{\partial \mathbf{P}} + \left( \frac{\partial \hat{\mathbf{G}} \hat{\mathbf{h}}_i}{\partial \mathbf{P}} \right)^\top \frac{\partial^2 \ell_i^{\text{IMG,TXT}}}{\partial^2 \hat{\mathbf{G}} \hat{\mathbf{h}}_i} \frac{\partial \hat{\mathbf{G}} \hat{\mathbf{h}}_i}{\partial \mathbf{P}} \quad (33)$$

1149 Here only the first term  $\left( \frac{\partial \hat{\mathbf{H}} \hat{\mathbf{g}}_i}{\partial \mathbf{P}} \right)^\top \frac{\partial^2 \ell_i^{\text{IMG}}}{\partial^2 \hat{\mathbf{H}} \hat{\mathbf{g}}_i} \frac{\partial \hat{\mathbf{H}} \hat{\mathbf{g}}_i}{\partial \mathbf{P}}$  can be computed efficiently while terms in red  
1150 are intractable or computationally expensive. The approximated posterior for  $\mathbf{P}$  obtained in our  
1151 BayesVLM corresponds to dropping the computationally expensive or infeasible terms in the exact  
1152 model.

## 1154 C.2 ESTIMATING THE POSTERIOR FOR BAYESVLM WITH LAPLACE APPROXIMATION

1156 We now introduce the procedure for estimating the posterior of BayesVLM using the Laplace  
1157 approximation in this section. We start by introducing the i.i.d. assumption we made and the resulting  
1158 probabilistic model for BayesVLM in App. C.2.1. Then, we give the derivation for the posterior  
1159 approximation for BayesVLM in App. C.2.2.

### 1160 C.2.1 I.I.D. ASSUMPTION AND THE RESULTING PROBABILISTIC MODEL

1162 To efficiently estimate the approximated posterior using the Laplace approximation and obtain a clear  
1163 probabilistic model underlying it, we assume two independent probabilistic models, one for each  
1164 modality. Specifically, for each modality, we assume data are i.i.d. given the observations from the  
1165 other modality:

$$1166 \mathbf{x}_i^{\text{IMG}} \stackrel{\text{i.i.d.}}{\sim} p(\mathbf{x}_i^{\text{IMG}} \mid \mathbf{X}^{\text{TXT}}, \boldsymbol{\theta}), \quad \mathbf{x}_i^{\text{TXT}} \stackrel{\text{i.i.d.}}{\sim} p(\mathbf{x}_i^{\text{TXT}} \mid \mathbf{X}^{\text{IMG}}, \boldsymbol{\theta}). \quad (\text{i.i.d. assumption})$$

1168 Following this assumption, the image encoder  $\phi(\cdot)$  and text encoder  $\psi(\cdot)$  will become independent,  
1169 and image projection layer  $\mathbf{P}$  and text projection layer  $\mathbf{Q}$  will become independent as well:

$$1170 \phi(\cdot) \perp\!\!\!\perp \psi(\cdot), \quad \mathbf{P} \perp\!\!\!\perp \mathbf{Q}. \quad (\text{Consequence from i.i.d. assumption})$$

1172 Under these assumptions, we can untangle the interaction between two modalities and approximate  
1173 their respective likelihoods as categorical distributions.

1174 When the modalities become independent, for image input  $\mathbf{x}_i^{\text{IMG}}$ , we can only look at the image loss  
1175 defined as

$$1176 \mathcal{L}_{\text{CE}}^{\text{IMG}}(\mathbf{X}_{\mathcal{B}}^{\text{IMG}}, \mathbf{X}_{\mathcal{B}}^{\text{TXT}}) = -\frac{1}{2|\mathcal{B}|} \sum_{i=1}^{|\mathcal{B}|} \log \frac{\exp(\hat{\mathbf{g}}_i^\top \hat{\mathbf{h}}_i)}{\sum_{j=1}^{|\mathcal{B}|} \exp(\hat{\mathbf{g}}_i^\top \hat{\mathbf{h}}_j)} \quad (34)$$

$$1179 \quad = -\frac{1}{2|\mathcal{B}|} \sum_{i=1}^{|\mathcal{B}|} \log \left[ \text{softmax} \left( \left[ \hat{\mathbf{g}}_i^\top \hat{\mathbf{h}}_1, \hat{\mathbf{g}}_i^\top \hat{\mathbf{h}}_2, \dots, \hat{\mathbf{g}}_i^\top \hat{\mathbf{h}}_{|\mathcal{B}|} \right] \right) \right]_i \quad (35)$$

$$1182 \quad = -\frac{1}{2|\mathcal{B}|} \sum_{i=1}^{|\mathcal{B}|} \log \left[ \text{softmax} \left( \hat{\mathbf{H}} \hat{\mathbf{g}}_i \right) \right]_i, \quad (36)$$

1185 where  $[\text{softmax}(\mathbf{z})]_i \triangleq \frac{\exp(z_i)}{\sum_j \exp(z_j)}$  is the  $i$ -th output of softmax function. This corresponds to the  
1186 cross-entropy loss on the following model, where label  $\mathbf{y}_i^{\text{IMG}}$  is a one-hot encoded vector with  $i$ -th  
1187 element equal to one,

$$\begin{array}{c}
1188 \\
1189 \quad \mathbf{x}_i^{\text{IMG}} \xrightarrow[\text{image projection layer } \mathbf{P}]{\text{Image encoder } \phi(\cdot) \text{ and}} \hat{\mathbf{g}}_i = \frac{\mathbf{P}\phi(\mathbf{x}_i^{\text{IMG}})}{\|\mathbf{P}\phi(\mathbf{x}_i^{\text{IMG}})\|} \xrightarrow[\text{compute logit}]{\text{given text embeddings } \hat{\mathbf{H}}} \hat{\mathbf{H}}\hat{\mathbf{g}}_i. \\
1190 \\
1191 \\
1192 \\
1193 \\
1194 \\
1195 \\
1196
\end{array}$$

Therefore, for image input, the corresponding model is

$$f(\mathbf{x}_i^{\text{IMG}} \mid \mathbf{X}^{\text{TXT}}, \boldsymbol{\theta}) = \hat{\mathbf{H}}\hat{\mathbf{g}}_i, \quad (37)$$

with the corresponding log likelihood

$$\begin{array}{c}
1197 \\
1198 \quad \log p(\mathbf{X}^{\text{IMG}} \mid \mathbf{X}^{\text{TXT}}, \boldsymbol{\theta}) = \log \prod_{i=1}^n p(\mathbf{x}_i^{\text{IMG}} \mid \mathbf{X}^{\text{TXT}}, \boldsymbol{\theta}) \\
1199 \\
1200 \\
1201 \\
1202
\end{array} \quad (38)$$

$$= \log \prod_{i=1}^n \left[ \text{softmax} \left( \hat{\mathbf{H}}\hat{\mathbf{g}}_i \right) \right]_i. \quad (39)$$

Similarly, for text input, the corresponding model is

$$f(\mathbf{x}_i^{\text{TXT}} \mid \mathbf{X}^{\text{IMG}}, \boldsymbol{\theta}) = \hat{\mathbf{G}}\hat{\mathbf{h}}_i, \quad (40)$$

with the corresponding log likelihood

$$\begin{array}{c}
1203 \\
1204 \quad \log p(\mathbf{X}^{\text{TXT}} \mid \mathbf{X}^{\text{IMG}}, \boldsymbol{\theta}) = \log \prod_{i=1}^n p(\mathbf{x}_i^{\text{TXT}} \mid \mathbf{X}^{\text{IMG}}, \boldsymbol{\theta}) \\
1205 \\
1206 \\
1207
\end{array} \quad (41)$$

$$= \log \prod_{i=1}^n \left[ \text{softmax} \left( \hat{\mathbf{G}}\hat{\mathbf{h}}_i \right) \right]_i. \quad (42)$$

Why is this still a reasonable approximation? For VLMs, it is important to capture interactions between modalities, and assuming independence seems problematic at first. However, as we are using a local post-hoc posterior estimation through the Laplace approximation, we are effectively introducing an independence conditionally on the MAP estimate of the (joint) contrastive loss. Thus, crucially, even though we assume independence between modalities, we can still capture interactions between modalities. Note that this assumption is also important for computational reasons, as it helps us derive a computationally efficient approach.

### C.2.2 POSTERIOR APPROXIMATION WITH LA

Now that we have a well-defined probabilistic model and likelihood, we apply the Laplace approximation to it.

**Why only treat  $\mathbf{P}$  and  $\mathbf{Q}$  probabilistically** In the Laplace approximation, for the posterior covariance, we need to compute the Hessian of the log likelihood. This is computationally infeasible for large models and large datasets, and a common approximation is Generalised Gauss–Newton (GGN) approximation (Schraudolph, 2002). Use shorthand  $f_{\boldsymbol{\theta}}(\mathbf{x})$  for the model and denote the log likelihood as  $\ell(y, f_{\boldsymbol{\theta}}(\mathbf{x}))$ , the GGN approximates to the Hessian is given by

$$\nabla_{\boldsymbol{\theta}}^2 \ell(y, f_{\boldsymbol{\theta}}(\mathbf{x})) \approx GGN(\boldsymbol{\theta}) \triangleq \frac{\partial f_{\boldsymbol{\theta}}(\mathbf{x})}{\partial \boldsymbol{\theta}} \frac{\partial^2 \ell(y, f_{\boldsymbol{\theta}}(\mathbf{x}))}{\partial f_{\boldsymbol{\theta}}(\mathbf{x})^2} \frac{\partial f_{\boldsymbol{\theta}}(\mathbf{x})}{\partial \boldsymbol{\theta}} \quad (43)$$

Note that in GGN approximation, we need to compute the Jacobian of the model output w.r.t. to the model parameters  $\frac{\partial f_{\boldsymbol{\theta}}(\mathbf{x})}{\partial \boldsymbol{\theta}}$ . This is computationally infeasible for image and text encoders due to the large number of output dimensions. For image projection and text projection, this challenge can be bypassed as the Jacobian can be obtained analytically. Therefore, we treat the vision and image encoder as fixed and apply the Laplace approximation only for the image projection and text projection  $\mathbf{P}$  and  $\mathbf{Q}$ .

**KFAC GGN approximation to Hessian** To estimate the Hessian of the log likelihood for  $\mathbf{P}$  and  $\mathbf{Q}$ , we use Kronecker-factored approximate curvature (KFAC), which expresses the Hessian as a Kronecker product of two smaller matrices. This significantly reduces computational and memory

1242 costs while preserving a richer posterior structure than diagonal approximations. Following (Ritter  
 1243 et al., 2018), the KFAC GGN approximation for  $-\nabla_{\mathbf{P}}^2 \log p(\mathbf{X}^{\text{IMG}} \mid \mathbf{X}^{\text{TXT}}, \mathbf{P})$  is  
 1244

$$1245 \underbrace{\left( \frac{1}{\sqrt{n}} \sum_{i=1}^n \phi(\mathbf{x}_i^{\text{IMG}}) \phi(\mathbf{x}_i^{\text{TXT}})^\top \right)}_{\mathbf{A}_{\text{IMG}}} \otimes \underbrace{\left( \frac{1}{\sqrt{n}} \sum_{i=1}^n \mathbf{J}_{\text{IMG}}(\mathbf{x}_i^{\text{IMG}})^\top \boldsymbol{\Lambda}_{\text{IMG}} \mathbf{J}_{\text{IMG}}(\mathbf{x}_i^{\text{IMG}}) \right)}_{\mathbf{B}_{\text{IMG}}}, \quad (44)$$

1250 and the KFAC GGN approximation for  $-\nabla_{\mathbf{Q}}^2 \log p(\mathcal{D} \mid \mathbf{Q})$  is  
 1251

$$1252 \underbrace{\left( \frac{1}{\sqrt{n}} \sum_{i=1}^n \psi(\mathbf{x}_i^{\text{TXT}}) \psi(\mathbf{x}_i^{\text{TXT}})^\top \right)}_{\mathbf{A}_{\text{TXT}}} \otimes \underbrace{\left( \frac{1}{\sqrt{n}} \sum_{i=1}^n \mathbf{J}_{\text{TXT}}(\mathbf{x}_i^{\text{TXT}})^\top \boldsymbol{\Lambda}_{\text{TXT}} \mathbf{J}_{\text{TXT}}(\mathbf{x}_i^{\text{TXT}}) \right)}_{\mathbf{B}_{\text{TXT}}}, \quad (45)$$

1257 where  $\mathbf{J}_{\text{IMG}}(\mathbf{x}_i^{\text{IMG}}) = \frac{\partial \hat{\mathbf{H}}_{\|\mathbf{g}_i\|}}{\partial \mathbf{g}_i}$  and  $\boldsymbol{\Lambda}_{\text{IMG}} = \text{diag}(\boldsymbol{\pi}) - \boldsymbol{\pi}\boldsymbol{\pi}^\top$ , with  $\pi_c = \frac{\exp(f_c)}{\sum_{c'} \exp(f_{c'})}$ ,  $\hat{\mathbf{g}}_i^\top \hat{\mathbf{h}}_c =: f_c$ .  
 1258

1259 As estimating the Kronecker factors over billions of data is computationally infeasible, following  
 1260 (Ritter et al., 2018), we leverage a subset of the data and include a pseudo-data count  $\tau$  to compensate  
 1261 for the reduced sample size. Putting everything together, the posterior covariance over  $\mathbf{P}$  and  $\mathbf{Q}$  are  
 1262 approximated as  
 1263

$$1264 \Sigma_{\text{IMG}} = (\tau(\mathbf{A}_{\text{IMG}} \otimes \mathbf{B}_{\text{IMG}}) + \lambda \mathbf{I})^{-1} \approx \underbrace{\left( \sqrt{\tau} \mathbf{A}_{\text{IMG}} + \sqrt{\lambda} \mathbf{I} \right)^{-1}}_{\tilde{\mathbf{A}}_{\text{IMG}}^{-1}} \otimes \underbrace{\left( \sqrt{\tau} \mathbf{B}_{\text{IMG}} + \sqrt{\lambda} \mathbf{I} \right)^{-1}}_{\tilde{\mathbf{B}}_{\text{IMG}}^{-1}}, \quad (46)$$

$$1269 \Sigma_{\text{TXT}} = (\tau(\mathbf{A}_{\text{TXT}} \otimes \mathbf{B}_{\text{TXT}}) + \lambda \mathbf{I})^{-1} \approx \underbrace{\left( \sqrt{\tau} \mathbf{A}_{\text{TXT}} + \sqrt{\lambda} \mathbf{I} \right)^{-1}}_{\tilde{\mathbf{A}}_{\text{TXT}}^{-1}} \otimes \underbrace{\left( \sqrt{\tau} \mathbf{B}_{\text{TXT}} + \sqrt{\lambda} \mathbf{I} \right)^{-1}}_{\tilde{\mathbf{B}}_{\text{TXT}}^{-1}}, \quad (47)$$

1273 where the respective factors are given as:  
 1274

$$1276 \mathbf{A}_{\text{IMG}} = \frac{1}{\sqrt{n}} \sum_{i=1}^n \phi(\mathbf{x}_i^{\text{IMG}}) \phi(\mathbf{x}_i^{\text{IMG}})^\top \\ 1277 \mathbf{A}_{\text{TXT}} = \frac{1}{\sqrt{n}} \sum_{i=1}^n \psi(\mathbf{x}_i^{\text{TXT}}) \psi(\mathbf{x}_i^{\text{TXT}})^\top, \quad (48)$$

$$1283 \mathbf{B}_{\text{IMG}} = \frac{1}{\sqrt{n}} \sum_{i=1}^n \mathbf{J}_{\text{IMG}}(\mathbf{x}_i^{\text{IMG}})^\top \boldsymbol{\Lambda}_{\text{IMG}} \mathbf{J}_{\text{IMG}}(\mathbf{x}_i^{\text{IMG}}) \\ 1284 \mathbf{B}_{\text{TXT}} = \frac{1}{\sqrt{n}} \sum_{i=1}^n \mathbf{J}_{\text{TXT}}(\mathbf{x}_i^{\text{TXT}})^\top \boldsymbol{\Lambda}_{\text{TXT}} \mathbf{J}_{\text{TXT}}(\mathbf{x}_i^{\text{TXT}}), \quad (49)$$

1290 **Jacobian computation** Here we derive the Jacobians  $\mathbf{J}_{\text{IMG}}(\mathbf{x}_i^{\text{IMG}})$  and  $\mathbf{J}_{\text{TXT}}(\mathbf{x}_i^{\text{TXT}})$  used in the KFAC  
 1291 GGN approximation.

1292 Recall  $\hat{\mathbf{g}}_i$  and  $\hat{\mathbf{h}}_j$  denote the normalized image and text embedding, respectively. Let  $\hat{\mathbf{H}}$  denote the  
 1293 matrix of normalized text embeddings with  $\hat{\mathbf{h}}_j$  as its columns and  $\hat{\mathbf{G}}$  the matrix of normalized image  
 1294 embeddings with  $\hat{\mathbf{g}}_i$  as its columns. Then, for the InfoNCE likelihood, which depends on the dot  
 1295 product between the normalised embedding in the batch, we compute the Jacobian for the image

1296 encoder as follows:  
 1297

$$J_{\text{IMG}}^{\text{InfoNCE}}(\mathbf{x}_i^{\text{IMG}}) = \frac{\partial \hat{\mathbf{H}} \hat{\mathbf{g}}_i}{\partial \mathbf{g}_i} \quad (50)$$

$$= \hat{\mathbf{H}} \frac{\partial}{\partial \mathbf{g}_i} \frac{\mathbf{g}_i}{\|\mathbf{g}_i\|} \quad (51)$$

$$= \hat{\mathbf{H}} \frac{\|\mathbf{g}_i\| - \mathbf{g}_i \frac{\partial \|\mathbf{g}_i\|}{\partial \mathbf{g}_i}}{\|\mathbf{g}_i\|^2} \quad (52)$$

$$= \hat{\mathbf{H}} \frac{\|\mathbf{g}_i\| - \frac{\mathbf{g}_i \mathbf{g}_i^\top}{\|\mathbf{g}_i\|}}{\|\mathbf{g}_i\|^2} \quad (53)$$

$$= \hat{\mathbf{H}} \left( \frac{1}{\|\mathbf{g}_i\|} - \frac{\mathbf{g}_i \mathbf{g}_i^\top}{\|\mathbf{g}_i\|^3} \right). \quad (54)$$

1311 Analogously, we obtain the Jacobian for the text encoder given as:  
 1312

$$J_{\text{TXT}}^{\text{InfoNCE}}(\mathbf{x}_i^{\text{TXT}}) = \hat{\mathbf{G}} \left( \frac{1}{\|\mathbf{h}_i\|} - \frac{\mathbf{h}_i \mathbf{h}_i^\top}{\|\mathbf{h}_i\|^3} \right). \quad (55)$$

1316 For SigLIP, we obtain the following Jacobians:  
 1317

$$J_{\text{IMG}}^{\text{SigLIP}}(\mathbf{x}_i^{\text{IMG}}) = \frac{\partial \hat{\mathbf{g}}_i}{\partial \mathbf{g}_i} = \left( \frac{1}{\|\mathbf{g}_i\|} - \frac{\mathbf{g}_i \mathbf{g}_i^\top}{\|\mathbf{g}_i\|^3} \right), \quad (56)$$

1321 and  
 1322

$$J_{\text{TXT}}^{\text{SigLIP}}(\mathbf{x}_i^{\text{TXT}}) = \frac{\partial \hat{\mathbf{h}}_i}{\partial \mathbf{h}_i} = \left( \frac{1}{\|\mathbf{h}_i\|} - \frac{\mathbf{h}_i \mathbf{h}_i^\top}{\|\mathbf{h}_i\|^3} \right). \quad (57)$$

1326 **Hessian of likelihood w.r.t. model output computation** Here we derive the loss Hessian w.r.t.  
 1327 model output  $\Lambda_{\text{IMG}}$  and  $\Lambda_{\text{TXT}}$ . For InfoNCE loss used in CLIP, the zero-shot classifier induced  
 1328 computes unnormalised logits for each class  $c$ , represented by  $\hat{\mathbf{g}}_i^\top \hat{\mathbf{h}}_c =: f_c$ . By applying the softmax  
 1329 function, we calculate the probabilities for each class  $c$  as  $\pi_c = \frac{\exp(f_c)}{\sum_{c'} \exp(f_{c'})}$ . The likelihood Hessian  
 1330 of the cross-entropy loss for this classifier is represented by  
 1331

$$\Lambda_{\text{IMG}}^{\text{InfoNCE}} = \text{diag}(\boldsymbol{\pi}) - \boldsymbol{\pi} \boldsymbol{\pi}^\top. \quad (58)$$

1334 Similarly, the likelihood Hessian for the text encoder follows analogous principles in the text-to-  
 1335 image direction. For a more detailed derivation of the likelihood Hessian, we refer to (Rasmussen  
 1336 & Williams, 2006, Ch. 3.5). Rearranging terms in the analytical expression for  $\mathbf{J}_{\text{IMG}}^\top \Lambda_{\text{IMG}}^{\text{InfoNCE}} \mathbf{J}_{\text{IMG}}$   
 1337 facilitates space-efficient computation of the GGN approximation.

1338 The SigLIP loss is defined as follows  
 1339

$$\mathcal{L}_{\text{SigLIP}}(\mathbf{X}^{\text{IMG}}, \mathbf{X}^{\text{TXT}}) \quad (59)$$

$$= -\frac{1}{n} \sum_{i=1}^n \sum_{j=1}^n \log \frac{1}{1 + \exp(-z_{ij}(t \hat{\mathbf{g}}_i^\top \hat{\mathbf{h}}_j + b))} \quad (60)$$

$$= \frac{1}{n} \sum_{i=1}^n \sum_{j=1}^n \underbrace{-\log \sigma(a_{ij})}_{:= \ell(\hat{\mathbf{g}}_i, \hat{\mathbf{h}}_j)}, \quad (61)$$

1348 where  $\sigma(a) = \frac{1}{1+e^{-a}}$  denotes the sigmoid function, and  $a_{ij} := z_{ij}(t \hat{\mathbf{g}}_i^\top \hat{\mathbf{h}}_j + b)$ , with labels  $z_{ij} \in$   
 1349  $\{-1, 1\}$ , a learnable temperature scaling parameter  $t$ , and a learnable bias  $b$ .

1350 In order to derive the loss Hessian  $\mathbf{\Lambda}^{\text{SigLIP}}$ , we first derive the component-wise loss gradient of  $\ell$ :

$$1352 \quad \frac{\partial}{\partial \hat{\mathbf{g}}_k} \ell(\hat{\mathbf{g}}_i, \hat{\mathbf{h}}_j) \stackrel{i \neq k}{=} 0 \quad (62)$$

$$1354 \quad \frac{\partial}{\partial \hat{\mathbf{g}}_k} \ell(\hat{\mathbf{g}}_i, \hat{\mathbf{h}}_j) \stackrel{i=k}{=} \frac{\partial}{\partial \hat{\mathbf{g}}_k} - \log \sigma(a_{ij}) \quad (63)$$

$$1356 \quad = -\frac{1}{\sigma(a_{ij})} \frac{\partial \sigma(a_{ij})}{\partial a_{ij}} \frac{\partial a_{ij}}{\partial \hat{\mathbf{g}}_i} \quad (64)$$

$$1359 \quad = (\sigma(a_{ij}) - 1) z_{ij} t \hat{\mathbf{h}}_j, \quad (65)$$

1360 which we utilise to derive the component-wise loss Hessian

$$1362 \quad \frac{\partial^2}{\partial \hat{\mathbf{g}}_k \partial \hat{\mathbf{g}}_k^\top} \ell(\hat{\mathbf{g}}_i, \hat{\mathbf{h}}_j) \stackrel{i \neq k}{=} 0 \quad (66)$$

$$1364 \quad \frac{\partial^2}{\partial \hat{\mathbf{g}}_k \partial \hat{\mathbf{g}}_k^\top} \ell(\hat{\mathbf{g}}_i, \hat{\mathbf{h}}_j) \stackrel{i=k}{=} \frac{\partial}{\partial \hat{\mathbf{g}}_k^\top} \left( \sigma(a_{ij}) z_{ij} t \hat{\mathbf{h}}_j - z_{ij} t \hat{\mathbf{h}}_j \right) \quad (67)$$

$$1367 \quad = z_{ij} t \hat{\mathbf{h}}_k \frac{\partial \sigma(a_{ij})}{\partial a_{ij}} \frac{\partial a_{ij}}{\partial \hat{\mathbf{g}}_k^\top} \quad (68)$$

$$1369 \quad = t^2 \sigma(a_{ij}) (1 - \sigma(a_{ij})) \hat{\mathbf{h}}_j \hat{\mathbf{h}}_j^\top. \quad (69)$$

1371 Finally, the likelihood Hessian for the SigLIP loss  $\mathcal{L}_{\text{SigLIP}}$  can be expressed as

$$1373 \quad \mathbf{\Lambda}_{\text{IMG}}^{\text{SigLIP}} = \frac{\partial^2}{\partial \hat{\mathbf{g}}_i \partial \hat{\mathbf{g}}_i^\top} \mathcal{L}(\hat{\mathbf{g}}_{1:n}, \hat{\mathbf{h}}_{1:n}) \quad (70)$$

$$1375 \quad = \frac{1}{n} \sum_{j=1}^n \sum_{i=1}^n \frac{\partial^2}{\partial \hat{\mathbf{g}}_i \partial \hat{\mathbf{g}}_i^\top} \ell(\hat{\mathbf{g}}_i, \hat{\mathbf{h}}_j) \quad (71)$$

$$1378 \quad = \frac{t^2}{n} \sum_{j=1}^n \sigma(a_{ij}) (1 - \sigma(a_{ij})) \hat{\mathbf{h}}_j \hat{\mathbf{h}}_j^\top \quad (72)$$

1381 for the image encoder and as

$$1383 \quad \mathbf{\Lambda}_{\text{TXT}}^{\text{SigLIP}} = \frac{t^2}{n} \sum_{i=1}^n \sigma(a_{ij}) (1 - \sigma(a_{ij})) \hat{\mathbf{g}}_i \hat{\mathbf{g}}_i^\top \quad (73)$$

1385 for the text encoder.

1387 **Efficient Hessian Computation** At first glance, computing the Hessian appears prohibitively  
1388 expensive: the loss Hessian  $\mathbf{\Lambda}$  has shape  $|\mathcal{B}| \times |\mathcal{B}|$  with  $|\mathcal{B}| \approx 32k$ , while the embedding dimension  
1389 is much smaller ( $d \approx 512$ ). Forming  $\mathbf{\Lambda}$  explicitly is therefore impractical. By exploiting its low-rank  
1390 structure and contracting with the Jacobians, however, the computation can be carried out efficiently  
1391 without ever materializing  $\mathbf{\Lambda}$ , making the GGN approximation feasible even for large batches. For  
1392 example, for the image encoder with the InfoNCE loss in CLIP, the GGN block simplifies to

$$1393 \quad \mathbf{J}_{\text{IMG}}(\mathbf{x}_i^{\text{IMG}})^\top \mathbf{\Lambda}_{\text{IMG}} \mathbf{J}_{\text{IMG}}^{\text{InfoNCE}} \quad (74)$$

$$1395 \quad = \underbrace{\left( \frac{1}{\|\mathbf{h}_i\|} - \frac{\mathbf{h}_i \mathbf{h}_i^\top}{\|\mathbf{h}_i\|^3} \right)}_{\mathbf{M} \in \mathbb{R}^{d \times d}} \underbrace{\hat{\mathbf{G}}^\top}_{\in \mathbb{R}^{d \times |\mathcal{B}|}} \underbrace{\left( \text{diag}(\boldsymbol{\pi}) - \boldsymbol{\pi} \boldsymbol{\pi}^\top \right)}_{\in \mathbb{R}^{|\mathcal{B}| \times |\mathcal{B}|}} \underbrace{\hat{\mathbf{G}}}_{\in \mathbb{R}^{|\mathcal{B}| \times d}} \underbrace{\left( \frac{1}{\|\mathbf{h}_i\|} - \frac{\mathbf{h}_i \mathbf{h}_i^\top}{\|\mathbf{h}_i\|^3} \right)}_{\mathbf{M} \in \mathbb{R}^{d \times d}} \quad (75)$$

$$1398 \quad = \mathbf{M} \left( \hat{\mathbf{G}}^\top \text{diag}(\boldsymbol{\pi}) \hat{\mathbf{G}} - \hat{\mathbf{G}}^\top \boldsymbol{\pi} \boldsymbol{\pi}^\top \hat{\mathbf{G}} \right) \mathbf{M} \quad (76)$$

$$1400 \quad = \mathbf{M} \left( \underbrace{\hat{\mathbf{G}}^\top}_{\in \mathbb{R}^{d \times |\mathcal{B}|}} \underbrace{\left( \boldsymbol{\pi} \odot \hat{\mathbf{G}} \right)}_{\in \mathbb{R}^{|\mathcal{B}| \times d}} - \underbrace{\left( \hat{\mathbf{G}}^\top \boldsymbol{\pi} \right)}_{\in \mathbb{R}^{d \times |\mathcal{B}|}} \underbrace{\left( \hat{\mathbf{G}}^\top \boldsymbol{\pi} \right)^\top}_{\in \mathbb{R}^{|\mathcal{B}| \times d}} \right) \mathbf{M} \quad (77)$$

1403 where  $\odot$  denotes row-wise scaling of  $\hat{\mathbf{G}}$  by the vector  $\boldsymbol{\pi}$ .

1404  
 1405 **Marginal likelihood** To learn the prior precision parameter  $\lambda$ , we follow prior work (*e.g.*, (Immer  
 1406 et al., 2021)) and optimise the log marginal likelihood within each probabilistic model. For the image  
 1407 projection layer  $\mathbf{P}$ , denote the prior and posterior as below:  
 1408

$$\text{prior} : \mathcal{N}(\mathbf{0}, \lambda_{\text{IMG}} \mathbf{I}) \quad (78)$$

$$\text{posterior} : \mathcal{N}(\mathbf{P}_{\text{MAP}}, \boldsymbol{\Sigma}_{\text{IMG}}) \quad (79)$$

1410 The marginal likelihood is  
 1411

$$1412 \log p(\mathbf{X}^{\text{IMG}} \mid \mathbf{X}^{\text{TXT}}) \approx \sum_{i=1}^n \log p(\mathbf{x}_i^{\text{IMG}} \mid \mathbf{X}^{\text{TXT}}, \mathbf{P}_{\text{MAP}}) \quad (80)$$

$$1415 - \frac{1}{2} (\mathbf{P}_{\text{MAP}}^{\top} \lambda \mathbf{I} \mathbf{P}_{\text{MAP}} - \log \det(\boldsymbol{\Sigma}_{\text{IMG}}) + \log \det(\lambda_{\text{IMG}} \mathbf{I})) \quad (81)$$

1417 We can learn the prior precision  $\lambda_{\text{IMG}}$  using gradient-based optimisation.  
 1418

1419 **Distribution over image and vision features** For completeness, we will briefly derive the  
 1420 distribution over image and vision features. In particular, for the image encoder let  $\mathbf{P} \sim$   
 1421  $\mathcal{MN}(\mathbf{P}_{\text{MAP}}, \mathbf{B}_{\text{IMG}}^{-1}, \mathbf{A}_{\text{IMG}}^{-1})$ , then:

$$1422 \mathbf{g} = \mathbf{P} \phi(\mathbf{x}^{\text{IMG}}) \quad (82)$$

1424 with  $\mathbf{P} \phi(\mathbf{x}^{\text{IMG}}) \sim$   
 1425

$$1426 \mathcal{MN}(\mathbf{P}_{\text{MAP}} \phi(\mathbf{x}^{\text{IMG}}), \mathbf{B}_{\text{IMG}}^{-1}, \phi(\mathbf{x}^{\text{IMG}})^{\top} \mathbf{A}_{\text{IMG}}^{-1} \phi(\mathbf{x}^{\text{IMG}})) \\ 1427 \mathbf{g} \sim \mathcal{N}(\mathbf{P}_{\text{MAP}} \phi(\mathbf{x}^{\text{IMG}}), (\phi(\mathbf{x}^{\text{IMG}})^{\top} \mathbf{A}_{\text{IMG}}^{-1} \phi(\mathbf{x}^{\text{IMG}})) \mathbf{B}_{\text{IMG}}^{-1}). \quad (83)$$

### 1429 C.3 DISTRIBUTION OVER COSINE SIMILARITIES

1431 For the derivation of the distribution over cosine similarities, first recall the definition of the cosine  
 1432 similarity between two vectors,  $\mathbf{g}$  and  $\mathbf{h}$ , which is given as  $S_{\text{cos}}(\mathbf{g}, \mathbf{h}) = \frac{\mathbf{g}^{\top} \mathbf{h}}{\|\mathbf{g}\| \|\mathbf{h}\|}$ . Now, let  $\mathbf{g}$   
 1433 and  $\mathbf{h}$  denote random vectors for the image and text embeddings, respectively. Further, let us  
 1434 assume that their distribution follows a Gaussian distribution with mean  $\boldsymbol{\mu}_{\mathbf{g}} = (\mu_{\mathbf{g},1}, \dots, \mu_{\mathbf{g},d})$  and  
 1435  $\boldsymbol{\mu}_{\mathbf{h}} = (\mu_{\mathbf{h},1}, \dots, \mu_{\mathbf{h},d})$  and diagonal covariance structure, *i.e.*,  $\boldsymbol{\Sigma}_{\mathbf{g}} = \text{diag}(\sigma_{\mathbf{g},1}^2, \dots, \sigma_{\mathbf{g},d}^2)$  and  
 1436  $\boldsymbol{\Sigma}_{\mathbf{h}} = \text{diag}(\sigma_{\mathbf{h},1}^2, \dots, \sigma_{\mathbf{h},d}^2)$ .  
 1437

1438 Then the expected value of the cosine similarity is:

$$1439 \mathbb{E}[S_{\text{cos}}(\mathbf{g}, \mathbf{h})] = \frac{\mathbb{E}[\mathbf{g}^{\top} \mathbf{h}]}{\mathbb{E}[\|\mathbf{g}\|] \mathbb{E}[\|\mathbf{h}\|]} \quad (84)$$

$$1442 = \frac{\sum_i^d \mu_{\mathbf{g},i} \mu_{\mathbf{h},i}}{\mathbb{E}[\|\mathbf{g}\|] \mathbb{E}[\|\mathbf{h}\|]}. \quad (85)$$

1444 Note that computing  $\mathbb{E}[\|\mathbf{x}\|]$  is intractable, and we, therefore, bound the expected value by application  
 1445 of the triangle inequality, *i.e.*,

$$1447 \mathbb{E}[\|\mathbf{x}\|] \leq \sqrt{\sum_i \mu_{\mathbf{x},i}^2 + \sigma_{\mathbf{x},i}^2}, \quad (86)$$

1449 where we use the fact that  $\mathbb{E}[x^2] = \mu_x^2 + \sigma_x^2$ . Consequently, we obtain an approximation to the  
 1450 expected value of the cosine similarity given by:  
 1451

$$1452 \mathbb{E}[S_{\text{cos}}(\mathbf{g}, \mathbf{h})] \approx \frac{\sum_i^d \mu_{\mathbf{g},i} \mu_{\mathbf{h},i}}{\sqrt{\sum_i \mu_{\mathbf{g},i}^2 + \sigma_{\mathbf{g},i}^2} \sqrt{\sum_i \mu_{\mathbf{h},i}^2 + \sigma_{\mathbf{h},i}^2}}. \quad (87)$$

1455 Next, we will derive the second moment (variance) of the cosine similarity of two random vectors.  
 1456 First, note that the variance can be written as the difference between two expectations, *i.e.*,  
 1457

$$\mathbb{V}\text{ar}[S_{\text{cos}}(\mathbf{g}, \mathbf{h})] = \mathbb{E}[S_{\text{cos}}(\mathbf{g}, \mathbf{h})^2] - \mathbb{E}[S_{\text{cos}}(\mathbf{g}, \mathbf{h})]^2, \quad (88)$$

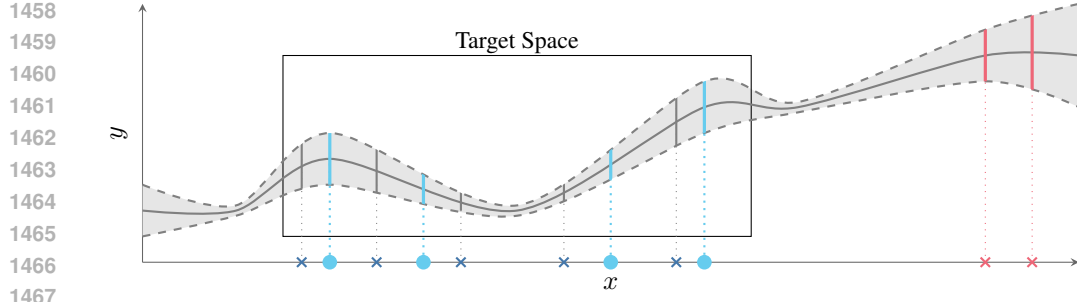


Figure 7: Illustration of targeted support set selection. We aim to select an **informative** support set that reduces the uncertainty over the predictions on the query set ●. Only focusing on the epistemic uncertainties would not lead to a good selection, as we would select **uninformative** support set candidates ✗ with high epistemic uncertainty. Hence, we target the selection process.

where the second expectation corresponds to:

$$\mathbb{E}[S_{\cos}(\mathbf{g}, \mathbf{h})]^2 \approx \frac{(\sum_i^d \mu_{\mathbf{g},i} \mu_{\mathbf{h},i})^2}{\sum_i \mu_{\mathbf{g},i}^2 + \sigma_{\mathbf{g},i}^2 \sum_i \mu_{\mathbf{h},i}^2 + \sigma_{\mathbf{h},i}^2}. \quad (89)$$

Next we can obtain  $\mathbb{E}[S_{\cos}(\mathbf{g}, \mathbf{h})^2]$  for which we will use the fact that  $\mathbb{E}[x^2] = \mu_x^2 + \sigma_x^2$  again, *i.e.*,

$$\mathbb{E}[S_{\cos}(\mathbf{g}, \mathbf{h})^2] = \frac{\mathbb{E}[(\mathbf{g}^\top \mathbf{h})^2]}{\sum_i \mu_{\mathbf{g},i}^2 + \sigma_{\mathbf{g},i}^2 \sum_i \mu_{\mathbf{h},i}^2 + \sigma_{\mathbf{h},i}^2} \quad (90)$$

where

$$\mathbb{E}[(\mathbf{g}^\top \mathbf{h})^2] = \sum_i \sum_j \mu_{\mathbf{g},i} \mu_{\mathbf{h},i} \mu_{\mathbf{g},j} \mu_{\mathbf{h},j} \quad (91)$$

$$+ \sum_i \sigma_{\mathbf{g},i}^2 \mu_{\mathbf{h},i}^2 + \mu_{\mathbf{g},i}^2 \sigma_{\mathbf{h},i}^2 + \sigma_{\mathbf{g},i}^2 \sigma_{\mathbf{h},i}^2. \quad (92)$$

Henceforth, we obtain the variance:

$$\text{Var}[S_{\cos}(\mathbf{g}, \mathbf{h})] = \frac{\sum_i \sigma_{\mathbf{g},i}^2 (\sigma_{\mathbf{h},i}^2 + \mu_{\mathbf{h},i}^2) + \sigma_{\mathbf{h},i}^2 \mu_{\mathbf{g},i}^2}{\sum_i \mu_{\mathbf{g},i}^2 + \sigma_{\mathbf{g},i}^2 \sum_i \mu_{\mathbf{h},i}^2 + \sigma_{\mathbf{h},i}^2}. \quad (93)$$

## D ACTIVE LEARNING DETAILS

We provide additional details on our active learning setup. Active learning provides a natural setting to evaluate the quality of uncertainty estimates, as it relies on selecting informative samples based on predictive uncertainty. We assess BayesVLM in this setting using acquisition functions from Bayesian active learning, combined with adaptive target region selection. Concretely, given a query set  $\mathcal{X}_{\text{test}} = \{x_i^*\}_{i=1}^{n_{\text{test}}}$  of unseen samples with unknown class labels, our goal is to select a support set  $\{(x_j, y_j)\}_{j=1}^m$  of labeled examples such that predictive uncertainty on  $\mathcal{X}_{\text{test}}$  is reduced. To this end, we first target the selection process toward the predictive distribution of the query set, and then select support candidates based on their estimated influence on predictive or model uncertainty.

We detail our method in three parts: [App. D.1](#) describes how we reduce the candidate pool by selecting samples that align with the target distribution; [App. D.2](#) outlines the acquisition functions used for (targeted) active fine-tuning; and [App. D.3](#) explains how we update the Laplace approximation in an online fashion during the EPIG acquisition process.

### D.1 TARGETED SELECTION

To target the active learning process towards relevant areas in the data space, we perform a  $k$ -nearest neighbours ( $k$ -NN) search around the test data. The main idea behind our adaptive targeted region selection is illustrated in [Fig. 7](#).

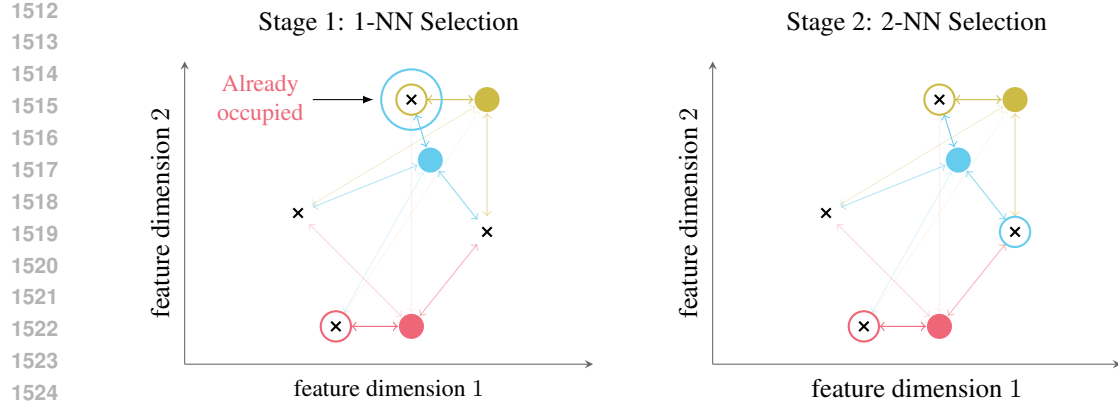


Figure 8: Illustration of the nearest neighbour-based support set selection for adaptive targeted selection. The circles  $\bullet$  show test data points with uncertainty scores depicted through their colours: **high**, **medium**, **low**. For each test datum we find the  $k = 1$  nearest neighbour from the support set candidates  $\times$ . If the  $k = 1$  nearest neighbour is already selected, we increase  $k$  for those with occupied neighbours and choose the second nearest neighbour, *i.e.*,  $k = 2$ . This recursion continues until every test datum has a selected support set candidate. The selected candidates are shown in coloured circles. Note that in the case of the **blue** test datum, the closest support set candidate has already been chosen by the **yellow**, and hence the second closest candidate is selected in the second stage.

Specifically, we greedily acquire an intermediate candidate set  $\mathcal{T}^* \subseteq \mathcal{D}_{\text{train}}$  using  $k$ -NN selection based on the test set  $\mathcal{D}_{\text{test}}$ . For this, we need to compute a metric comparing the random feature projections. We assessed two different ways, first by computing the 2-Wasserstein distance between the distributions of the embeddings and the second by computing the expected cosine similarity based on [App. C.3](#). Recall that for multivariate Gaussian distributions, the 2-Wasserstein distance exists in closed-form and is given as  $W_2^2(\mathcal{N}(\boldsymbol{\mu}_1, \boldsymbol{\Sigma}_1), \mathcal{N}(\boldsymbol{\mu}_2, \boldsymbol{\Sigma}_2)) =$

$$\|\mu_1 - \mu_2\|_2^2 + \text{tr} \left( \Sigma_1 + \Sigma_2 - 2(\Sigma_1^{1/2} \Sigma_2 \Sigma_1^{1/2})^{1/2} \right), \quad (94)$$

where  $\|\cdot\|_2$  denotes the Euclidean norm,  $\text{tr}(\cdot)$  is the trace operator, and  $\Sigma^{1/2}$  is the matrix square root of  $\Sigma$ . As computing the Wasserstein distance exactly is computationally and memory intensive due to the matrix square root, we approximate it by assuming both distributions to be isotropic. Hence, simplifying to  $\bar{W}_2^2(\mathcal{N}(\mu_1, \Sigma_1), \mathcal{N}(\mu_2, \Sigma_2)) =$

$$\sum_{i=1}^d (\mu_{1,i} - \mu_{2,i})^2 + \sigma_{1,i}^2 + \sigma_{2,i}^2 - 2\sigma_{1,i}\sigma_{2,i}, \quad (95)$$

where  $\Sigma_1 = \text{diag}(\sigma_{1,1}^2, \dots, \sigma_{1,J}^2)$  and  $\Sigma_2$  is given respectively.

Based on a selected metric, we select the training samples closest to the test set in the joint embedding space, resulting in:

$$\mathcal{T} = \bigcup_{g^* \in \mathcal{T}^*} N_k(g^*, \mathcal{D}_{\text{train}}), \quad (96)$$

with  $N_k(\mathbf{g}^*, \mathcal{D}_{\text{train}})$  denoting the set of  $k$ -nearest neighbours of  $\mathbf{g}^*$  in the training set  $\mathcal{D}_{\text{train}}$ . To ensure that we select  $k$  distinct data points for each test sample, we perform an iterative search in which we discard already selected training samples and iteratively increase the search radius until  $k$  distinct samples are found for each test datum. This process is illustrated in Fig. 8.

## D.2 ACQUISITION FUNCTIONS

Given a labelled pool  $\mathcal{D}_{\text{train}}$  and an unlabelled target set  $\mathcal{X}_{\text{test}} = \{x \mid (x, y) \in \mathcal{D}_{\text{test}}\}$ , the goal is to select  $m$  maximally informative samples from  $\mathcal{D}_{\text{train}}$  to reduce predictive uncertainty on  $\mathcal{X}_{\text{test}}$ . In this section, we provide a detailed explanation of the acquisition functions used for this purpose.

1566 **Naive random** For the *naive random* acquisition function, we randomly sample  $m$  data points from  
 1567 the train set  $\mathcal{D}_{\text{train}}$  to form the support set  $\mathcal{S}_{\text{ID}}$ .  
 1568

1569 **Targeted random** For the *targeted random* acquisition function, we randomly sample  $m$  data points  
 1570 from the unlabelled test set  $\mathcal{X}_{\text{test}}$  to form an intermediate support set  $\mathcal{T}^*$ . According to App. D.1, we  
 1571 then select the nearest neighbours to  $\mathcal{T}^*$  from the training set  $\mathcal{D}_{\text{train}}$  based on the cosine similarity of  
 1572 the normalized image embeddings to form the support set  $\mathcal{T}_{\text{t-ID}}$ .  
 1573

1574 **Targeted maximum entropy** For the *entropy* acquisition function, we compute the predictive  
 1575 entropy  $\mathcal{H}(y_i^* | \mathbf{x}_i^*)$  for each data point  $\mathbf{x}_i^* \in \mathcal{X}_{\text{test}}$  and select the  $m$  data points with the highest  
 1576 entropy. We use the predictive entropy on the MAP estimate of the model parameters to estimate the  
 1577 predictive entropy of the model:  
 1578

$$\begin{aligned} & \mathcal{H}(y | \mathbf{x}, \boldsymbol{\theta}_{\text{MAP}}) \\ &= - \sum_{c=1}^C p(y = c | \mathbf{x}, \boldsymbol{\theta}_{\text{MAP}}) \log p(y = c | \mathbf{x}, \boldsymbol{\theta}_{\text{MAP}}) \end{aligned} \quad (97)$$

1581 According to App. D.1, we then select the most similar data points from  $\mathcal{X}_{\text{train}}$  to form the support set  
 1582  $\mathcal{T}_{\text{t-entropy}}$ .  
 1583

1584 **BALD** We compute the BALD score (Houlsby et al., 2011) for each data point in  $\mathcal{X}_{\text{train}}$  and select the  
 1585  $m$  data points with the highest score. The score is approximated using nested Monte Carlo sampling,  
 1586 as in (Houlsby et al., 2011).  
 1587

$$\text{BALD}(\mathbf{x}) \quad (98)$$

$$= \mathbb{E}_{p(y|\mathbf{x})} [\mathcal{H}(p(\boldsymbol{\theta})) - \mathcal{H}(p(\boldsymbol{\theta} | \mathbf{x}, y))] \quad (99)$$

$$= \mathbb{E}_{p(\boldsymbol{\theta}|\mathcal{D})} [\mathcal{H}(p(y | \mathbf{x}, \boldsymbol{\theta})) - \mathcal{H}(p(y | \mathbf{x}, \mathcal{D}))] \quad (100)$$

1591 **Targeted BALD** We compute the BALD score (Eq. (100)) for each data point  $\mathbf{x}_i^* \in \mathcal{X}_{\text{test}}$  and select  
 1592 the  $m$  data points with the highest score. According to App. D.1, we then select the most similar data  
 1593 points from  $\mathcal{X}_{\text{train}}$  to form the support set  $\mathcal{T}_{\text{t-BALD}}$ .  
 1594

1595 **EPIG** The Expected Predictive Information Gain (EPIG) score (Bickford Smith et al., 2023) calculates  
 1596 the expected mutual information between the model parameters and the predictive distribution  
 1597 resulting from the acquisition of a training data point. This method is specifically designed to target  
 1598 relevant information, eliminating the need for a  $k$ -nearest neighbour search typically used in other  
 1599 acquisition functions. The EPIG score is given by  
 1600

$$\text{EPIG}(\mathbf{x}) = \mathbb{E}_{p_*(\mathbf{x}^*)p(y|\mathbf{x})} [\mathcal{H}(p(y^* | \mathbf{x}^*)) - \mathcal{H}(p(y^* | \mathbf{x}^*, \mathbf{x}, y))] \quad (101)$$

$$= \mathbb{E}_{p_*(\mathbf{x}^*)} [\text{D}_{\text{KL}}(p(y, y^* | \mathbf{x}, \mathbf{x}^*) \| p(y | \mathbf{x})p(y^* | \mathbf{x}^*))] \quad (102)$$

$$= \mathbb{E}_{p_*(\mathbf{x}^*)} \left[ \sum_{y \in \mathcal{Y}} \sum_{y^* \in \mathcal{Y}} p(y, y^* | \mathbf{x}, \mathbf{x}^*) \log \frac{p(y, y^* | \mathbf{x}, \mathbf{x}^*)}{p(y | \mathbf{x})p(y^* | \mathbf{x}^*)} \right] \quad (103)$$

1606 where  $p_*(\mathbf{x}^*)$  denotes the target input distribution. The EPIG score is approximated using Monte  
 1607 Carlo sampling, as detailed in (Bickford Smith et al., 2023). For the EPIG selection, we perform  
 1608 online updates to the model weights using the online Laplace as described in App. D.3.  
 1609

### D.3 ONLINE LAPLACE APPROXIMATION

1611 We use an online Laplace approximation to efficiently update the posterior distribution over the image  
 1612 projection matrix  $\mathbf{P}$  during active learning. Instead of recomputing the posterior from scratch after  
 1613 each support set update, we incrementally refine both the MAP estimate and the Kronecker-factored  
 1614 Hessian approximation using the newly selected datapoint. Concretely, we perform a gradient step to  
 1615 update  $\mathbf{P}_{\text{MAP}}$ , and adjust the Kronecker factors  $\mathbf{A}_{\text{IMG}}$  and  $\mathbf{B}_{\text{IMG}}$  based on the contribution of the new  
 1616 sample. This yields a computationally efficient approximation to the posterior over  $\mathbf{P}$  conditioned on  
 1617 the growing support set. Additionally, the prior precision can optionally be re-estimated after each  
 1618 update step, as commonly done in online Laplace methods (Immer et al., 2021; Lin et al., 2023). In  
 1619 the following, we outline the structure of the Laplace approximation and describe how it is updated  
 online during EPIG-based support set construction.

1620 Recall that we obtain from our post-hoc Laplace approximation the Kronecker factorized Hessian  
 1621 approximation  $\mathbf{H}_{\text{IMG}} \approx (\sqrt{\tau} \mathbf{A}_{\text{IMG}} + \sqrt{\lambda} \mathbf{I}) \otimes (\sqrt{\tau} \mathbf{B}_{\text{IMG}} + \sqrt{\lambda} \mathbf{I})$  with  
 1622

$$1623 \mathbf{A}_{\text{IMG}} = \frac{1}{\sqrt{n}} \sum_{i=1}^n \phi(\mathbf{x}_i^{\text{IMG}}) \phi(\mathbf{x}_i^{\text{IMG}})^\top \quad \text{and} \quad (104)$$

$$1624 \mathbf{B}_{\text{IMG}} = \frac{1}{\sqrt{n}} \sum_{i=1}^n \mathbf{J}_{\text{IMG}}(\mathbf{x}_i^{\text{IMG}})^\top \mathbf{\Lambda}_{\text{IMG}} \mathbf{J}_{\text{IMG}}(\mathbf{x}_i^{\text{IMG}}), \quad (105)$$

1625 approximating a posterior distribution over the projection weights:  
 1626

$$1627 \mathbf{P} \sim \mathcal{MN}(\mathbf{P}_{\text{MAP}}, \tilde{\mathbf{B}}_{\text{IMG}}^{-1}, \tilde{\mathbf{A}}_{\text{IMG}}^{-1}) \quad (106)$$

$$1628 \mathbf{Q} \sim \mathcal{MN}(\mathbf{Q}_{\text{MAP}}, \tilde{\mathbf{B}}_{\text{TXT}}^{-1}, \tilde{\mathbf{A}}_{\text{TXT}}^{-1}) \quad (107)$$

1629 with  $\tilde{\mathbf{A}}, \tilde{\mathbf{B}}$  denoting the Kronecker factors after applying  $\tau$  and  $\lambda$ .  
 1630

1631 Further, utilizing App. C.3 in combination with the generalized probit approximation (as described,  
 1632 for instance, in (Daxberger et al., 2021)), we obtain an analytical form for the predictive posterior  
 1633 distribution  $p(y | \mathbf{x}, \mathcal{D})$  of our few-shot classifier.

1634 Our goal with EPIG is to iteratively construct a support set  $\mathcal{T}_t$ , where  $t$  denotes the current number of  
 1635 selected training data points. We construct  $\mathcal{T}_t$  by greedily selecting the training datum that maximises  
 1636 the expected information gain on the predictive distribution in the target domain:  
 1637

$$1638 \mathbf{x}_{t+1} = \arg \max_{\mathbf{x} \in \mathcal{D}_{\text{train}}} \text{EPIG}(\mathbf{x} | \mathcal{T}_t) \quad (108)$$

$$1639 = \arg \max_{\mathbf{x} \in \mathcal{D}_{\text{train}}} \mathbb{E}_{p^*(\mathbf{x}^*)p(y|\mathbf{x})} [\mathcal{H}(p(y^* | \mathbf{x}^*, \mathcal{T}_t)) - \mathcal{H}(p(y^* | \mathbf{x}^*, \mathcal{T}_t \cup \{(\mathbf{x}, y)\}))] \quad (109)$$

1640 and obtain the corresponding label  $y_{t+1}$ , forming the support set  $\mathcal{T}_{t+1} = \mathcal{T}_t \cup \{(\mathbf{x}_{t+1}, y_{t+1})\}$ .  
 1641

1642 The integration of  $\{(\mathbf{x}_{t+1}, y_{t+1})\}$  into the few-shot training set changes the posterior distribution  
 1643 over the image projection. To obtain the updated posterior distribution  
 1644

$$1645 \mathbf{P} | \mathcal{T}_{t+1} \sim \mathcal{MN}(\mathbf{P}_{\text{MAP}}, \tilde{\mathbf{B}}_{\text{IMG}, t+1}^{-1}, \tilde{\mathbf{A}}_{\text{IMG}, t+1}^{-1}), \quad (110)$$

1646 we utilise the following online updates to the projection weights and the Laplace approximation:  
 1647

$$1648 \mathbf{P}_{\text{MAP}, t+1} = \mathbf{P}_{\text{MAP}, t} - \gamma \nabla_{\mathbf{P}} \mathcal{L}(\mathbf{x}_{t+1}^{\text{IMG}}, \mathbf{X}^{\text{TXT}}) \quad (111)$$

$$1649 \mathbf{A}_{\text{IMG}, t+1} = \frac{\sqrt{n+t} \mathbf{A}_{\text{IMG}, t} + \beta \mathbf{A}_{\mathbf{x}_{t+1}}}{\sqrt{n+t+1}} \quad (112)$$

$$1650 \mathbf{B}_{\text{IMG}, t+1} = \frac{\sqrt{n+t} \mathbf{B}_{\text{IMG}, t} + \beta \mathbf{B}_{\mathbf{x}_{t+1}}}{\sqrt{n+t+1}}. \quad (113)$$

1651 where  $\gamma \geq 0$  and  $\beta \geq 0$  are hyperparameters and  
 1652

$$1653 \mathbf{A}_{\mathbf{x}_{t+1}} = \phi(\mathbf{x}_{t+1}^{\text{IMG}}) \phi(\mathbf{x}_{t+1}^{\text{IMG}})^\top \quad (114)$$

$$1654 \mathbf{B}_{\mathbf{x}_{t+1}} = \mathbf{J}_{\text{IMG}}(\mathbf{x}_{t+1}^{\text{IMG}})^\top \mathbf{\Lambda}_{\text{IMG}} \mathbf{J}_{\text{IMG}}(\mathbf{x}_{t+1}^{\text{IMG}}). \quad (115)$$

## 1655 E EXPERIMENTAL DETAILS

1656 This section details the experimental setup used in our study. In App. E.1, we describe the pre-trained  
 1657 vision-language models and checkpoints used. App. E.2 explains how we computed the Hessian  
 1658 matrices required for the Laplace approximation. In App. E.3, we outline how we selected the Laplace  
 1659 parameters, such as the pseudo-data count  $\tau$  and prior precision  $\lambda$ . App. E.4 describes our active  
 1660 learning setup, including dataset preparation, selection strategies, and training hyperparameters (see  
 1661 Table 6).  
 1662

1663 We run experiments on a compute cluster with NVIDIA P100 16GB, V100 32 GB, and A100 80GB  
 1664 GPUs. We used V100 or A100 GPUs for the Huge model variants and the ImageNet experiments.  
 1665

1674  
1675

## E.1 PRE-TRAINED VISION-LANGUAGE MODELS

1676  
1677  
1678  
1679

In this work, we used the OpenCLIP (Ilharco et al., 2021) implementations of CLIP (Radford et al., 2021), which was published under the MIT license. We present additional experimental results on the HuggingFace implementation of SigLIP (Zhai et al., 2023), which was originally published under the Apache2 license.

1680  
1681  
1682  
1683  
1684

For PCME++, we used the CLIP ViT-B/16 checkpoint provided by the authors with uncertainty adapter trained on CC-3M (Sharma et al., 2018), CC-12M (Changpinyo et al., 2021), and Redcaps (Desai et al., 2021). For ProLIP, we used the ViT-B/16 model checkpoint released by the authors at <https://github.com/naver-ai/prolip>, which shares the same backbone architecture.

1685  
1686

## E.2 ESTIMATION OF THE HESSIAN MATRICES

1687  
1688  
1689  
1690  
1691  
1692

We estimated the Hessians separately for the CLIP image and text encoders using the pre-training dataset LAION-400M (Schuhmann et al., 2022) published under MIT license. For this estimation, we randomly sampled a subset of 327.680 data points. The pre-training dataset was filtered to exclude NSFW content. For the Laplace approximation, we used the GGN approximation of the Hessian matrices as described in App. C.2 and estimated the covariance matrices  $A$  and  $B$  for the image and text encoders.

1693  
1694

## E.3 ESTIMATION OF THE HESSIAN PARAMETERS

1695  
1696  
1697  
1698  
1699  
1700  
1701  
1702  
1703

To ensure that both zero-shot and active learning experiments rely on a well-calibrated posterior covariance, we estimated the pseudo-data count (Ritter et al., 2018),  $\tau$ , by performing a grid search over values in  $\tau \in [1, 5, 10, 15, \dots, 200]$ . In the active learning experiments, the step size was reduced to 2. The optimal value of  $\tau$  was selected by minimizing the negative log predictive density (NLPD) on a random subset of ImageNet consisting of 100 classes and 1097 test data points in total as a proxy. App. E.3 presents two plots illustrating the NLPD as a function of the pseudo-data count for SigLIP-Base and CLIP-Base, respectively. Once this optimal  $\tau$  was identified, we further optimised the prior precision,  $\lambda$ , using the marginal likelihood on the LAION-400M (Schuhmann et al., 2022) dataset.

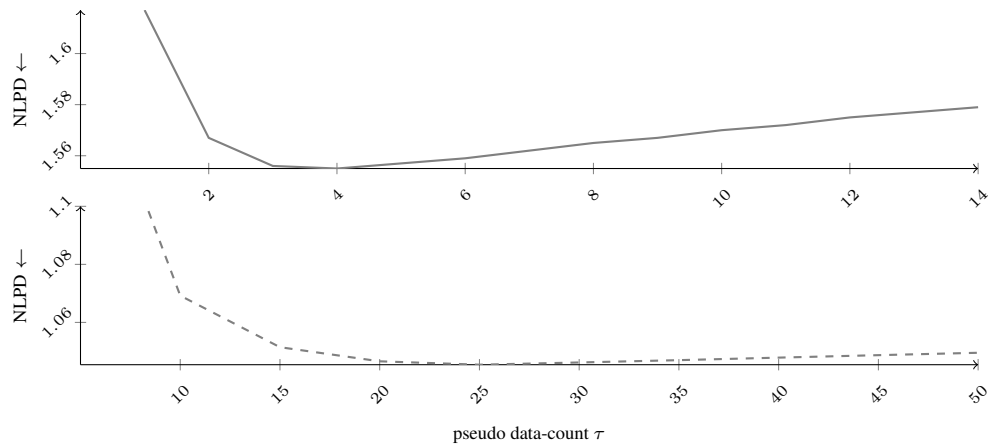
1704  
1705  
1706  
1707  
1708  
1709  
1710  
1711  
1712  
1713  
1714  
1715  
1716  
1717  
17181719  
1720  
1721  
1722  
1723

Figure 9: Grid search over the pseudo-data count parameter  $\tau$  for CLIP-Base (—) and SigLIP-Base (---). The optimal NLPD for CLIP-Base is identified at  $\tau = 10$ , while the optimal NLPD for SigLIP-Base is identified at  $\tau = 100$ .

1724  
1725

## E.4 ACTIVE LEARNING EXPERIMENTS

1726  
1727

We conducted active learning experiments on the OfficeHome data set (Venkateswara et al., 2017), which consists of the domains: art, clipart, product, and real-world, as well as on the ImageNet dataset with the domains ImageNet-R (Hendrycks et al., 2021) and ImageNet-Sketch (Wang et al., 2019). For

these experiments, all training sets from the respective domains were combined into a single, large training set, and the projection layer of either CLIP or SigLIP was fine-tuned for a specific domain. Data selection was performed based on the acquisition functions described in App. D.2. Performance was evaluated at the checkpoint corresponding to the lowest NLPD on a domain-specific validation set. We also performed a grid search for the online learning parameters of the EPIG acquisition rule, selecting the EPIG learning rate  $\gamma$  from the range  $[1e-5, 1e-4, 1e-3, 1e-2]$  and the EPIG Hessian update scale  $\beta$  from  $[1, 10, 100, 1000]$ , based on the NLPD on the domain-specific validation set. Details on the training hyperparameter settings are given in Table 6.

Table 6: Active fine-tuning hyperparameters.

config	value
optimiser	AdamW
learning rate	$1e-5$
weight decay	$5e-2$
optimiser momentum	$\beta_1, \beta_2 = 0.9, 0.999$
batch size	32
epochs	100

## F ADDITIONAL RESULTS

In this Appendix, we provide additional results to support the findings in the main paper. Specifically, we detail (i) the approximation quality of the Gaussian approximation to the distribution over cosine similarities in App. F.1, (ii) the active learning experiments in App. F.2, (iii) the ablation of the  $k$ -NN distance metric in App. F.3, (iv) the influence of the number of data points used for Hessian estimation in App. F.4, (v) the runtime overhead and inference costs of BayesVLM compared to the baselines in App. F.5, and (vi) additional zero-shot learning results in App. F.7 to demonstrate the generality of our approach.

### F.1 APPROXIMATION QUALITY

To assess the approximation quality of the Gaussian approximation to the distribution over cosine similarities, we generated 500 samples for the image and text feature distributions for a given input. For the resulting samples, we then computed the respective cosine similarity for each pair and performed kernel density estimation with a Gaussian kernel and length scale of 0.3 on the similarity scores. We added increasing shifts to the distribution mean to evaluate the change in the approximation quality under varying cosine similarity values. The results are depicted in Fig. 10. We can observe that our approximation through ProbCosine results qualitatively in a low approximation error.

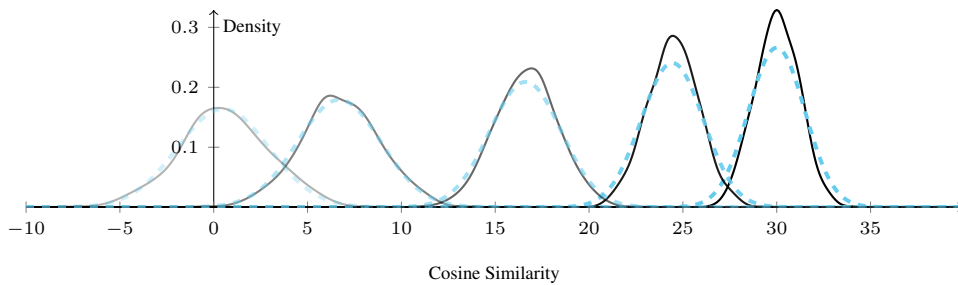


Figure 10: Approximation quality of the Gaussian approximation (ProbCosine) (---) to the distribution over cosine similarities compared to KDE over samples (—) for image-text pairs with increasing Euclidean distance between their feature projection means ( $\mu_g, \mu_h$ ).

1782  
1783

## F.2 ACTIVE LEARNING EXPERIMENTS

1784  
1785  
1786  
1787  
1788

We report the active learning results for CLIP-Huge in Fig. 13 and for SigLIP-Base in Fig. 14. For CLIP-Huge, we observe that active learning based on our post-hoc uncertainties consistently improves upon random and entropy-based selection. For SigLIP-Base, we observe significant improvements in terms of accuracy and NLPD on the ImageNet version with active learning based on our post-hoc uncertainties.

1789

1790  
1791F.3 ABLATION OF THE  $k$ -NN DISTANCE METRIC1792  
1793  
1794  
1795  
1796  
1797

We performed an ablation study on the  $k$ -NN distance metric for our proposed targeted selection in Sec. 3.3 while fixing the *online LA learning rate*  $\gamma = 1e-4$  and the *online LA pseudo-data count*  $\beta = 10$ . We evaluate performance using two distance metrics: Wasserstein and cosine similarity. Results are reported for EPIG and BALD, with Wasserstein (*solid lines*) and cosine (*dashed lines*) metrics. While Wasserstein-based  $k$ -NN selection demonstrates improved performance for datasets such as OfficeHome-Art and ImageNet-R, no clear trend is observed across the other datasets.

1798

1799

## F.4 NUMBER OF DATA POINTS FOR HESSEAN ESTIMATION

1800  
1801  
1802  
1803  
1804  
1805  
1806  
1807

We assessed the influence of the number of data points used to estimate the Hessian by estimating the trace of the Hessian using a varying number of data points for 10 random subsets of the Laion400m data set. Fluctuations of the estimated trace can be understood as an indicator that the Hessian estimates are unreliable. Fig. 11 shows that the trace of both the Hessian over the image projection and the text projection quickly converges to a stable value with low fluctuations, as seen by the low variance and stable mean. Moreover, the results indicate that 10 mini-batches suffice to obtain a reliable estimate of the Hessians.

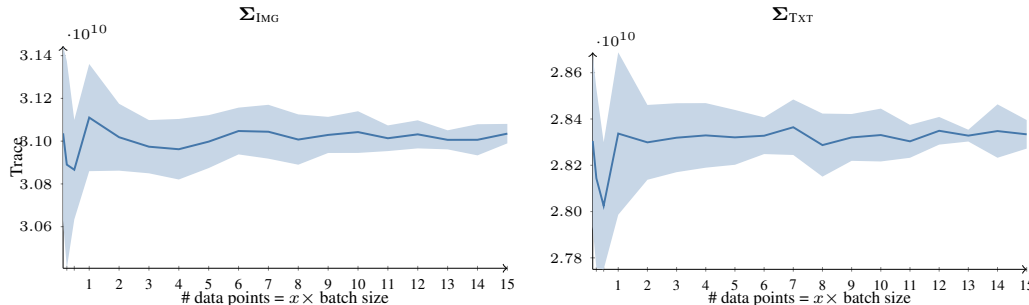
1808  
1809  
1810  
1811  
1812  
1813  
1814  
1815  
1816  
18171818  
1819  
1820

Figure 11: Hessian (Trace) vs. number of samples. Error bars indicate  $\pm 1$  standard deviation over 10 random subsets of Laion400m.

1821

1822  
1823

## F.5 RUNTIME OVERHEAD

1824  
1825  
1826  
1827  
1828  
1829

We compared our approach against the vanilla CLIP. We report runtimes on CIFAR-100 with CLIP-Huge-/Base on a Tesla V100 with 3 warmup steps and averaged over 1000 runs (batch size 1) in Table 7. Indicating minimal computational overhead. In addition, we present inference costs in GFLOPs, comparing the original VLM (deterministic) against TTA and BayesVLM in Table 8. We find that BayesVLM results in comparable inference costs, while TTA has an 80-fold increase in the inference cost.

1830  
1831  
1832  
1833  
1834  
1835

Table 7: Average runtime measured in seconds on CIFAR-100.

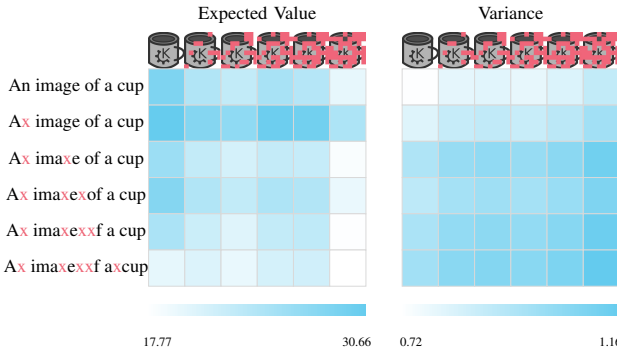
Model	Vanilla	BayesVLM	rel. increase
CLIP-Huge	43.8178	43.9712	0.35%
CLIP-Bas	9.4498	9.8929	4.69%

1836 Table 8: Inference computational cost per image on CIFAR-100 (in GFLOPs  $10^9$ ).  
1837

Model	Vanilla	TTA (FARINA ET AL., 2024)	BAYESVLM
CLIP-Base	8.83	687.78	8.84
CLIP-Lage	162.06	12638.00	162.07
CLIP-Huge	334.71	26098.06	334.72
SigLIP-Base	47.00	3652.05	47.03

1843  
1844 F.6 INTERPRETING PROBABILISTIC COSINE SIMILARITIES  
1845

1846 We qualitatively assessed the distribution obtained by ProbCosine on a randomly selected test example  
1847 from the OfficeHome clipart domain, evaluating the mean and variance of the cosine similarity under  
1848 increasing corruption in both image and text domains. Text corruption was introduced by randomly  
1849 replacing characters with ‘x’, and image corruption by randomly adding grey squares. Fig. 12 shows  
1850 the mean and variance of cosine similarities as corruption increases. We observe that the expected  
1851 cosine similarity generally decreases and variance increases with more corruption, indicating that  
1852 our approximation effectively captures model uncertainties under distribution shift. Note that we  
1853 observe a slight increase in the cosine similarity after one character has been replaced, indicating that  
1854 performing predictions solely on the expected cosine similarity can be problematic. In this case, the  
1855 variance over cosine similarities can capture the change in the input, highlighting the importance of  
1856 capturing and propagating the model uncertainties.

1869 Figure 12: Illustration of ProbCosine under increasing corruption. The mean similarity decreases and  
1870 variance increases with higher levels of corruption, demonstrating effective uncertainty estimation  
1871 under distribution shift.  
1872  
18731874 F.7 ADDITIONAL ZERO-SHOT RESULTS  
1875

1876 Here, we report additional zero-shot results for CLIP-huge and SigLIP-base in Table 9 and Table 10,  
1877 respectively. We also report the results for applying our *ProbCosine* to the ProLIP (Chun et al., 2025)  
1878 model in Table 11.

1879 **CLIP-huge results** In Table 9, BayesVLM consistently matches or outperforms baseline methods  
1880 in terms of accuracy (ACC), negative log predictive density (NLPD), and expected calibration error  
1881 (ECE). We note that TTA achieves worse ACC than CLIP on CIFAR-10 and -100, which we believe  
1882 is due to test-time augmentation in (Farina et al., 2024) not being optimised for small images (32x32),  
1883 where the classes could become unrecognisable with additional cropping in the augmentation.

1884 **SigLIP-base results** In Table 10, for SigLIP, BayesVLM still yields improvements on several  
1885 benchmarks (despite using proxy data for Hessian estimation, as the original training set is not  
1886 publicly available), demonstrating robustness to such settings. Despite mismatched training and  
1887 Hessian estimation datasets, BayesVLM remains competitive, especially on CIFAR-10, UCF101, and  
1888 SUN397, effectively improving calibration without sacrificing predictive performance. We note that  
1889 TTA achieves better ACC on some benchmarks, which is sensible since the model will get better at  
predicting the correct class average with more chances (augmentations).

1890 **ProbCosine combined with ProLIP results** In Table 11, we observe that applying ProbCosine to  
 1891 ProLIP improves zero-shot performance across classification benchmarks and metrics.  
 1892

1893 **Table 9: Zero-shot Results:** Quantitative evaluation of uncertainty estimation across multiple data  
 1894 sets in the zero-shot setting for the OpenCLIP ViT-L-14 model. Our proposed BayesVLM consistently  
 1895 outperforms baseline methods across accuracy (ACC, in %), negative log predictive density (NLPD),  
 1896 and expected calibration error (ECE, in %) metrics.

Metrics	Methods	FLOWERS-102	FOOD-101	CIFAR-10	CIFAR-100	IMAGENET-R	UCF101	SUN397
ACC $\uparrow$	CLIP (Radford et al., 2021)	<b>72.04</b> $\pm$ 0.5723	86.60 $\pm$ 0.2144	<b>95.57</b> $\pm$ 0.2058	<b>76.74</b> $\pm$ 0.4225	85.51 $\pm$ 0.4065	<b>69.60</b> $\pm$ 0.7479	71.48 $\pm$ 0.3205
	CLIP (temp. scaling)	<b>72.04</b> $\pm$ 0.5723	86.60 $\pm$ 0.2144	<b>95.57</b> $\pm$ 0.2058	<b>76.74</b> $\pm$ 0.4225	85.51 $\pm$ 0.4065	<b>69.60</b> $\pm$ 0.7479	71.48 $\pm$ 0.3205
	TTA (Farina et al., 2024)	71.85 $\pm$ 0.5735	<b>87.11</b> $\pm$ 0.2109	92.83 $\pm$ 0.2580	71.56 $\pm$ 0.4511	<b>87.64</b> $\pm$ 0.2800	<b>70.10</b> $\pm$ 0.7443	<b>71.99</b> $\pm$ 0.3187
	BayesVLM	<b>72.42</b> $\pm$ 0.4469	<b>87.20</b> $\pm$ 0.3341	<b>95.49</b> $\pm$ 0.2075	<b>76.77</b> $\pm$ 0.4223	85.63 $\pm$ 0.3508	<b>70.26</b> $\pm$ 0.4571	71.12 $\pm$ 0.4532
NLPD $\downarrow$	CLIP (Radford et al., 2021)	1.75 $\pm$ 0.0479	0.48 $\pm$ 0.0083	<b>0.15</b> $\pm$ 0.0072	0.90 $\pm$ 0.0178	0.58 $\pm$ 0.0174	1.36 $\pm$ 0.0391	1.02 $\pm$ 0.0128
	CLIP (temp. scaling)	<b>1.51</b> $\pm$ 0.0378	0.47 $\pm$ 0.0065	<b>0.15</b> $\pm$ 0.0056	<b>0.87</b> $\pm$ 0.0143	0.59 $\pm$ 0.0144	<b>1.20</b> $\pm$ 0.0298	<b>0.96</b> $\pm$ 0.0098
	TTA (Farina et al., 2024)	1.74 $\pm$ 0.0472	0.49 $\pm$ 0.0086	0.24 $\pm$ 0.0080	1.15 $\pm$ 0.0188	<b>0.49</b> $\pm$ 0.0160	1.34 $\pm$ 0.0390	1.06 $\pm$ 0.0133
	BayesVLM	1.62 $\pm$ 0.0335	<b>0.45</b> $\pm$ 0.0110	<b>0.15</b> $\pm$ 0.0061	<b>0.87</b> $\pm$ 0.0155	0.57 $\pm$ 0.0132	1.22 $\pm$ 0.0204	0.98 $\pm$ 0.0154
ECE $\downarrow$	CLIP (Radford et al., 2021)	9.47	3.07	0.97	5.73	2.13	10.72	8.60
	CLIP (temp. scaling)	4.90	3.00	1.35	2.55	5.21	<b>3.40</b>	<b>1.48</b>
	TTA (Farina et al., 2024)	11.96	3.77	1.21	3.92	<b>1.92</b>	11.87	10.53
	BayesVLM	<b>4.66</b>	<b>1.00</b>	<b>0.62</b>	<b>1.91</b>	2.15	5.37	3.89

1905 **Table 10: Zero-shot results:** Quantitative evaluation of uncertainty estimation across multiple  
 1906 data sets in the zero-shot setting for the SigLIP-Base model (Zhai et al., 2023). Our proposed  
 1907 BayesVLM often performs competitively to baseline methods across accuracy (ACC, in %), negative  
 1908 log predictive density (NLPD), and expected calibration error (ECE, in %) metrics.  
 1909

Metrics	Methods	FLOWERS-102	FOOD-101	CIFAR-10	CIFAR-100	IMAGENET-R	UCF101	SUN397
ACC $\uparrow$	SigLIP (Zhai et al., 2023)	<b>82.31</b> $\pm$ 0.4867	88.81 $\pm$ 0.1984	<b>93.20</b> $\pm$ 0.2517	<b>71.27</b> $\pm$ 0.4525	89.71 $\pm$ 0.3509	<b>59.61</b> $\pm$ 0.7978	<b>67.55</b> $\pm$ 0.3323
	SigLIP (temp. scaling)	<b>82.31</b> $\pm$ 0.4867	88.81 $\pm$ 0.1984	<b>93.20</b> $\pm$ 0.2517	<b>71.27</b> $\pm$ 0.4525	89.71 $\pm$ 0.3509	<b>59.61</b> $\pm$ 0.7978	<b>67.55</b> $\pm$ 0.3323
	TTA (Farina et al., 2024)	<b>82.66</b> $\pm$ 0.4828	<b>89.24</b> $\pm$ 0.1950	87.96 $\pm$ 0.3254	60.95 $\pm$ 0.4879	<b>90.91</b> $\pm$ 0.3230	<b>60.14</b> $\pm$ 0.7960	66.82 $\pm$ 0.3342
	BayesVLM	<b>82.44</b> $\pm$ 0.3805	88.84 $\pm$ 0.3148	<b>93.16</b> $\pm$ 0.2524	<b>71.22</b> $\pm$ 0.4527	89.72 $\pm$ 0.3037	<b>59.69</b> $\pm$ 0.4905	<b>67.44</b> $\pm$ 0.4686
NLPD $\downarrow$	SigLIP (Zhai et al., 2023)	0.88 $\pm$ 0.0285	0.38 $\pm$ 0.0061	<b>0.21</b> $\pm$ 0.0063	<b>1.08</b> $\pm$ 0.0168	0.41 $\pm$ 0.0139	1.90 $\pm$ 0.0438	1.12 $\pm$ 0.0117
	SigLIP (temp. scaling)	<b>0.84</b> $\pm$ 0.0246	0.40 $\pm$ 0.0054	0.22 $\pm$ 0.0057	1.09 $\pm$ 0.0152	0.43 $\pm$ 0.0125	<b>1.77</b> $\pm$ 0.0376	1.12 $\pm$ 0.0102
	TTA (Farina et al., 2024)	<b>0.85</b> $\pm$ 0.0276	<b>0.37</b> $\pm$ 0.0064	0.36 $\pm$ 0.0073	1.62 $\pm$ 0.0209	<b>0.37</b> $\pm$ 0.0134	1.88 $\pm$ 0.0430	1.18 $\pm$ 0.0124
	BayesVLM	0.86 $\pm$ 0.0210	0.39 $\pm$ 0.0099	<b>0.21</b> $\pm$ 0.0061	<b>1.08</b> $\pm$ 0.0163	0.41 $\pm$ 0.0114	1.82 $\pm$ 0.0248	<b>1.12</b> $\pm$ 0.0154
ECE $\downarrow$	SigLIP (Zhai et al., 2023)	<b>4.31</b>	1.66	<b>0.92</b>	1.97	<b>1.36</b>	12.72	3.82
	SigLIP (temp. scaling)	6.28	5.54	2.94	4.47	4.85	<b>6.69</b>	2.83
	TTA (Farina et al., 2024)	4.56	<b>0.72</b>	3.14	2.09	1.59	13.47	6.81
	BayesVLM	4.87	3.49	1.38	<b>1.52</b>	2.79	9.60	<b>1.14</b>

1918 **Table 11: Can ProbCosine improve the zero-shot performance of pre-trained probabilistic  
 1919 models? Yes.** Applying ProbCosine to the ProLIP (Chun et al., 2025) model improves zero-shot  
 1920 performance across classification benchmarks and metrics.  
 1921

Metrics	Methods	FLOWERS-102	FOOD-101	CIFAR-10	CIFAR-100	IMAGENET-R	UCF101	SUN397
ACC $\uparrow$	Mean (Chun et al., 2025)	<b>77.83</b> $\pm$ 0.0053	<b>90.38</b> $\pm$ 0.0019	<b>96.52</b> $\pm$ 0.0018	<b>82.41</b> $\pm$ 0.0038	84.76 $\pm$ 0.0042	<b>69.94</b> $\pm$ 0.0033	<b>65.93</b> $\pm$ 0.0077
	ProbCosine (Eq. (10))	<b>77.74</b> $\pm$ 0.0053	<b>90.35</b> $\pm$ 0.0019	<b>96.52</b> $\pm$ 0.0018	<b>82.48</b> $\pm$ 0.0038	<b>84.91</b> $\pm$ 0.0041	<b>69.99</b> $\pm$ 0.0033	<b>65.82</b> $\pm$ 0.0077
	Mean (Chun et al., 2025)	1.36 $\pm$ 0.0411	<b>0.33</b> $\pm$ 0.0060	0.11 $\pm$ 0.0052	0.64 $\pm$ 0.0148	<b>0.59</b> $\pm$ 0.0164	1.05 $\pm$ 0.0120	1.28 $\pm$ 0.0316
	ProbCosine (Eq. (10))	<b>1.28</b> $\pm$ 0.0376	0.34 $\pm$ 0.0055	<b>0.11</b> $\pm$ 0.0047	<b>0.63</b> $\pm$ 0.0133	0.60 $\pm$ 0.0151	<b>1.02</b> $\pm$ 0.0108	<b>1.24</b> $\pm$ 0.0286
ECE $\downarrow$	Mean (Chun et al., 2025)	5.31	<b>0.79</b>	<b>0.60</b>	3.38	<b>1.08</b>	5.99	7.99
	ProbCosine (Eq. (10))	<b>3.60</b>	2.57	0.76	<b>1.40</b>	3.53	<b>2.23</b>	<b>4.73</b>

## F.8 ROBUSTNESS WRT TO PSEUDO-DATA COUNT

1926 To examine the influence of the pseudo-data count  $\tau$  on BayesVLM, we evaluated BayesVLM with  
 1927 the CLIP-Base configuration on four datasets (FLOWERS-102, FOOD-101, CIFAR-10, CIFAR-  
 1928 100) while varying  $\tau \in \{1, 3, 5, 7, 9\}$ . For each setting, we report classification accuracy (ACC  $\uparrow$ ),  
 1929 negative log predictive density (NLPD  $\downarrow$ ), and expected calibration error (ECE  $\downarrow$ ) in Table 12.  
 1930

1931 The results show that performance is stable across the tested range of pseudo-data counts. Accu-  
 1932 racy and calibration metrics vary only slightly with  $\tau$ , indicating that the method is robust to this  
 1933 hyperparameter. In the main manuscript, we used  $\tau = 4$  as the default setting. We find that slight  
 1934 improvements can be observed when moving the pseudo-data count away from  $\tau = 4$ , but the value  
 1935 found on the proxy dataset ( $\tau = 4$ ) provides reasonable performance in general.  
 1936

## F.9 ROBUSTNESS WRT THE NUMBER OF NEGATIVE SAMPLES

1937 To assess the impact of negative samples on the likelihood approximation, we vary the batch size  
 1938  $K \in \{32768, 8192, 2048\}$  and estimate the posterior from 1–5 random batches, reporting mean and  
 1939 standard deviation over five trials. Because the posterior depends on the number of negatives only  
 1940 through the Hessian  $B$ -factor (cf. Eq. (5)), we present the normalised trace ( $\frac{\text{tr}(B_{i \times K})}{\text{tr}(B_{5 \times K})}$ ). Ideally, this

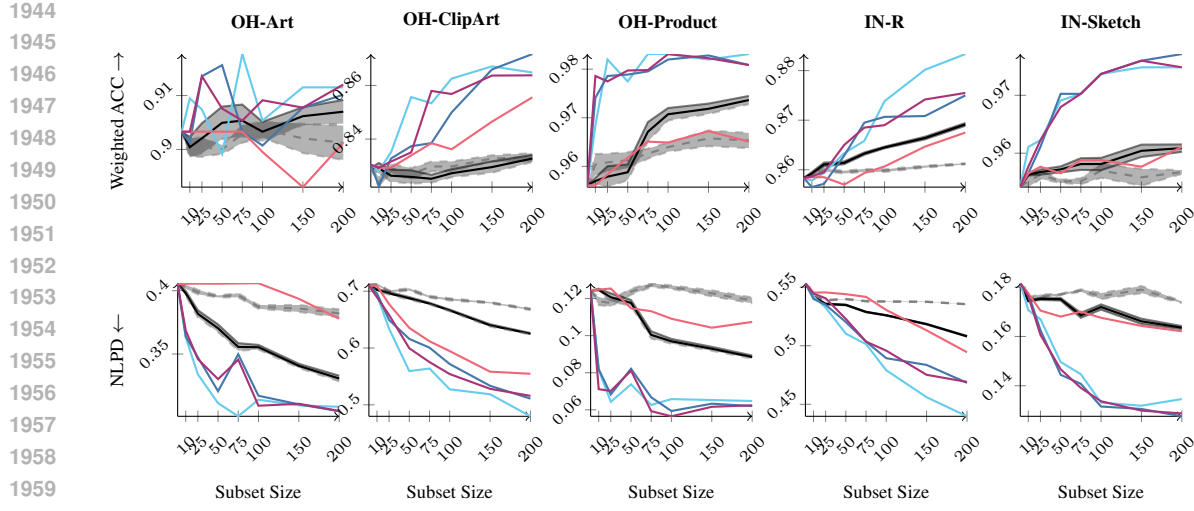


Figure 13: **Active learning results (CLIP Huge):** We present results for EPIG (—), BALD (—), Entropy (targeted) (—), Entropy (—), Random selection (targeted) (—), Random selection (—) on the OfficeHome dataset (OH) and ImageNet variants (IN). We observe that active learning based on our post-hoc uncertainties consistently improves upon random and entropy-based selection.

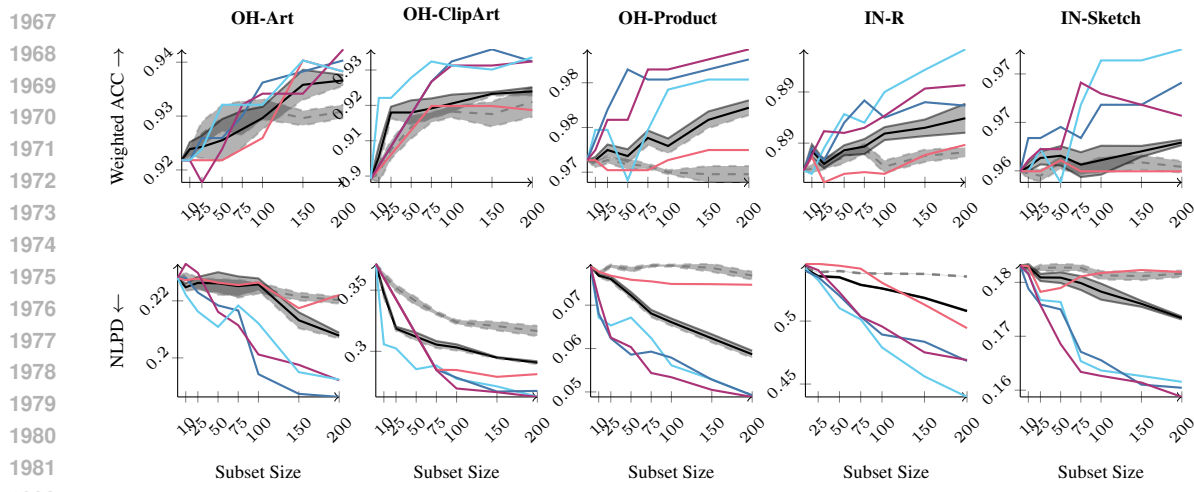


Figure 14: **Active learning results (SigLIP Base):** We present results for EPIG (—), BALD (—), Entropy (targeted) (—), Entropy (—), Random selection (targeted) (—), Random selection (—) on the OfficeHome dataset (OH) and ImageNet variants (IN).

ratio equals one with zero variance. Results for the image and text surrogate models are shown in Fig. 16a and Fig. 16b, respectively.

The batch size 32768 yields mean values near one for all numbers of random batches and maintains low standard deviations, indicating reliable estimates for both modalities.

## F.10 ADDITIONAL EXPERIMENTS ON CC12M

We find that BayesVLM provided robust uncertainty estimates for CLIP even when estimated on the proxy dataset, cf., Table 13.

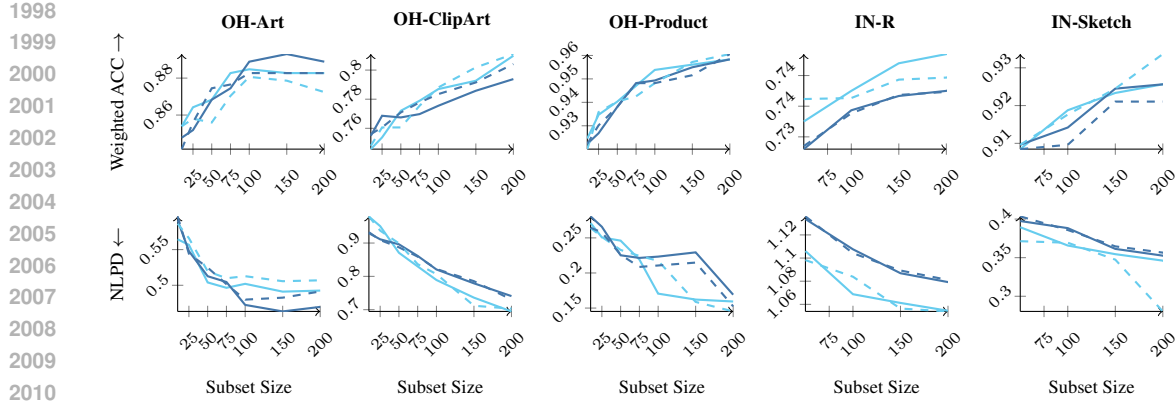


Figure 15: Ablation study on the  $k$ -NN distance metric, fixing the *online LA learning rate*  $\gamma = 1e-4$  and the *online LA pseudo-data count*  $\beta = 10$ . Results are shown for EPIG (Wasserstein) (—), EPIG (cosine) (---), BALD (Wasserstein) (—), and BALD (cosine) (---). As shown in Fig. 15, Wasserstein-based  $k$ -NN selection demonstrates improved performance for datasets such as *OH-Art* and *IN-R*, while no clear trend is observed across the other datasets.

Table 12: Zero-shot CLIP-Base performance versus pseudo-count on four datasets.

Pseudo Count	FLOWERS-102			FOOD-101			CIFAR-10			CIFAR-100		
	ACC↑	NLPD↓	ECE↓	ACC↑	NLPD↓	ECE↓	ACC↑	NLPD↓	ECE↓	ACC↑	NLPD↓	ECE↓
1	69.04±0.59	1.75±0.04	3.98	80.62±0.25	0.67±0.01	0.85	93.58±0.25	0.20±0.01	0.70	73.82±0.44	0.95±0.02	2.58
3	69.43±0.59	1.81±0.05	3.78	80.45±0.25	0.68±0.01	1.67	93.60±0.24	0.20±0.01	1.10	73.80±0.44	0.95±0.02	4.31
5	69.54±0.59	1.83±0.05	3.97	80.37±0.25	0.68±0.01	2.31	93.60±0.24	0.20±0.01	1.20	73.82±0.44	0.96±0.02	4.82
7	69.36±0.59	1.84±0.05	4.50	80.34±0.25	0.68±0.01	2.63	93.60±0.24	0.21±0.01	1.25	73.81±0.44	0.96±0.02	5.10
9	69.43±0.59	1.85±0.05	4.60	80.33±0.25	0.68±0.01	2.81	93.61±0.24	0.21±0.01	1.27	73.79±0.44	0.96±0.02	5.29

## F.11 ROBUSTNESS W.R.T. DISTRIBUTION SHIFT OF THE PROXY DATASET

Most OpenCLIP models are trained on the LAION-400M dataset, which allows us to directly estimate the Hessians on this distribution. However, some large CLIP variants are trained on closed-source data, requiring the use of a proxy dataset. As shown in Table 13, BayesVLM remains effective in a simulated closed-source setting, where we estimate the Hessians using the CC12M dataset.

To further analyse robustness, we conduct additional experiments in which we progressively distort the images of the LAION-400M dataset using different augmentations before estimating the Laplace Hessians: **GRAYSCALE** (interpolating between the RGB variant and the Grayscale variant with intensity coefficients in  $\{0, 0.2, 0.4, 0.6, 0.8, 1.0\}$ ), **JPEG COMPRESSION** (using increasingly lower JPEG compression quality values in  $\{100, 50, 25, 10, 5, 1\}$ ), and **GAUSSIAN BLUR** (with increasing radius in  $\{0, 10, 20, 30, 40, 50\}$ ). We provide examples in Figure 17). This setup simulates a controlled proxy-distribution shift. Importantly, all zero-shot evaluations are performed on the original (non-augmented) benchmarks.

The zero-shot results on FOOD-101, CIFAR-10, and IMAGENET-R in Tables 14 to 16 show that augmentations that alter image style while preserving semantic content lead to a gradual increase in ECE that closely tracks the augmentation intensity. In contrast, **GAUSSIAN BLUR** (which directly impairs object recognizability, especially at intensities 0.6 to 1.0) causes substantially stronger degradation in both ECE and NLPD. Overall, these findings indicate that BayesVLM is robust to mild stylistic shifts in the proxy data, but its performance deteriorates once the augmentations begin to compromise semantic information relevant to the model.

## F.12 ADDITIONAL ZERO-SHOT RESULTS ON ADVERSARIAL IMAGENET VARIANTS

To further assess the robustness of BayesVLM under substantial distribution shift, we evaluate the CLIP-Base model on two challenging adversarial ImageNet variants: IMAGENET-A and IMAGENET-SKETCH. These datasets introduce a severe covariate shift. IMAGENET-A contains naturally adversarial, small, or off-centre objects, whereas IMAGENET-SKETCH imposes strong stylistic changes that alter low-level statistics.

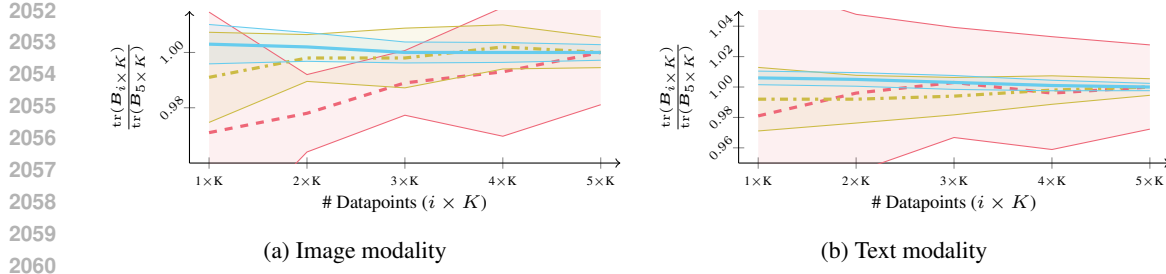


Figure 16: Normalized trace of the image Hessian  $B$ -factor for varying base batch sizes  $K$  (2048 (---), 8192 (---), 32768 (—)) and 1–5 random batches. Error bars show  $\pm 1$  std over five trials.

Table 13: **Does BayesVLM work in closed-source data settings? Yes.** With OpenCLIP ViT-B-32 trained on LAION-400M and BayesVLM estimated on the proxy dataset CC12M, we find that results are robust and show only slight degradation; statistically significant differences are **bold** ( $p = 0.05$ ).

Metrics	Dataset	FLOWERS-102	FOOD-101	CIFAR-10	CIFAR-100	IMAGENET-R	UCF101	SUN397
ACC $\uparrow$	LAION-400M	<b>68.87</b> $\pm$ 0.4630	80.43 $\pm$ 0.3968	93.62 $\pm$ 0.2444	73.63 $\pm$ 0.4406	74.45 $\pm$ 0.4361	61.43 $\pm$ 0.4868	66.96 $\pm$ 0.4703
	CC12M	68.12 $\pm$ 0.4660	80.35 $\pm$ 0.3974	93.57 $\pm$ 0.2453	73.78 $\pm$ 0.4398	74.32 $\pm$ 0.4369	61.46 $\pm$ 0.4867	66.81 $\pm$ 0.4709
NLPD $\downarrow$	LAION-400M	<b>1.73</b> $\pm$ 0.0320	0.68 $\pm$ 0.0126	0.20 $\pm$ 0.0067	0.95 $\pm$ 0.0152	<b>1.03</b> $\pm$ 0.0177	1.44 $\pm$ 0.0183	<b>1.12</b> $\pm$ 0.0155
	CC12M	1.77 $\pm$ 0.0330	0.68 $\pm$ 0.0129	0.20 $\pm$ 0.0067	0.95 $\pm$ 0.0152	1.03 $\pm$ 0.0180	1.44 $\pm$ 0.0185	1.13 $\pm$ 0.0162
ECE $\downarrow$	LAION-400M	4.22	1.69	0.72	1.92	1.78	<b>3.77</b>	<b>2.06</b>
	CC12M	<b>3.84</b>	<b>0.99</b>	<b>0.70</b>	<b>1.43</b>	<b>1.39</b>	3.83	3.89

Table 17 reports zero-shot accuracy, negative log predictive density (NLPD), and expected calibration error (ECE) for CLIP, temperature scaling, test-time augmentation (TTA), and BayesVLM. Across both datasets, BayesVLM does not show signs of epistemic underestimation. On IMAGENET-A, BayesVLM matches TTA in terms of calibration (ECE 0.23 vs. 0.23) while improving over CLIP. On IMAGENET-SKETCH, BayesVLM achieves the best calibration among all methods (ECE 0.08), outperforming temperature scaling and TTA. Although the NLPD on IMAGENET-A is slightly higher than with temperature scaling, BayesVLM still provides an improvement over CLIP.

Notably, TTA yields large accuracy gains, especially on IMAGENET-A, which likely arise from improved viewpoint coverage rather than improved uncertainty modelling: using 64 crops increases the likelihood of capturing an informative region of the image. In contrast, BayesVLM preserves single-pass inference efficiency while improving predictive calibration. Since BayesVLM is complementary to TTA, both approaches can be combined to obtain improvements in accuracy and uncertainty quality simultaneously.

Table 14: Zero-shot CLIP-Base performance on FOOD-101 versus augmentation intensity for three augmentation types.

Intensity	GRAYSCALE			Quality	JPEG COMPRESSION			Radius	GAUSSIAN BLUR		
	ACC↑	NLPD↓	ECE↓		ACC↑	NLPD↓	ECE↓		ACC↑	NLPD↓	ECE↓
0.0	80.44±0.397	0.68±0.013	1.69	100	80.44±0.397	0.68±0.013	1.69	0	80.44±0.397	0.68±0.013	1.69
0.2	80.45±0.397	0.68±0.013	1.71	50	80.48±0.396	0.68±0.012	2.21	10	80.61±0.395	0.68±0.012	2.38
0.4	80.43±0.397	0.68±0.013	1.73	25	80.54±0.396	0.68±0.012	2.26	20	80.58±0.396	0.68±0.012	3.25
0.6	80.48±0.396	0.68±0.013	1.85	10	80.59±0.396	0.68±0.012	2.23	30	80.48±0.396	0.69±0.011	5.69
0.8	80.54±0.396	0.68±0.012	2.06	5	80.58±0.396	0.68±0.012	2.74	40	80.43±0.397	0.72±0.011	8.93
1.0	80.56±0.396	0.68±0.012	2.62	1	80.51±0.396	0.68±0.012	4.38	50	80.40±0.397	0.75±0.011	11.52

Table 15: Zero-shot CLIP-Base performance on CIFAR-10 versus augmentation intensity for three augmentation types.

Intensity	GRAYSCALE			Quality	JPEG COMPRESSION			Radius	GAUSSIAN BLUR		
	ACC↑	NLPD↓	ECE↓		ACC↑	NLPD↓	ECE↓		ACC↑	NLPD↓	ECE↓
0.0	93.61±0.245	0.203±0.007	0.72	100	93.61±0.245	0.203±0.007	0.72	0	93.61±0.245	0.203±0.007	0.72
0.2	93.61±0.245	0.203±0.007	0.72	50	93.60±0.245	0.203±0.007	1.02	10	93.57±0.245	0.203±0.007	0.72
0.4	93.61±0.245	0.203±0.007	0.71	25	93.59±0.245	0.203±0.007	0.96	20	93.57±0.245	0.203±0.007	0.65
0.6	93.61±0.245	0.203±0.007	0.68	10	93.59±0.245	0.203±0.007	0.92	30	93.58±0.245	0.204±0.007	0.84
0.8	93.58±0.245	0.203±0.007	0.69	5	93.57±0.245	0.203±0.007	0.89	40	93.58±0.245	0.207±0.007	1.88
1.0	93.58±0.245	0.203±0.007	0.80	1	93.60±0.245	0.205±0.007	1.35	50	93.58±0.245	0.212±0.007	2.73

Table 16: Zero-shot CLIP-Base performance on IMAGENET-R versus augmentation intensity for three augmentation types.

Intensity	GRAYSCALE			Quality	JPEG COMPRESSION			Radius	GAUSSIAN BLUR		
	ACC↑	NLPD↓	ECE↓		ACC↑	NLPD↓	ECE↓		ACC↑	NLPD↓	ECE↓
0.0	74.49±0.436	1.031±0.018	1.71	100	74.48±0.436	1.031±0.018	1.71	0	74.49±0.436	1.031±0.018	1.71
0.2	74.51±0.436	1.031±0.018	1.70	50	74.53±0.436	1.031±0.017	2.05	10	74.67±0.435	1.029±0.017	2.04
0.4	74.51±0.436	1.031±0.018	1.61	25	74.56±0.436	1.031±0.017	1.93	20	74.69±0.435	1.031±0.017	3.01
0.6	74.48±0.436	1.030±0.018	1.72	10	74.63±0.436	1.030±0.018	1.94	30	74.76±0.434	1.046±0.016	5.70
0.8	74.47±0.436	1.030±0.018	1.89	5	74.47±0.436	1.030±0.018	1.89	40	74.71±0.435	1.077±0.016	9.28
1.0	74.56±0.436	1.029±0.018	1.95	1	74.72±0.435	1.032±0.017	3.23	50	74.75±0.434	1.109±0.015	12.20

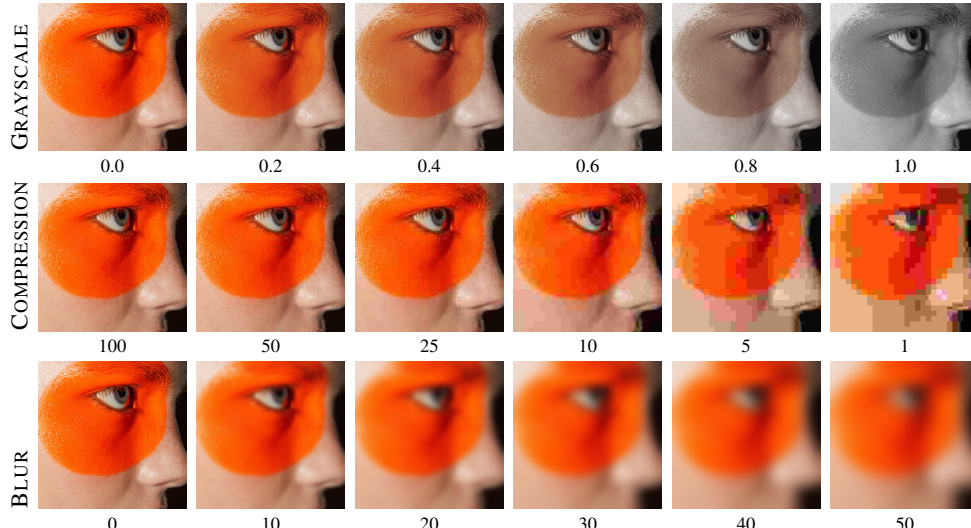


Figure 17: Visualisation of proxy-data augmentations across degradation levels. Rows correspond to augmentation types (GRAYSCALE, JPEG COMPRESSION, GAUSSIAN BLUR). Columns show increasing degradation severity, parameterised by intensity, JPEG quality, or blur radius, respectively.

Table 17: Zero-shot performance on IMAGENET-A and IMAGENET-SKETCH.

Method	IMAGENET-A			IMAGENET-SKETCH		
	Acc (%) ↑	NLPD ↓	ECE ↓	Acc (%) ↑	NLPD ↓	ECE ↓
CLIP (Radford et al., 2021)	25.87±0.4379	3.77±0.0312	0.33	50.98±0.4999	2.37±0.0303	0.16
CLIP (temp. scaling)	25.87±0.4379	3.22±0.0226	0.18	50.98±0.4999	2.29±0.0286	0.13
TTA (Farina et al., 2024)	38.67±0.4870	2.77±0.0279	0.23	52.40±0.4994	2.36±0.0300	0.15
BayesVLM	26.67±0.4422	3.36±0.0257	0.23	50.59±0.5000	2.24±0.0259	0.08